Low-Cost, Rapid, Sensitive Detection of Pathogenic Bacteria Using Phage-Based Magnetoelastic Biosensors

by

Shin Horikawa

A dissertation submitted to the Graduate Faculty of
Auburn University
in partial fulfillment of the
requirements for the Degree of
Doctor of Philosophy

Auburn, Alabama
May 5, 2013

Keywords: magnetoelastic biosensor, phage, pathogenic bacteria, food safety, biosecurity

Approved by

Bryan A. Chin, Chair, Professor of Materials Engineering
Zhongyang Cheng, Professor of Materials Engineering
Dong-Joo Kim, Associate Professor of Materials Engineering
Valery A. Petrenko, Professor of Pathobiology
Sang-Jin Suh, Associate Professor of Biological Sciences
George T. Flowers, Dean of the Graduate School

Abstract

As part of the ongoing efforts to secure food safety as well as to guard against possible bioterrorism, the role of pathogen detection technologies has become vital. However, conventional and standard detection methods, including culture-, immunology-, and polymerase chain reaction-based methods, are generally expensive, time-consuming, and labor-intensive. Hence, there is a need for new detection technologies that outperform the conventional methods and enable the rapid, on-site detection of pathogenic substances. Although label-free biosensors have proven to be among the most promising methods, meeting various performance criteria (e.g., sensitivity, selectivity, assay time, thermal stability, and longevity) simultaneously still remains a challenge. Hence, further research and development are essential before biosensors become a reliable, alternative solution.

Phage-based magnetoelastic (ME) biosensors, a novel class of wireless, mass-sensitive biosensors, are among potential candidates that could overcome the above performance challenge. These biosensors are not only thermally robust, but their wireless nature of detection offers great flexibility in design and use, which facilitates on-site pathogen detection. In addition, the sensitivity of ME biosensors can be improved by reducing their dimensions, and the fabrication cost per sensor can be reduced via batch fabrication. Hence, this dissertation presents investigations into the performance improvement of phage-based ME biosensors, in terms of cost-effectiveness, rapidness, and sensitivity, and into the enhanced detection of pathogenic bacteria, *Salmonella* Typhimurium and *Bacillus anthracis* spores, for food safety and biosecurity.

To enhance both cost-effectiveness and sensitivity, micron- to millimeter-scale ME biosensors were batch-fabricated and used. In this way, the fabrication cost per sensor was reduced to a fraction of a cent. In addition, the following two methodologies were employed to dramatically shorten assay time: (1) direct detection of *S.* Typhimurium on fresh spinach leaves and (2) detection of *B. anthracis* spores with the aid of a designed microfluidic flow cell, which ensures efficient physical contact between a biosensor and flowing spores. By using these methodologies with low-cost, miniature ME biosensors, (1) *S.* Typhimurium cells on the order of 10^4 cells/cm^2 were detected with 150-μm long sensors in 45 min, and (2) down to 106 *B. anthracis* spores were detected with 200-μm long sensors in 10 min.

Additionally, to further enhance the detection capabilities of phage-based ME biosensors, the following effects were studied: (1) the effects of mass position on the sensitivity of ME biosensors and (2) the effects of surface functionalization on surface phage coverage. The mass sensitivity of ME biosensors was found to be largely dependent on the dimensions of the sensors as well as on the position of attached masses. From numerical simulation results, a formula that predicts the mass-position-dependent sensor response for a single localized mass was also derived. In addition, surface phage coverage on bare and surface-functionalized ME biosensors was quantified by atomic force microscopy. The results showed that activated carboxyl-based covalent attachment produced a surface phage coverage of $\sim$ 50%, which is comparable to that obtained through physical adsorption, the traditional method of phage immobilization. By contrast, much lower surface phage coverages ($\sim$ 5%) were obtained for aldehyde- and methyl-terminated sensor surfaces. These differences in surface phage coverage was also found to affect the quantity of a subsequently captured analyte. Hence, by properly functionalizing the sensor surface, both surface phage coverage and the quantity of the captured analyte can be controlled. Finally, with the results of the mass-position-dependence of sensor response,

a concept of phage layer patterning was introduced. Phage may be patterned onto desired parts of the sensor surface to further enhance the detection capabilities of ME biosensors.

Acknowledgments

This dissertation would not have been possible without the guidance and help of a great number of individuals. First and foremost, I am truly indebted to my advisor, Dr. Bryan A. Chin, who has provided invaluable assistance in the preparation and completion of this research. I will never forget his generosity and encouragement. I am also grateful to all my committee members, Dr. Zhongyang Cheng, Dr. Dong-Joo Kim, Dr. Valery A. Petrenko, and Dr. Sang-Jin Suh for their sincere support. Special thanks to Dr. Valery A. Petrenko, who has helped me improve my attitude towards scientific research.

I would like to thank Dr. Maria L. Auad, Dr. Michael J. Bozack, and Dr. Michael E. Miller for their technical assistance in atomic force microscopy, x-ray photoelectron spectroscopy, and confocal scanning laser microscopy, respectively. With their expert guidance and assistance, I have been able to acquire sound engineering practices.

I am also thankful for all the support from Dr. James M. Barbaree, Kiril A. Vaglenov, and I-Hsuan Chen, who have provided all biological samples and shared a great deal of knowledge regarding microbiology over the past several years.

Yating Chai, Dr. John Shu, Michael L. Johnson, Leslie C. Mathison, Dr. Shichu Huang, Dr. Jiehui Wan, Dr. Suiqiong Li, and Steve Best have shared with me countless discussions on sensing principles, microelectronic fabrication, and testing methodologies. We have worked together in our experiments and constantly tried to gain greater understanding of our work. I would like to thank them for always being there for me.

Last but not least, I owe earnest thankfulness to my parents and sister for their love and support.

Table of Contents

List of Figures

List of Tables

List of Abbreviations

AFM	Atomic force microscopy
AUDFS	the Auburn University Detection and Food Safety Center
BSA	Bovine serum albumin
CDC	the Centers for Disease Control and Prevention
DI	Deionized
DMF	dimethylformamide
DNA	Deoxyribonucleic acid
dNTP	Deoxynucleotide triphosphate
ELISA	Enzyme-linked immunosorbent assay
FE	Finite element
LOD	Limit of detection
ME	Magnetoelastic
PCR	Polymerase chain reaction
PDMS	Poly(dimethylsiloxane)
RNA	Ribonucleic acid
SAM	Self-assembled monolayer
SEM	Scanning electron microscopy

TBS	Tris-buffered saline
VBNC	Viable but non-culturable
XPS	X-ray photoelectron spectroscopy

Chapter 1

Introduction

1.1 Background and need

Food is essential for each individual to grow and stay healthy in daily life. However, the past decades have been marked by a global increase in the outbreaks of food poisoning and associated illnesses. These public health problems are caused by the accidental supply and consumption of contaminated food, largely due to improper safety knowledge, perspectives, and practices of food producers [1] as well as insufficient consumer awareness [2]. Although substantial progress on food safety regulations has been made worldwide [3], up to 30% of the population even in industrialized countries suffer from foodborne illnesses each year [4]. In the United States, for example, approximately 48 million cases of foodborne illnesses are estimated to occur annually, resulting in 128,000 hospitalizations, 3,000 deaths, and $51.0 to $77.7 billion economic losses [5–7].

At present, 31 foodborne pathogens, including bacteria, parasites, and viruses, are identified in the United States [7]. According to the Centers for Disease Control and Prevention (CDC) [5], most foodborne illnesses in the United States are caused by norovirus (58%), followed by nontyphoidal *Salmonella* spp. (11%), *Clostridium perfringens* (10%), and *Campylobacter* spp (9%). In addition, the leading cause of both hospitalization and death is nontyphoidal *Salmonella* spp. (35% and 28%, respectively), which cause Salmonellosis, a major foodborne disease in most countries [4]. Food can be contaminated by these identified as well as unidentified pathogens at any stages of the supply chain (e.g., production, packaging, transportation, and retail). As a result, the food industry, the main party that is concerned with the presence

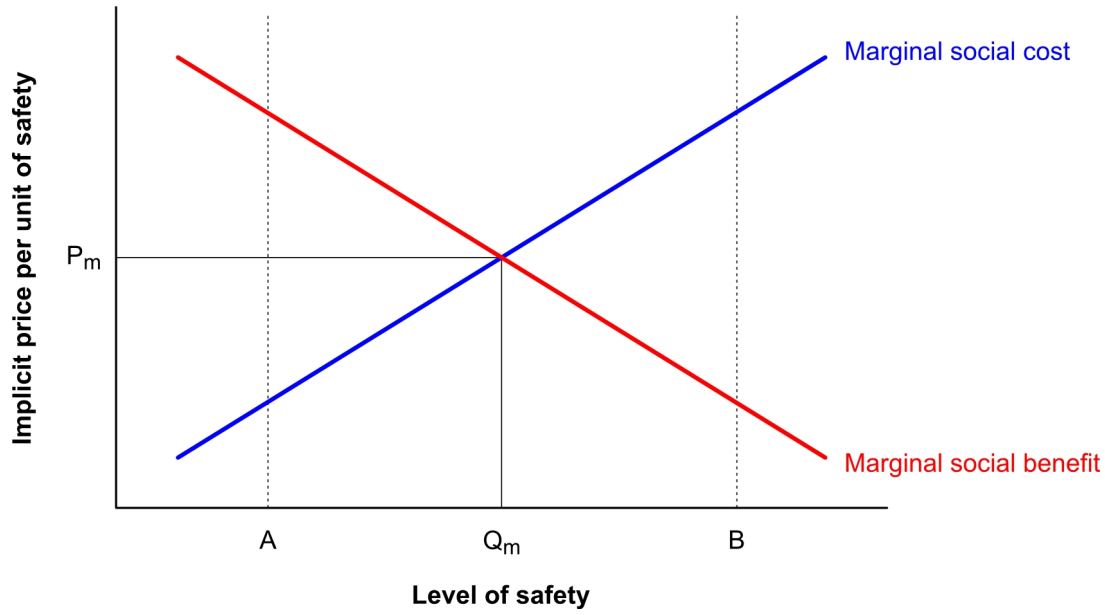

Figure 1.1: Economic cost - benefit assessment.

of foodborn pathogens, is responsible for controlling the quality of food products. However, zero risk for all food products is unlikely to be achievable. Hence, one of the biggest challenges is to put effective controls in place without unnecessarily increasing costs. In other words, the optimal level of food safety must be determined through economic cost - benefit assessments [8]. Figure 1.1 shows a typical representation of the relationship between implicit price per unit of safety and level of safety. As can be seen from the upward sloping line of marginal social cost, it is inexpensive to improve safety at low levels, but further improvements are more costly. By contrast, marginal social benefit (i.e., society's additional willingness to pay to avoid ill-health and the costs of treating ill-health) decreases as the level of safety increases, represented by the downward sloping line. At point A, the amount the society is willing to pay exceeds the amount it would cost to improve safety, indicating that it is worth allocating resources to produce more safety. By contrast, costs exceed benefits at point B, meaning that too many resources are being devoted to safety. Only at point Q_m are costs equal to benefits per unit of safety, representing that efficient resource allocation occurs [8]. Hence, this point Q_m is the sought safety level (P_m is

the corresponding price per unit of safety). From the above example of assessment, it is understandable that cost is an important factor that cannot be disregarded for the management of food safety risks.

Foodborne illness is not the only problem that poses a severe risk to public safety. Since the 2001 anthrax mail attacks in the United States, bioterrorism, which makes use of bacteria, viruses, fungi, and/or toxins as a bioweapon, has been publicly recognized as an emerging danger. The CDC has, thus far, identified 35 potential bioterrorism agents and classified them into three categories [9]. For example, *Bacillus anthracis*, the etiologic agent of anthrax, is listed among the high-priority Category A agents, which have the potential for major public health impact. Comprehensive attempts to control these deadly biological agents have been made internationally by prohibiting their use and proliferation since the war era in the last century [10]. However, as is evident from the recent anthrax attacks, the attempts have not been

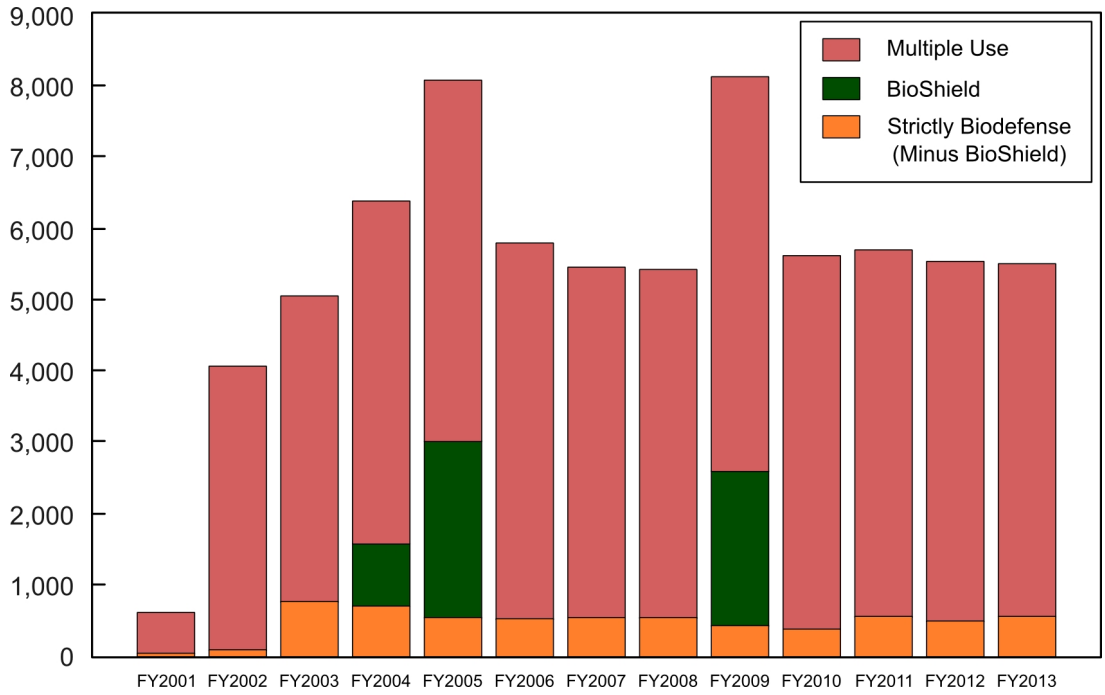

Figure 1.2: Civilian biodefense funding by fiscal year, FY2001 - FY2013 (in $millions).

entirely successful. As a result, the government of the United States has been enhancing national biosecurity. In fact, the funding for civilian biodefense dramatically increased after the 2001 anthrax attacks, and over $4 billion of funding has been maintained since the fiscal year of 2002 as shown in Fig. 1.2 [11]. The budget transition clearly indicates that there is a need for comprehensive biodefense systems that enable the nationwide surveillance and prevention of bioterrorism. In addition, a portion of the funding is dedicated to food defense, including the prevention of deliberate food contamination with pathogenic agents.

As part of the ongoing efforts to secure food safety as well as to guard against possible bioterrorism, the role of pathogen detection technologies has become vital. However, conventional and standard detection methods, including culture-, immunology-, and polymerase chain reaction-based methods, are generally expensive, time-consuming, and labor-intensive [3]. Hence, much research has been recently focused on developing label-free biosensors, which are meant to be low-cost, rapid,

Table 1.1: Major performance criteria for biosensors.

Criterion	**Description**
Sensitivity	Ability to detect a small amount of pathogens in a reasonably small sample volume
Selectivity	Ability to distinguish among pathogens
Assay time	Short for a single test
Thermal stability	Ability to function at a wide range of temperatures
Longevity	Ability to retain detection capabilities for a fair period of time
Assay protocol	No reagent addition needed
Measurement	Direct and without pre-enrichment
Format	Highly automated format
Operator	No expertise needed
Cost	Inexpensive
Size	Compact and portable for on-site detection

and user-friendly, adequate for on-site pathogen detection for both food safety and biosecurity. Table 1.1 lists the major performance criteria for biosensors (partially adapted from [12]). Although some existing biosensors possess excellent performance, meeting various performance criteria simultaneously still remains a challenge. Hence, further research and development are essential before biosensors become a reliable, alternative solution.

1.2 Research objectives

Magnetoelastic (ME) biosensors, a novel class of wireless, mass-sensitive biosensors, are among potential candidates that could overcome the above-mentioned performance challenge. In recent years, the Auburn University Detection and Food Safety Center (AUDFS) has begun research into the detection of pathogenic bacteria using freestanding, strip-shaped ME biosensors combined with a landscape phage (i.e., genetically engineered phage) [13] as the biomolecular-recognition element [14–17]. These phage-based ME biosensors are not only rapid and thermally robust [16], but their wireless nature of detection offers great flexibility in design and use, which facilitates on-site bacterial detection. In addition, the sensitivity of ME biosensors can be improved by reducing their dimensions [18], and the fabrication cost per sensor can be reduced via batch fabrication. Hence, the primary objectives of this research are (1) to further improve the cost-effectiveness, rapidness, and sensitivity of the phage-based ME biosensors and (2) to demonstrate enhanced detection of pathogenic bacteria (i.e., *Salmonella* Typhimurium and *Bacillus anthracis* spores). In order to improve both cost-effectiveness and sensitivity, micron- to millimeter-scale ME biosensors were batch-fabricated and used. In addition, the following two methodologies were employed to shorten assay time:

1. Direct detection of *S.* Typhimurium on fresh spinach leaves without any pre-test sample preparation (i.e., collection and purification of *Salmonella*-containing samples, followed by enrichment)

2. Detection of *B. anthracis* spores with the aid of a designed microfluidic flow cell, which ensures efficient physical contact between a biosensor and flowing spores.

Additionally, as potential ways to further enhance the detection capabilities of phage-based ME biosensors, the following effects were studied:

1. Effects of mass position on the sensitivity of ME biosensors

2. Effects of surface functionalization of ME biosensors on surface phage coverage.

1.3 Target pathogenic bacteria to be detected

S. Typhimurium and *B. anthracis* spores are target pathogenic bacteria to be detected in this research. Their median infectious doses and incubation periods are summarized in Table 1.2.

Table 1.2: Infectious doses and incubation periods for the target pathogenic bacteria.

Target pathogen	**Infectious dose**	**Incubation period**	**Ref.**
S. Typhimurium	100 to 1,000 cells (ingestion)	6 to 72 hr	[19]
B. anthracis	8,000 to 50,000 spores (inhalation)	$<$ 7 days	[20]

1.3.1 *Salmonella* Typhimurium

Nontyphoidal *Salmonella* spp. are important foodborne pathogens that cause gastroenteritis, bacteremia, and subsequent focal infection [21]. They are responsible for 11% of all foodborn illnesses in the United States, resulting in roughly 20,000 hospitalizations and 400 deaths each year [5]. Salmonellosis, caused by the ingestion

Table 1.3: Recent *Salmonella* outbreaks in various food products in the United States.

Source	**Cause(s)**	**Cases**	**Hospitalizations**	**Year**	**Ref.**
Tomatoes	*S.* Typhimurium	183	22	2006	[24]
Peanut butter	*S.* Tennessee	425	71	2007	[25]
Cantaloupes	*S.* Litchfield	51	> 16	2008	[26]
Jalapeño peppers	*S.* Saintpaul	1,442	> 286	2008	[27]
Peanut butter	*S.* Typhimurium	714	~ 170	2009	[28]
Alfalfa sprouts	*S.* Saintpaul	235	~ 7	2009	[29]
Shell eggs	*S.* Enteritidis	1,939	N/A	2010	[30]
Cantaloupes	*S.* Panama	20	3	2011	[31]
Sprouts	*S.* Enteritidis	25	3	2011	[32]
Ground turkey	*S.* Heidelberg	136	37	2011	[33]
Chicken livers	*S.* Heidelberg	190	30	2011	[34]
Ground beef	*S.* Typhimurium	20	8	2011	[35]
Ground tuna	*S.* Bareilly & *S.* Nchanga	425	55	2012	[36]
Ground beef	*S.* Enteritidis	46	12	2012	[37]
Cantaloupes	*S.* Typhimurium & *S.* Newport	270	101	2012	[38]
Live poultry	*S.* Montevideo	76	17	2012	[39]
Mangoes	*S.* Braenderup	121	25	2012	[40]
Peanut butter	*S.* Bredeney	30	4	2012	[41]

of nontyphoidal *Salmonella* spp., is a major foodborne disease in most countries today [4] and usually contracted from various sources [22], including eggs, meat, poultry, and fresh produce as shown in Table 1.3. Among over 2,500 serovars capable of infecting humans and animals, *S.* Typhimurium is becoming one of the most prevalent serovars [23]. Hence, this pathogenic bacterium has been selected as one of the target pathogens to be detected in this research. Figure 1.3 shows a scanning electron micrograph of *S.* Typhimurium cells on a spinach leaf surface.

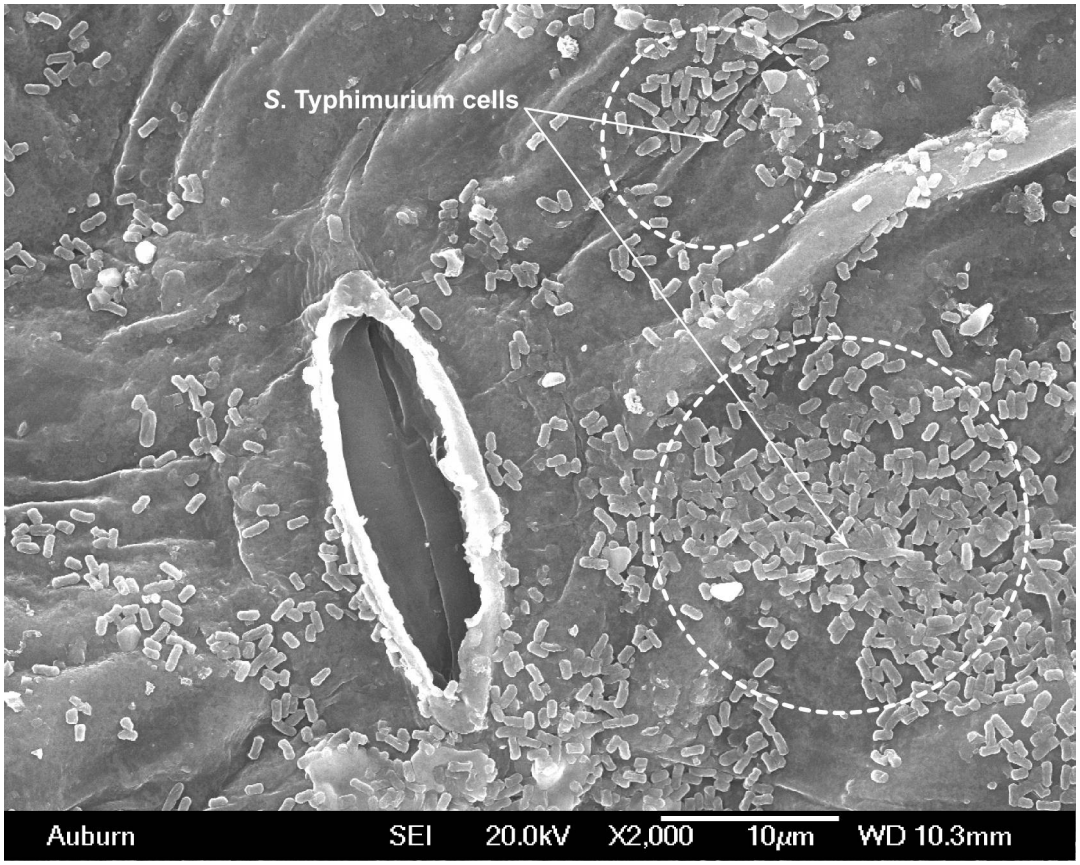

Figure 1.3: *S.* Typhimurium cells on a spinach leaf surface.

1.3.2 *Bacillus anthracis* spores

B. anthracis, the etiologic agent of anthrax, is a rod-shaped, spore-forming bacterium [42, 43]. Due to it's ability to form a resistant spore (i.e., dehydrated, thick-walled cell), this bacterium can populate a wide range of environments, including soil, bodies of water and animal hosts [42]. Although *B. anthracis* spores are metabolically dormant, they can germinate and grow to a vast number of vegetative cells once entering a nutrient-rich host, which in turn causes the disease anthrax with high fatality rates (Table 1.4). Hence, the potential use of *B. anthracis* spores as a bioweapon is a significant public safety concern. When used in an aerosolized form, they could enter the bodies of individuals through inhalation. For example, the recent anthrax attacks that occurred in the United States in 2001 resulted in 11 cases of inhalational anthrax,

Table 1.4: Types of anthrax infection and associated fatality rates.

Type	**Fatality rate**	**Ref.**
Inhalational	As high as 90% (< 50% with appropriate treatment)	[44–46]
Cutaneous	20% (< 1% with appropriate treatment)	[45, 46]
Gastrointestinal	25 to 60%	[45, 46]

5 of whom died. Although early, proper antibiotic treatments have proven effective in reducing the high fatality rates, such treatments are often difficult to provide due to initial, non-specific symptoms in infected patients [44]. Hence, anthrax infection must be prevented through early detection of *B. anthracis* spores. Figure 1.4 shows a scanning electron micrograph of *B. anthracis* spores on a gold surface.

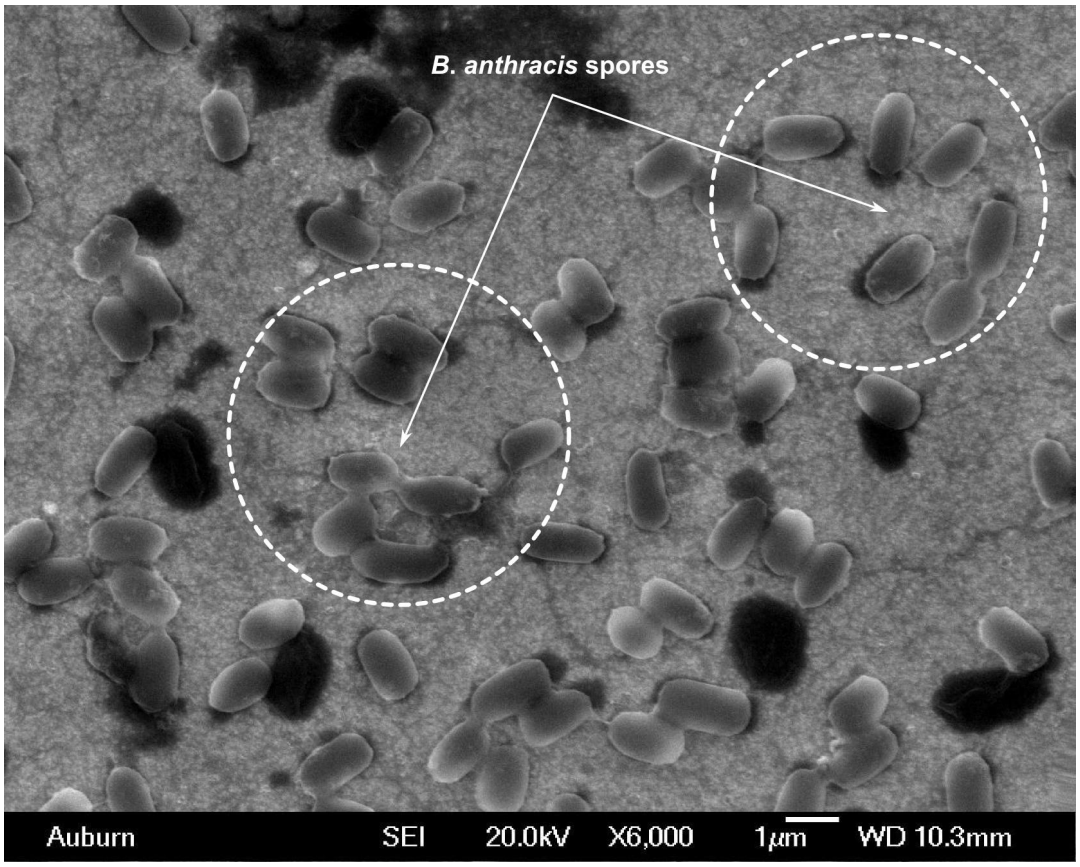

Figure 1.4: *B. anthracis* spores on a gold surface.

1.4 Organization of this dissertation

In this chapter, the need for high-performance biosensors for on-site pathogen detection was described, and the objectives of the present research were stated. The rest of this dissertation is organized as follows:

Chapter 2 briefly reviews major bacterial detection methods and discusses reasons for the current shift towards the development of label-free biosensors.

Chapter 3 describes the fundamentals, detection principle, and fabrication methods of phage-based ME biosensors in depth.

Chapter 4 presents an investigation into rapid, direct detection of *S.* Typhimurium on fresh spinach leaves. Various effects, including the topography of spinach leaf surfaces, the distribution of *S.* Typhimurium cells, and the size and number of ME biosensors, on the limit of detection will also be discussed.

Chapter 5 presents an investigation into rapid, sensitive detection of *B. anthracis* spores using micron-scale ME biosensors in combination with a designed microfluidic flow cell.

Chapter 6 investigates the effects of mass position on the sensitivity of ME biosensors. Experimental and numerical results will be first compared, and then, a formula predicting the sensor response for a single point-mass will be derived. In addition, the effects of surface functionalization on surface phage coverage will be studied. Based on the results of these investigations, a concept of the patterning of the phage layer onto desired parts of the sensor surface will be introduced.

Finally, Chapter 7 presents an overall summary and conclusions of this dissertation.

Bibliography

[1] M. L. L. Ivey, J. T. LeJeune, and S. A. Miller, "Vegetable producers perceptions of food safety hazards in the midwestern USA," *Food Control*, vol. 26, no. 2, pp. 453 – 465, 2012.

[2] C. Losasso, V. Cibin, V. Cappa, A. Roccato, A. Vanzo, I. Andrighetto, and A. Ricci, "Food safety and nutrition: Improving consumer behaviour," *Food Control*, vol. 26, no. 2, pp. 252 – 258, 2012.

[3] V. Velusamy, K. Arshak, O. Korostynska, K. Oliwa, and C. Adley, "An overview of foodborne pathogen detection: In the perspective of biosensors," *Biotechnology Advances*, vol. 28, no. 2, pp. 232 – 254, 2010.

[4] WHO, "Food safety and foodborne illness," 2007. fact sheet no. 237.

[5] E. Scallan, R. M. Hoekstra, F. J. Angulo, R. V. Tauxe, M.-A. Widdowson, S. L. Roy, J. L. Jones, and P. M. Griffin, "Foodborne illness acquired in the United States - major pathogens," *Emerging Infectious Diseases*, vol. 17, no. 1, pp. 7 – 15, 2011.

[6] E. Scallan, P. M. Griffin, F. J. Angulo, R. V. Tauxe, and R. M. Hoekstra, "Foodborne illness acquired in the United States - unspecified agents," *Emerging Infectious Diseases*, vol. 17, no. 1, pp. 16 – 22, 2011.

[7] R. L. Scharff, "Economic burden from health losses due to foodborne illness in the United States," *Journal of food protection*, vol. 75, no. 1, pp. 123 – 131, 2012.

[8] W. B. Traill and A. Koenig, "Economic assessment of food safety standards: Costs and benefits of alternative approaches," *Food Control*, vol. 21, no. 12, pp. 1611 – 1619, 2010.

[9] M. Shannon, "Management of infectious agents of bioterrorism," *Clinical Pediatric Emergency Medicine*, vol. 5, no. 1, pp. 63 – 71, 2004.

[10] D. P. Fidler, "Facing the global challenges posed by biological weapons," *Microbes and Infection*, vol. 1, no. 12, pp. 1059 – 1066, 1999.

[11] C. Franco and T. K. Sell, "Federal agency biodefense funding, FY2012 - FY2013," *Biosecurity and Bioterrorism: Biodefense Strategy, Practice, and Science*, vol. 10, no. 2, pp. 162 – 181, 2012.

[12] D. Ivnitski, I. Abdel-Hamid, P. Atanasov, and E. Wilkins, "Biosensors for detection of pathogenic bacteria," *Biosensors and Bioelectronics*, vol. 14, no. 7, pp. 599 – 624, 1999.

[13] V. A. Petrenko, "Landscape phage as a molecular recognition interface for detection devices," *Microelectronics Journal*, vol. 39, no. 2, pp. 202 – 207, 2008.

[14] S. Huang, H. Yang, R. Lakshmanan, M. Johnson, J. Wan, I.-H. Chen, H. W. III, V. Petrenko, J. Barbaree, and B. Chin, "Sequential detection of *Salmonella typhimurium* and *Bacillus anthracis* spores using magnetoelastic biosensors," *Biosensors and Bioelectronics*, vol. 24, no. 6, pp. 1730 – 1736, 2009.

[15] R. S. Lakshmanan, R. Guntupalli, J. Hu, D.-J. Kim, V. A. Petrenko, J. M. Barbaree, and B. A. Chin, "Phage immobilized magnetoelastic sensor for the detection of *Salmonella typhimurium*," *Journal of Microbiological Methods*, vol. 71, no. 1, pp. 55 – 60, 2007.

[16] J. Wan, H. Shu, S. Huang, B. Fiebor, I.-H. Chen, V. A. Petrenko, and B. A. Chin, "Phage-based magnetoelastic wireless biosensors for detecting *Bacillus anthracis* spores," *IEEE Sensors Journal*, vol. 7, pp. 470 – 477, 2007.

[17] J. Wan, M. L. Johnson, R. Guntupalli, V. A. Petrenko, and B. A. Chin, "Detection of *Bacillus anthracis* spores in liquid using phage-based magnetoelastic micro-resonators," *Sensors and Actuators B: Chemical*, vol. 127, no. 2, pp. 559 – 566, 2007.

[18] M. L. Johnson, J. Wan, S. Huang, Z. Cheng, V. A. Petrenko, D.-J. Kim, I.-H. Chen, J. M. Barbaree, J. W. Hong, and B. A. Chin, "A wireless biosensor using microfabricated phage-interfaced magnetoelastic particles," *Sensors and Actuators A: Physical*, vol. 144, no. 1, pp. 38 – 47, 2008.

[19] http://www.msdsonline.com/resources/msds-resources/free-safety-data-sheet-index/salmonella-spp.aspx.

[20] http://www.msdsonline.com/resources/msds-resources/free-safety-data-sheet-index/bacillus-anthracis.aspx.

[21] D. Acheson and E. L. Hohmann, "Nontyphoidal Salmonellosis," *Clinical Infectious Diseases*, vol. 32, no. 2, pp. 263 – 269, 2001.

[22] http://www.harrisonspractice.com/practice/ub/view/Harrisons%20Practice/141052/all/Nontyphoidal_Salmonellosis.

[23] http://www.safe-poultry.com/ParatyphoidSalmonella.asp.

[24] http://www.cdc.gov/ncidod/dbmd/diseaseinfo/salmonellosis_2006/110306_outbreak_notice.htm.

[25] http://www.cdc.gov/ncidod/dbmd/diseaseinfo/salmonellosis_2007/030707_outbreak_notice.htm.

[26] http://www.cdc.gov/salmonella/litchfield/.

[27] http://www.cdc.gov/salmonella/saintpaul/jalapeno/index.html.

[28] http://www.cdc.gov/salmonella/typhimurium/update.html.

[29] http://www.cdc.gov/salmonella/saintpaul/alfalfa/.

[30] http://www.cdc.gov/salmonella/enteritidis/index.html.

[31] http://www.cdc.gov/salmonella/panama0311/062311/index.html.

[32] http://www.cdc.gov/salmonella/sprouts-enteritidis0611/070611/index.html.

[33] http://www.cdc.gov/salmonella/heidelberg/111011/index.html.

[34] http://www.cdc.gov/salmonella/heidelberg-chickenlivers/011112/index.html.

[35] http://www.cdc.gov/salmonella/typhimurium-groundbeef/020112/index.html.

[36] http://www.cdc.gov/salmonella/bareilly-04-12/index.html.

[37] http://www.cdc.gov/salmonella/enteritidis-07-12/index.html.

[38] http://www.cdc.gov/salmonella/typhimurium-cantaloupe-08-12/index.html.

[39] http://www.cdc.gov/salmonella/montevideo-06-12/index.html.

[40] http://www.cdc.gov/salmonella/braenderup-08-12/index.html.

[41] http://www.cdc.gov/salmonella/bredeney-09-12/index.html.

[42] A. Driks, "The *Bacillus anthracis* spore," *Molecular Aspects of Medicine*, vol. 30, no. 6, pp. 368 – 373, 2009.

[43] T. M. Koehler, "*Bacillus anthracis* physiology and genetics," *Molecular Aspects of Medicine*, vol. 30, no. 6, pp. 386 – 396, 2009.

[44] T. V. Inglesby, T. O'Toole, D. A. Henderson, J. G. Bartlett, M. S. Ascher, E. Eitzen, A. M. Friedlander, J. Gerberding, J. Hauer, J. Hughes, J. McDade, M. T. Osterholm, G. Parker, T. M. Perl, P. K. Russell, and K. Tonat, "Anthrax as a biological weapon, 2002: Updated recommendations for management," *The Journal of the American Medical Association*, vol. 287, no. 17, pp. 2236 – 2252, 2002.

[45] http://www.bt.cdc.gov/agent/anthrax/faq/.

[46] http://www.upmc-biosecurity.org/website/our_work/biological-threats-and-epidemics/fact_sheets/anthrax.html.

Chapter 2

Review of the Literature on Bacterial Detection Methods

This chapter reviews major bacterial detection methods and discusses reasons for the current shift towards the development of label-free biosensors.

2.1 Conventional detection methods

Conventional methods for the detection of pathogenic bacteria rely on specific microbiological or biochemical identification. Three major conventional methods are culture-, immunology-, and polymerase chain reaction-based methods as shown in Fig. 2.1. Although these methods can be highly sensitive, selective, and reliable, their application to on-site bacterial detection is greatly restricted by several drawbacks, including long assay times, high cost, and cumbersome procedures, requiring trained personnel.

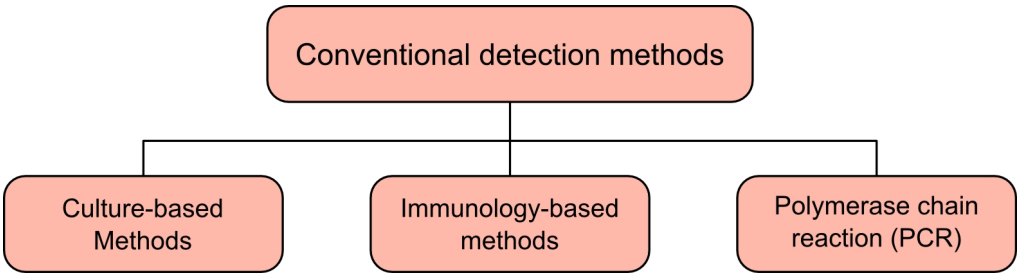

Figure 2.1: Conventional methods for bacterial detection.

2.1.1 Culture-based methods

Culture-based methods remain the most reliable and commonly used techniques for bacterial detection. These methods are capable of identifying a small number of

pathogenic bacteria (down to single bacteria). However, cumbersome assay steps, including pre-enrichment, selective enrichment, colony counting, biochemical screening, and serological confirmation, are generally required [1]. As a result, depending on bacterial species and/or strains, these culture-based methods may take days to weeks to yield results, which hinders their use in on-site bacterial detection. In addition, some viable bacteria in the environment may enter a dormant state and become non-culturable (i.e., viable but non-culturable (VBNC) state), which leads to an underestimation of the quantity of the bacteria or a failure to identify the bacteria in a contaminated sample [2]. Table 2.1 shows examples of culture-based bacterial detection and their assay times.

Table 2.1: Examples of culture-based bacterial detection.

Detected pathogen	**Assay time**	**Ref.**
Escherichia coli O157:H7	2 days	[3]
Salmonella Enteritidis	4 to 8 days	[4]
Listeria monocytogenes	up to 7 days	[5, 6]
Campylobacter fetus	14 to 16 days	[7]

2.1.2 Immunology-based methods

Immunology-based methods, the majority of which rely on an antibody - antigen binding, have been widely used for the detection of pathogenic bacteria, including *Escherichia coli*, *Salmonella* spp., *Listeria monocytogenes*, *Campylobacter* spp., and *Staphylococcal enterotoxins* [2]. Among existing methods, enzyme-linked immunosorbent assay (ELISA), which is relatively rapid and versatile, is the most commonly used technique. Figure 2.2 illustrates a typical procedure for sandwich ELISA, a commonly used ELISA variant. The assay steps are as follows:

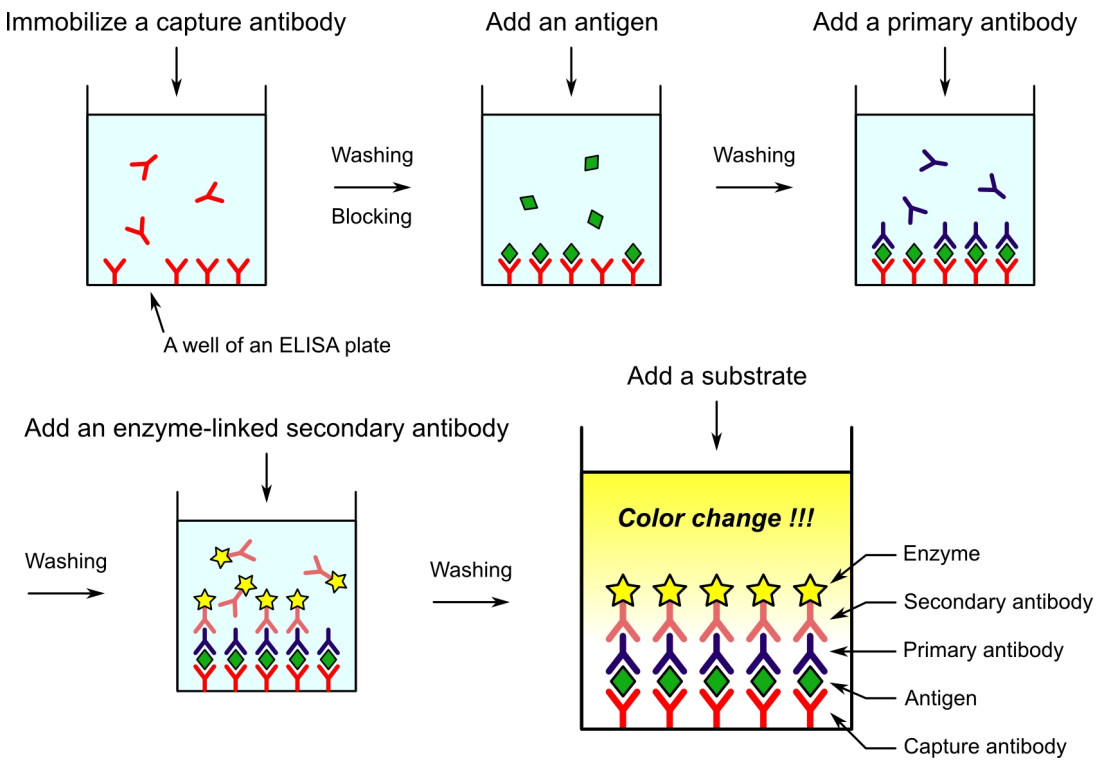

Figure 2.2: Typical procedure for sandwich ELISA.

1. Immobilize a capture antibody on the surface of each well of a microtiter plate (often called an ELISA plate). Then, wash the plate so that any unbound antibodies are removed.

2. Block any non-specific adsorption sites on the well surface with a surface blocking agent (usually, bovine serum albumin or casein).

3. Apply a sample that contains a target antigen to the plate and allow the capture antibody to bind with the antigen. Then, wash the plate to remove any unbound antigens.

4. Add a primary antibody and allow it to bind with the antigen. Then, wash the plate.

5. Add an enzyme-linked secondary antibody that binds with the primary antibody. Then, wash the plate.

6. Finally, add a substrate that can be converted by the enzyme into a color or electrochemical signal for measurement.

Although ELISA-based methods are much more rapid than culture-based methods, hours to days are still required to yield results [8–10]. In addition, their limits of detection (LODs) are not competitive with those of culture-based methods. Furthermore, cumbersome assay procedures (i.e., a series of washing and addition of reagents) make ELISA-based methods unsuitable for on-site bacterial detection. Table 2.2 shows examples of ELISA-based bacterial detection and their LODs.

Table 2.2: Examples of ELISA-based bacterial detection.

Detected pathogen	**LOD**	**Ref.**
Escherichia coli O157	10^3 to 10^4 cfu/ml	[11, 12]
Salmonella serovars	10^6 cells/ml	[13]
Listeria monocytogenes	10^3 cells/ml	[14]
Campylobacter fetus	10^5 cells/ml	[7]

2.1.3 Polymerase chain reaction-based methods

The polymerase chain reaction (PCR) is a biochemical technique to produce millions of copies of a fragment of a nucleic acid (usually, deoxyribonucleic acid (DNA), which is more stable than ribonucleic acid (RNA)). PCR-based methods have been widely used to identify or detect pathogenic bacteria, including *Salmonella aureus*, *Listeria monocytogenes*, *Bacillus cereus*, *Escherichia coli* O157:H7, and *Campylobacter jejuni* [2]. As shown in Fig. 2.3, the PCR typically requires a series of 20 to 40 thermal cycles. In each cycle, there are three discrete temperature steps as described below:

1. Denaturation: separating double-stranded DNA into a pair of single-stranded DNA templates at a temperature of around 95 °C.

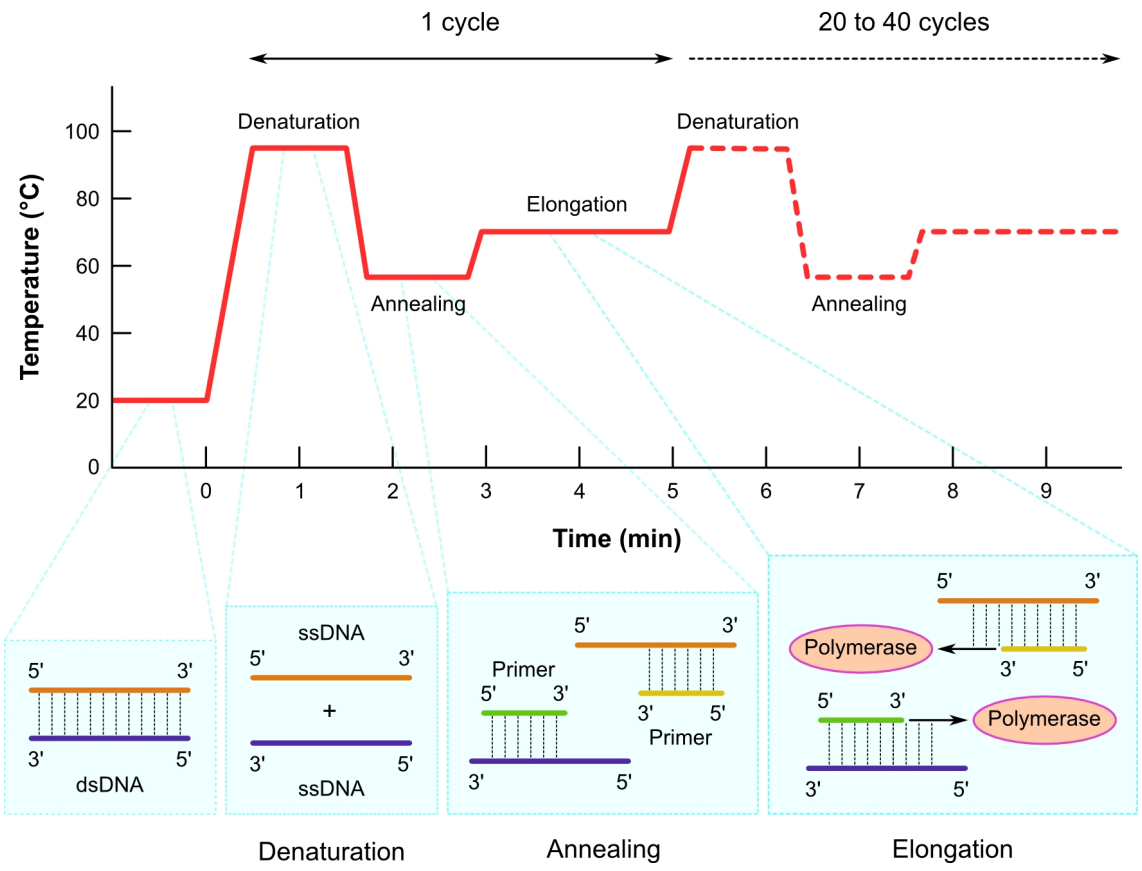

Figure 2.3: Schematic illustration of the PCR cycle.

2. Annealing: allowing annealing of forward and reverse primers to the single-stranded DNA templates at a temperature of 50 to 65 °C.

3. Elongation: extending the primers with the aid of DNA polymerase to synthesize complementary strands at a temperature of around 70 °C.

In this way, the number of amplicons doubles after each cycle, resulting in exponential amplification in the amount of the target DNA sequence. Since each cycle requires only several minutes, millions of amplicons can be produced within a few hours. After thermal cycling, the final PCR products are typically analyzed by gel electrophoresis.

PCR-based methods possess the capability of detecting a small amount of target DNA (down to a few DNA molecules [15, 16]) as well as offer high specificity and

accuracy. In addition, they are relatively rapid (i.e., a few hours of assay time) when compared with culture- and immunology-based methods. However, their use in on-site bacterial detection is restricted by a number of shortcomings. They require pure DNA samples and specific primers for avoiding false amplification, expensive reagents (e.g., DNA polymerase, deoxynucleotide triphosphate (dNTP), and other additives), and hours of thermal cycles, followed by a gel electrophoresis-based analysis, which usually takes one additional hour. In other words, these PCR-based methods are complex, expensive, and still time-consuming. Although newer PCR variants, including real-time PCR [17], digital PCR [18], and microfluidic PCR [19], can offer a much shorter assay time with less volumes of reagents, the use of a fluorescent-labeled DNA probe as well as an optical detector for the acquisition of fluorescence signals is additionally needed, leading to an increase in cost and assay complexity. Furthermore, PCR-based methods cannot generally discriminate between viable and non-viable cells [20], as well as the extraction of DNA from a resistant bacterial spore, such as a *B. anthracis* spore, remains a challenge [21]. Examples of PCR-based bacterial detection and their LODs are shown in Table 2.3.

Table 2.3: Examples of PCR-based bacterial detection.

Detected pathogen	**LOD**	**Ref.**
Escherichia coli	10^2 cells/ml	[22]
Salmonella Enteritidis	1 cfu/25 g or ml of food samples	[23]
Listeria monocytogenes	3 cfu/g in ground beef	[24]
Campylobacter spp.	100 to 150 cfu/ml	[25]
Legionella pneumophila	$<$ 10 cfu/ml	[26]

2.2 Biosensors as promising bacterial detection methods

Figure 2.4 shows the number of research articles published between 1985 and 2005 on different bacterial detection methods [20]. As can be seen, the most popular detection methods were PCR-, culture-, and ELISA-based methods, which is due to their low LODs and high reliability as mentioned in the previous sections. However, in addition to these conventional methods, emerging biosensor technologies have been drawing much attention in recent years. In fact, the global market for biosensors in 2012 is estimated to be $8.5 billion and projected to reach $16.8 billion by 2018 [27]. Biosensor technologies come with promises of equally reliable results in much shorter times [20].

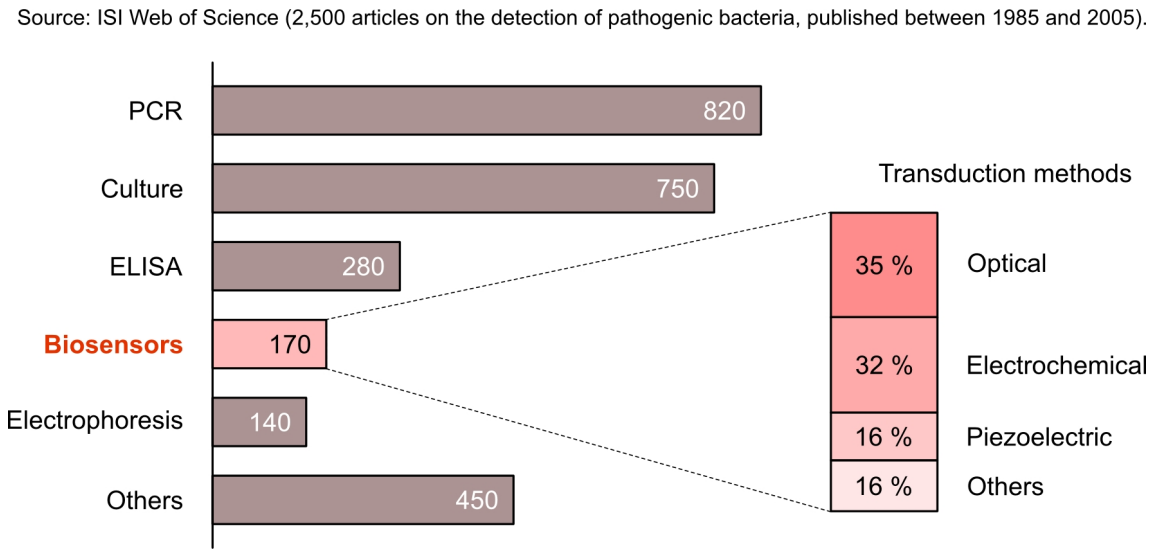

Figure 2.4: Number of research articles published between 1985 and 2005 on different bacterial detection methods.

2.2.1 Definition of a biosensor

A biosensor is an analytical device that converts a biological response into an electrical signal. Two principal components of a biosensor are: (1) a biomolecular-recognition element, which recognizes and specifically binds with a target analyte,

and (2) a signal transducer, which converts the recognition event into a measurable electrical signal.

Figure 2.5 shows a schematic diagram of a biosensor. When a biomolecular-recognition event occurs, a signal can be instantaneously generated by the transducer. This initial, small input signal from the transducer is, then, amplified, processed, and sent to an output system for display or further analyses. Biosensors can be rapid, sensitive, target-specific, and portable, which makes them suitable for use in a variety of fields, including medical care, environmental monitoring, food safety, and biosecurity. Biosensors can be classified by their recognition elements and/or signal transduction methods as shown in Fig. 2.6.

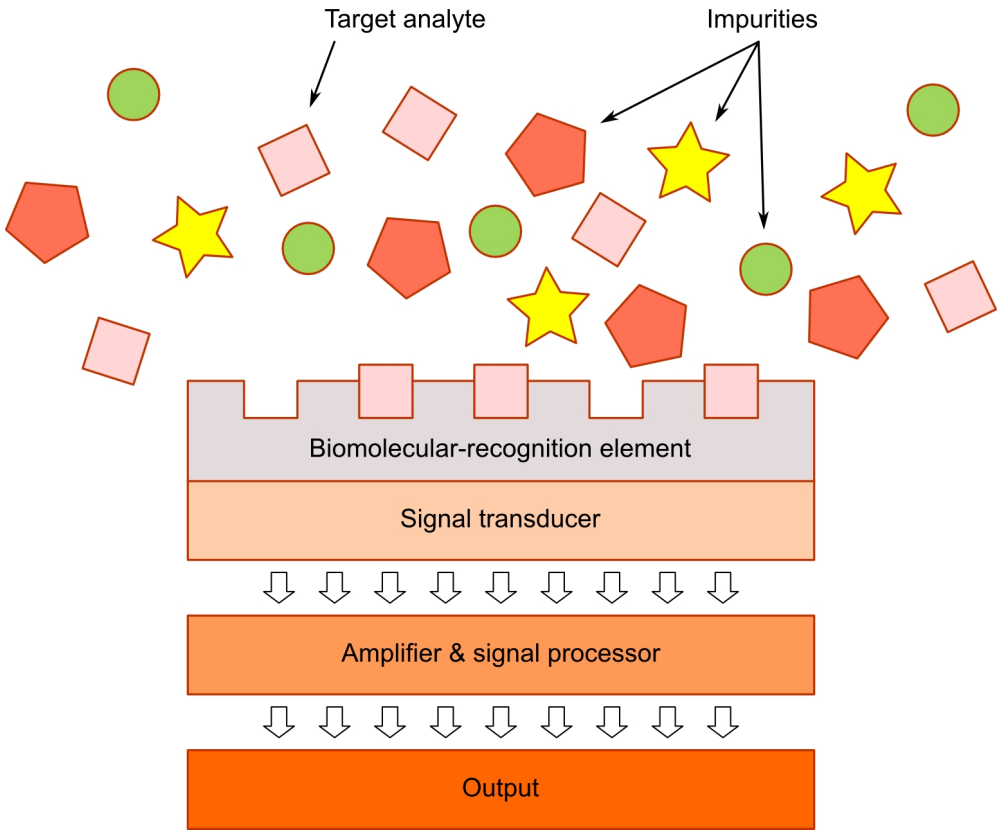

Figure 2.5: Schematic diagram of a biosensor.

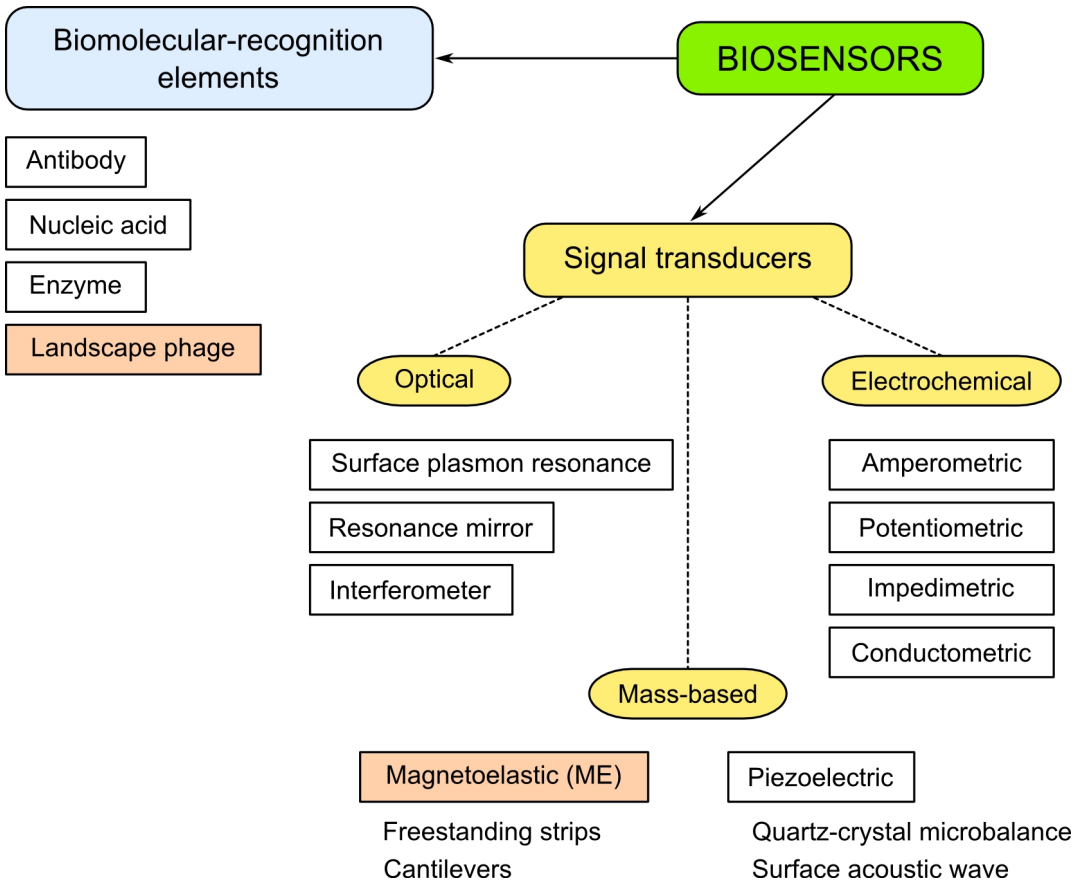

Figure 2.6: Classification of biosensors.

2.2.2 Biomolecular-recognition elements

Biomolecular-recognition elements are responsible for specifically binding a target analyte to a biosensor. They are generally immobilized on the surface of a signal transducer. Antibodies, nucleic acids, and enzymes are three major types of biomolecular-recognition elements as can be seen in Fig. 2.6. In recent years, however, a number of attempts have been made in employing landscape phages (i.e., genetically engineered phages) as the biomolecular-recognition element for the detection of pathogenic bacteria [28–31]. Landscape phages are highly tailorable, specific, relatively inexpensive, and thermally robust (much better than commonly used antibodies) [32]. Hence, in this research, landscape phages were affinity-selected for the target pathogenic bacteria (i.e., *S.* Typhimurium and *B. anthracis* spores) and used.

2.2.3 Signal transducers

Signal transducers are responsible for converting a biomolecular-recognition event into a measurable electrical signal. In the past decades, a wide variety of transduction methods has been developed. Among them, optical, electrochemical, and mass-based methods are the most commonly used methods (Fig. 2.6). Each of these major types of transducers contains many different subtypes. In addition, they can be further classified into labeled and label-free methods. While the labeled methods depend on the detection of a specific label (e.g., fluorescent, chemiluminescent, and radioactive labels), the label-free methods are based on the direct measurement of a phenomenon occurring on a transducer surface [2]. In this research, freestanding, strip-shaped magnetoelastic (ME) transducers, a novel class of mass-based transducers, were combined with the above-mentioned landscape phages and used. Compared with conventional mass-based transducers (e.g., piezoelectric transducers), ME transducers possess advantageous features, such as low-cost production, wireless signal transduction, and thus, flexibility in biosensor design. These unique characteristics of ME transducers facilitate on-site bacterial detection.

2.3 Conventional detection methods vs. biosensors

Table 2.4 compares the LODs and assay times of major bacterial detection methods. As mentioned earlier, the conventional detection methods possess low LODs, and even single pathogenic bacteria can be detected with culture-based methods. However, the conventional methods are all time-consuming (i.e., up to weeks of assay time required), and thus, the final results can not be obtained rapidly. By contrast, biosensors are generally much more rapid (i.e., on the order of minutes and up to hours of assay time), which is a distinct advantage for on-site bacterial detection for food safety and biosecurity. However, their LODs need to be improved so that they can be competitive with the conventional detection methods. In addition, other

Table 2.4: Comparison of the performance of major bacterial detection methods.

Detection method	**LOD**	**Assay time**	**Ref.**
Conventional methods			
Culture	Down to a single cell	Days to weeks	[3–7]
ELISA	10^3 to 10^6 cfu/ml	Hours to days	[7, 11–14]
PCR	Down to a single cell	Hours	[16, 22–26]
Optical biosensors			
Surface plasmon resonance	50 to 10^5 cfu/ml	15 min to hours	[33–36]
Resonant mirror	10^3 spores	10 min	[37]
Interferometer	5×10^6 cfu/ml	$<$ 40 min	[38]
Ring resonator	10^5 cfu/ml	$<$ 60 min	[39]
Bioluminescence	10 cfu/ml	20 min	[40]
Electrochemical biosensors			
Amperometric	10^1 to 10^3 cfu/ml	Minutes to hours	[41–45]
Potentiometric	10^1 to 10^3 cfu/ml	30 min to 1.5 hr	[46–48]
Impedimetric	2 cfu/ml	45 min	[49]
Conductometric	61 cfu/ml	8 min	[50]
Mass-based biosensors			
Quartz-crystal microbalance	10^3 spores/ml	$<$ 30 min	[51]
Love-wave	$<$ 200 spores/ml	5 min	[52]
Silicon cantilevers	1 spore in air	hours	[53]
	50 spores in water	hours	[53]
Piezoelectric cantilevers	300 spores/ml	$<$ 20 min	[54]
Magnetoelastic cantilevers	10^5 cfu/ml	$<$ 120 min	[55]
Magnetoelastic strips	10^3 cfu/ml	$<$ 30 min	[56]

performance criteria previously shown in Table 1.1 need to be met before biosensors become reliable alternatives.

2.3.1 Probability of detection: PCR vs. biosensors

Although there is still room for improvement, biosensors are promising tools for pathogen detection, which may be explained with a statistical model reported by Sabelnikov et al [15]. The model can be used to estimate the probability of detection for an aerosolized pathogen (e.g., aerosolized *B. anthracis* spores) using a model detector or its network. A model detector is defined as a single device that consists of an aerosol sampler and a detection device based on any of known bacterial detection methods, such as PCR-, immunology-, and biosensor-based methods. In addition, a network of model detectors consists of m single model detectors, each of which operates in the same way and deals with the same amount of a sample that contains a target pathogen. The assumptions for this statistical model are as follows [15]:

1. There is a space that contains aerosolized particles of a pathogen. These pathogen particles are distributed in the space according to a Poisson distribution with a parameter, λ, which is equal to the mean concentration of the pathogen.

2. The aerosol sampler intakes the air with a flow rate, W_s, and concentrates the aerosolized pathogen with an efficiency, K_e, into a liquid collective sample with a volume, V_c.

3. The time of sampling is set equal to the time of inhalation of the pathogen by an individual. Since the total number of the pathogens inhaled by the exposed individual, D_i, is equal to the concentration of the pathogen in the air multiplied by the time of exposure and the inhalation rate, W_h, this assumption allows to exclude time and concentration factors from all calculations.

4. n individual samples of identical volume, V_s, are simultaneously tested for detection.

5. The pathogen can be detected in a single sample (i.e, $n = 1$) with a probability of 100% only if its amount in the sample is greater than or equal to a certain threshold value, I. In other words, the value I represents the LOD of the detection device (i.e., the minimum detectable number of pathogens per sample volume, V_s). For simplification, neither false positives nor false negatives are allowed.

Based on the above assumptions, the probability of detection of the pathogen in a single sample (i.e., $n = 1$), P_{ds}, may be expressed as

$$P_{\mathrm{ds}} = 1 - \sum_{k=0}^{I-1} F(k), \tag{2.1}$$

$$F(k) = \frac{(\lambda V_s)^k e^{-\lambda V_s}}{k!}, \tag{2.2}$$

$$\lambda = \frac{K_e D_i W_s}{W_h V_c}, \tag{2.3}$$

where $F(k)$ is the probability of finding exactly k pathogens in the sample volume, V_s. In addition, the probability of detection with one model detector (i.e., $m = 1$ with n samples), P_{dn}, is equal to the probability that the pathogen can be detected in at least one of n individual samples, which can be calculated by

$$P_{\mathrm{dn}} = 1 - (1 - P_{\mathrm{ds}})^n. \tag{2.4}$$

By analogy, the probability of detection with a network of m model detectors, P_{dm}, can be computed by

$$P_{\mathrm{dm}} = 1 - (1 - P_{\mathrm{dn}})^m. \tag{2.5}$$

The use of the above equations allows one to compare different bacterial detection methods in terms of their probability of detection with respect to the inhalation dose of a target pathogen. Here, as an example, comparisons will be made for PCR-

and biosensor-based methods. In all calculations, K_e and V_c were kept constant and equal to 0.8 and 10 ml, respectively, which are currently used in the most advanced commercial samplers [58, 59]. In addition, an inhalation rate (W_h) of 11 l/min for adult humans [60] was used. For convenience, all the variables and their values used are summarized in Table 2.5.

Table 2.5: Variables and their values used for the calculations of the probability of detection.

Variable	**Values**	**Ref.**
D_i: total number of inhaled pathogens	1 to 100	
W_s: intake flow rate of the sampler	1,000 l/min	[57, 58]
K_e: efficacy coefficient of the sampler (ratio of the number of concentrated pathogens to the number of sampled pathogens)	0.8	[58]
V_c: volume of a liquid collective sample	10 ml	[58, 59]
V_s: volume of an individual sample for detection	(1) 50 to 500 μl for PCR (2) 1 ml for biosensors	[15]
n: number of individual samples	(1) 96 or 384 for PCR (2) 1 for biosensors	[15]
I: detectable number of pathogens per sample volume, V_s	(1) 15 for PCR (2) 50 for biosensors	[15]
m: number of model detectors	(1) 1 for PCR (2) 1 to 4 for biosensors	
W_h: inhalation rate for adult humans	11 l/min	[60]

Figure 2.7 shows the results for PCR-based detectors. These detectors can simultaneously test 96 or 384 samples (i.e., $n = 96$ or 384, based on the standard 96- or 384-well format of PCR technologies) with $I = 15$, which is of the best commercial, field-operated PCR device [15]. In addition, various values of V_s (50, 100, and 500 μl) were used in the calculations. For a standard PCR-based detector ($n = 96$ and $V_s = 50$ μl), it was found that 36 and more pathogens can be detected with a probability of 100% (solid curve). In addition, a slightly better result was obtained with $n = 384$, which reduces the minimum detectable number of pathogens with a probability

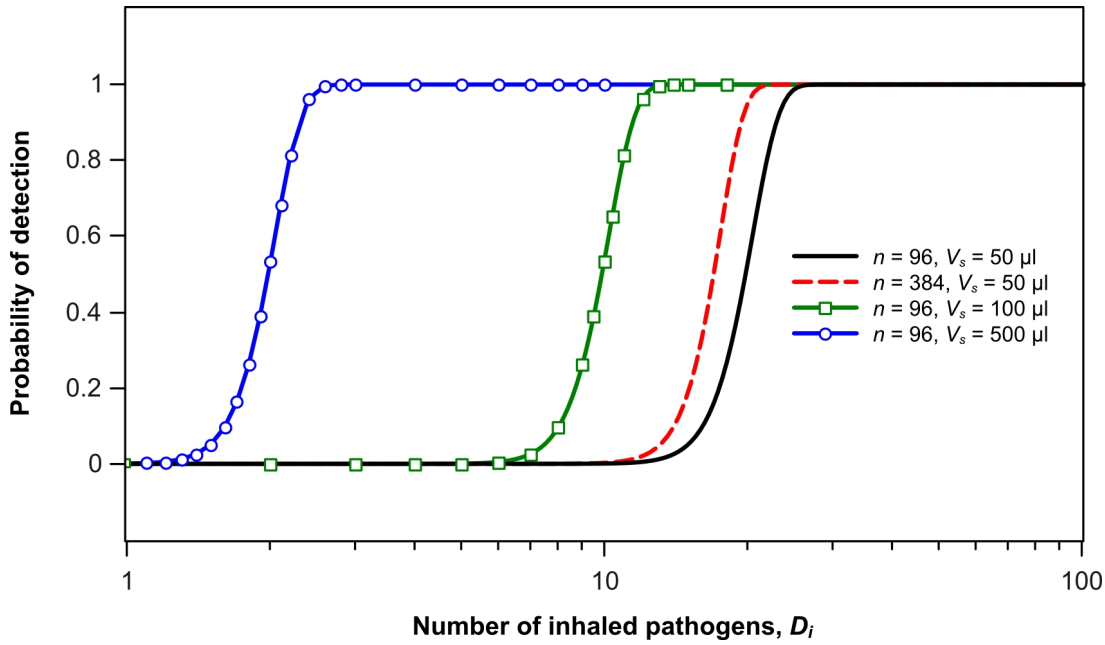

Figure 2.7: Probability of detection with respect to the inhalation dose of the target pathogen for PCR-based detectors. The following values were used in the calculations: $W_s = 1{,}000$ l/min, $K_e = 0.8$, $I = 15$, and $m = 1$.

of 100% to be 28 (dashed curve). However, for both detectors, detection of less than 10 pathogens was found to be hardly possible, which may lead to certain risks of lethality in humans for some existing pathogens. For instance, Table 2.6 shows lethal doses of *B. anthracis* spores in humans for different levels of lethality. The LD_{10}, the lethal dose at which 10% of the population is expected to die, may be as low as 50 to 98 spores, and even lower lethal doses for the LD_5 and LD_1 have been reported. Comparing the above calculated and these reported lethal doses clearly indicates that both of the standard PCR-based detectors would fail to detect *B. anthracis* spores in doses that could still cause a lethality of 5%. Although an increase in the volume of

Table 2.6: Lethal doses of *B. anthracis* spores in humans.

Level of lethality	**Lethal dose [spores]**	**Ref.**
LD_{10}	50 to 98	[61]
LD_5	14 to 28	[61]
LD_1	1 to 3	[61]

individual samples, V_s, further reduces the minimum detectable number of pathogens (solid curves with squares and circles in Fig. 2.7), the use of such larger volumes per sample (i.e., V_s = 100 or 500 μl) is not practical because it obviously increases costs due to a corresponding increase in the volumes of reagents required for the PCR (i.e., DNA polymerase, dNTPs, and other additives).

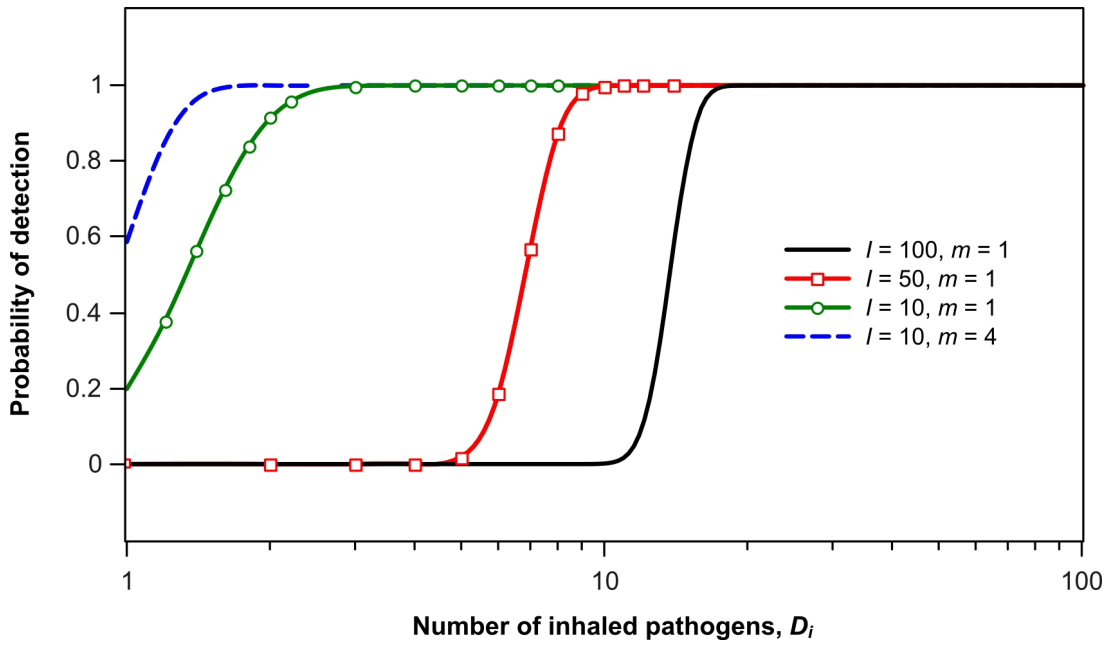

Figure 2.8: Probability of detection with respect to the inhalation dose of the target pathogen for biosensor-based detectors. The following values were used in the calculations: W_s = 1,000 l/min, K_e = 0.8, V_s = 1 ml, and n = 1.

Figure 2.8 shows the results for biosensor-based detectors with various values of I (10, 50, and 100 pathogens per V_s). Biosensors generally deal with a much larger individual sample volume (1 ml) than standard PCR-based methods (50 μl). Hence, if the value of I is sufficiently small, they could outperform standard PCR-based detectors as shown in Table 2.7. It can be seen that the minimum detectable number of pathogens for the biosensor-based detectors dramatically decreases as the value of I is decreased. In addition, when a network of four detectors (i.e., m = 4) with I = 10 is used, down to four pathogens can be detected. Hence, these calculation results indicate that the use of biosensors can be a better choice than PCR-based detection

methods. Particularly, the use of a network of biosensors offers a promise in rapid, sensitive detection of target pathogens.

Table 2.7: Minimum detectable number of pathogens for PCR- and biosensor-based methods.

Detection method	I	V_s	n	m	**Minimum detectable number of pathogens**
Standard PCR	15	50 μl	96	1	36
Biosensor	100	1 ml	1	1	29
Biosensor	50	1 ml	1	1	19
Biosensor	10	1 ml	1	1	9
Biosensor	10	1 ml	1	4	4

Bibliography

[1] J. J. Gooding, "Biosensor technology for detecting biological warfare agents: Recent progress and future trends," *Analytica Chimica Acta*, vol. 559, no. 2, pp. 137 – 151, 2006.

[2] V. Velusamy, K. Arshak, O. Korostynska, K. Oliwa, and C. Adley, "An overview of foodborne pathogen detection: In the perspective of biosensors," *Biotechnology Advances*, vol. 28, no. 2, pp. 232 – 254, 2010.

[3] G. Ngwa, R. Schop, S. Weir, C. León-Velarde, and J. Odumeru, "Detection and enumeration of *E. coli* O157:H7 in water samples by culture and molecular methods," *Journal of Microbiological Methods*, vol. 92, no. 2, pp. 164 – 172, 2013.

[4] B. Lungu, W. D. Waltman, R. D. Berghaus, and C. L. Hofacre, "Comparison of a real-time PCR method with a culture method for the detection of *Salmonella enterica* serotype Enteritidis in naturally contaminated environmental samples from integrated poultry houses," *Journal of food protection*, vol. 75, no. 4, pp. 743 – 747, 2012.

[5] E. de Boer and R. R. Beumer, "Methodology for detection and typing of foodborne microorganisms," *International Journal of Food Microbiology*, vol. 50, no. 12, pp. 119 – 130, 1999.

[6] S. Artault, J. L. Blind, J. Delaval, Y. Dureuil, and N. Gaillard, "Detecting *Listeria monocytogenes* in food," *International Food Hygiene*, vol. 12, p. 23, 2001.

[7] B. Brooks, J. Devenish, C. Lutze-Wallace, D. Milnes, R. Robertson, and G. Berlie-Surujballi, "Evaluation of a monoclonal antibody-based enzyme-linked immunosorbent assay for detection of *Campylobacter fetus* in bovine preputial washing and vaginal mucus samples," *Veterinary Microbiology*, vol. 103, no. 12, pp. 77 – 84, 2004.

[8] K. D. King, J. M. Vanniere, J. L. LeBlanc, K. E. Bullock, and G. P. Anderson, "Automated fiber optic biosensor for multiplexed immunoassays," *Environmental Science & Technology*, vol. 34, no. 13, pp. 2845 – 2850, 2000.

[9] F. S. Ligler, G. P. Anderson, P. T. Davidson, R. J. Foch, J. T. Ives, K. D. King, G. Page, D. A. Stenger, and J. P. Whelan, "Remote sensing using an airborne biosensor," *Environmental Science & Technology*, vol. 32, no. 16, pp. 2461 – 2466, 1998.

[10] K. Tsuchiya and C. C. dUrsel, "Development of a sensitive ELISA using three monoclonal antibodies against lipopolysaccharides to detect *Xanthomonas campestris pv. vesicatoria*, the causal agent of bacterial spot of tomato and pepper," *Journal of General Plant Pathology*, vol. 70, pp. 21 – 26, 2004.

[11] B. W. Blais, J. Leggate, J. Bosley, and A. Martinez-Perez, "Comparison of fluorogenic and chromogenic assay systems in the detection of *Escherichia coli* O157 by a novel polymyxin-based ELISA," *Letters in Applied Microbiology*, vol. 39, no. 6, pp. 516 – 522, 2004.

[12] M. Feng, Q. Yong, W. Wang, H. Kuang, L. Wang, and C. Xu, "Development of a monoclonal antibody-based ELISA to detect *Escherichia coli* O157:H7," *Food and Agricultural Immunology*, pp. 1 – 7, 2012.

[13] L. P. Mansfield and S. Forsythe, "The detection of *Salmonella* serovars from animal feed and raw chicken using a combined immunomagnetic separation and ELISA method," *Food Microbiology*, vol. 18, no. 4, pp. 361 – 366, 2001.

[14] E. L. Crowley, C. K. O'Sullivan, and G. G. Guilbault, "Increasing the sensitivity of *Listeria monocytogenes* assays: Evaluation using ELISA and amperometric detection," *Analyst*, vol. 124, pp. 295 – 299, 1999.

[15] A. Sabelnikov, V. Zhukov, and R. Kempf, "Probability of real-time detection versus probability of infection for aerosolized biowarfare agents: A model study," *Biosensors and Bioelectronics*, vol. 21, no. 11, pp. 2070 – 2077, 2006.

[16] K. M. Hong, H. Najjar, M. Hawley, and R. D. Press, "Quantitative real-time PCR with automated sample preparation for diagnosis and monitoring of cytomegalovirus infection in bone marrow transplant patients," *Clinical Chemistry*, vol. 50, no. 5, pp. 846 – 856, 2004.

[17] M. Kubista, J. M. Andrade, M. Bengtsson, A. Forootan, J. Jonák, K. Lind, R. Sindelka, R. Sjöback, B. Sjögreen, L. Strömbom, A. Ståhlberg, and N. Zoric, "The real-time polymerase chain reaction," *Molecular Aspects of Medicine*, vol. 27, no. 23, pp. 95 – 125, 2006.

[18] B. Vogelstein and K. W. Kinzler, "Digital PCR," *Proceedings of the National Academy of Sciences*, vol. 96, no. 16, pp. 9236 – 9241, 1999.

[19] J. Liu, M. Enzelberger, and S. Quake, "A nanoliter rotary device for polymerase chain reaction," *Electrophoresis*, vol. 23, no. 10, pp. 1531 – 1536, 2002.

[20] O. Lazcka, F. J. D. Campo, and F. X. M. noz, "Pathogen detection: A perspective of traditional methods and biosensors," *Biosensors and Bioelectronics*, vol. 22, no. 7, pp. 1205 – 1217, 2007.

[21] P. Belgrader, M. Okuzumi, F. Pourahmadi, D. A. Borkholder, and M. Northrup, "A microfluidic cartridge to prepare spores for PCR analysis," *Biosensors and Bioelectronics*, vol. 14, no. 1011, pp. 849 – 852, 2000.

[22] J. A. Higgins, S. Nasarabadi, J. S. Karns, D. R. Shelton, M. Cooper, A. Gbakima, and R. P. Koopman, "A handheld real time thermal cycler for bacterial pathogen detection," *Biosensors and Bioelectronics*, vol. 18, no. 9, pp. 1115 – 1123, 2003.

[23] C. Almeida, L. Cerqueira, N. Azevedo, and M. Vieira, "Detection of *Salmonella enterica* serovar Enteritidis using real time PCR, immunocapture assay, PNA FISH and standard culture methods in different types of food samples," *International Journal of Food Microbiology*, vol. 161, no. 1, pp. 16 – 22, 2013.

[24] P. G. Klein and V. K. Juneja, "Sensitive detection of viable *Listeria monocytogenes* by reverse transcription-PCR.," *Applied and Environmental Microbiology*, vol. 63, no. 11, pp. 4441 – 4448, 1997.

[25] M. Lund, S. Nordentoft, K. Pedersen, and M. Madsen, "Detection of *Campylobacter* spp. in chicken fecal samples by real-time PCR," *Journal of Clinical Microbiology*, vol. 42, no. 11, pp. 5125 – 5132, 2004.

[26] P. Villari, E. Motti, C. Farullo, and I. Torre, "Comparison of conventional culture and PCR methods for the detection of *Legionella pneumophila* in water," *Letters in Applied Microbiology*, vol. 27, no. 2, pp. 106 – 110, 1998.

[27] http://www.pharmaceutical-market-research.com/publications/finance_investment/biosensors_global_market_overview.html.

[28] S. Huang, H. Yang, R. Lakshmanan, M. Johnson, J. Wan, I.-H. Chen, H. W. III, V. Petrenko, J. Barbaree, and B. Chin, "Sequential detection of *Salmonella typhimurium* and *Bacillus anthracis* spores using magnetoelastic biosensors," *Biosensors and Bioelectronics*, vol. 24, no. 6, pp. 1730 – 1736, 2009.

[29] M. L. Johnson, J. Wan, S. Huang, Z. Cheng, V. A. Petrenko, D.-J. Kim, I.-H. Chen, J. M. Barbaree, J. W. Hong, and B. A. Chin, "A wireless biosensor using microfabricated phage-interfaced magnetoelastic particles," *Sensors and Actuators A: Physical*, vol. 144, no. 1, pp. 38 – 47, 2008.

[30] R. S. Lakshmanan, R. Guntupalli, J. Hu, D.-J. Kim, V. A. Petrenko, J. M. Barbaree, and B. A. Chin, "Phage immobilized magnetoelastic sensor for the detection of *Salmonella typhimurium*," *Journal of Microbiological Methods*, vol. 71, no. 1, pp. 55 – 60, 2007.

[31] J. Wan, H. Shu, S. Huang, B. Fiebor, I.-H. Chen, V. A. Petrenko, and B. A. Chin, "Phage-based magnetoelastic wireless biosensors for detecting *Bacillus anthracis* spores," *IEEE Sensors Journal*, vol. 7, pp. 470 – 477, 2007.

[32] V. A. Petrenko, "Landscape phage as a molecular recognition interface for detection devices," *Microelectronics Journal*, vol. 39, no. 2, pp. 202 – 207, 2008.

[33] G. C. Bokken, R. J. Corbee, F. van Knapen, and A. A. Bergwerff, "Immunochemical detection of *Salmonella* group B, D and E using an optical surface plasmon

resonance biosensor," *FEMS Microbiology Letters*, vol. 222, no. 1, pp. 75 – 82, 2003.

[34] B.-K. Oh, Y.-K. Kim, K. W. Park, W. H. Lee, and J.-W. Choi, "Surface plasmon resonance immunosensor for the detection of *Salmonella typhimurium*," *Biosensors and Bioelectronics*, vol. 19, no. 11, pp. 1497 – 1504, 2004.

[35] D. Zhang, Y. Yan, Q. Li, T. Yu, W. Cheng, L. Wang, H. Ju, and S. Ding, "Label-free and high-sensitive detection of *Salmonella* using a surface plasmon resonance DNA-based biosensor," *Journal of Biotechnology*, vol. 160, no. 34, pp. 123 – 128, 2012.

[36] Y. Wang, W. Knoll, and J. Dostalek, "Bacterial pathogen surface plasmon resonance biosensor advanced by long range surface plasmons and magnetic nanoparticle assays," *Analytical Chemistry*, vol. 84, no. 19, pp. 8345 – 8350, 2012.

[37] T. E. Love, C. Redmond, and C. N. Mayers, "Real time detection of anthrax spores using highly specific anti-EA1 recombinant antibodies produced by competitive panning," *Journal of Immunological Methods*, vol. 334, no. 12, pp. 1 – 10, 2008.

[38] B. H. Schneider, J. G. Edwards, and N. F. Hartman, "Hartman interferometer: versatile integrated optic sensor for label-free, real-time quantification of nucleic acids, proteins, and pathogens," *Clinical Chemistry*, vol. 43, no. 9, pp. 1757 – 1763, 1997.

[39] A. Ramachandran, S. Wang, J. Clarke, S. Ja, D. Goad, L. Wald, E. Flood, E. Knobbe, J. Hryniewicz, S. Chu, D. Gill, W. Chen, O. King, and B. Little, "A universal biosensing platform based on optical micro-ring resonators," *Biosensors and Bioelectronics*, vol. 23, no. 7, pp. 939 – 944, 2008.

[40] J. Qiu, Y. Zhou, H. Chen, and J.-M. Lin, "Immunomagnetic separation and rapid detection of bacteria using bioluminescence and microfluidics," *Talanta*, vol. 79, no. 3, pp. 787 – 795, 2009.

[41] Z. Muhammad-Tahir and E. Alocilja, "Fabrication of a disposable biosensor for *Escherichia coli* O157:H7 detection," *Sensors Journal, IEEE*, vol. 3, pp. 345 – 351, Aug. 2003.

[42] Z. Muhammad-Tahir and E. Alocilja, "A disposable biosensor for pathogen detection in fresh produce samples," *Biosystems Engineering*, vol. 88, no. 2, pp. 145 – 151, 2004.

[43] C. Ruan, H. Wang, and Y. Li, "A bienzyme electrochemical biosensor coupled with immunomagnetic separation for rapid detection of *Escherichia coli* O157:H7 in food samples," *Transactions of the ASABE*, vol. 45, no. 1, pp. 249 – 255, 2002.

[44] L. Yang, C. Ruan, and Y. LI, "Rapid detection of *Salmonella typhimurium* in food samples using a bienzyme electrochemical biosensor with flow injection," *Journal of Rapid Methods & Automation in Microbiology*, vol. 9, no. 4, pp. 229 – 240, 2001.

[45] O. Laczka, J.-M. Maesa, N. Godino, J. del Campo, M. Fougt-Hansen, J. P. Kutter, D. Snakenborg, F.-X. Munoz-Pascual, and E. Baldrich, "Improved bacteria detection by coupling magneto-immunocapture and amperometry at flow-channel microband electrodes," *Biosensors and Bioelectronics*, vol. 26, no. 8, pp. 3633 – 3640, 2011.

[46] C. Ercole, M. D. Gallo, L. Mosiello, S. Baccella, and A. Lepidi, "*Escherichia coli* detection in vegetable food by a potentiometric biosensor," *Sensors and Actuators B: Chemical*, vol. 91, pp. 163 – 168, 2003.

[47] A. G. Gehring, D. L. Patterson, and S.-I. Tu, "Use of a light-addressable potentiometric sensor for the detection of *Escherichia coli* O157:H7," *Analytical Biochemistry*, vol. 258, no. 2, pp. 293 – 298, 1998.

[48] G. A. Zelada-Guillén, J. L. Sebastián-Avila, P. Blondeau, J. Riu, and F. X. Rius, "Label-free detection of *Staphylococcus aureus* in skin using real-time potentiometric biosensors based on carbon nanotubes and aptamers," *Biosensors and Bioelectronics*, vol. 31, no. 1, pp. 226 – 232, 2012.

[49] M. dos Santos, J. Agusil, B. Prieto-Simn, C. Sporer, V. Teixeira, and J. Samitier, "Highly sensitive detection of pathogen *E. coli* O157:H7 by electrochemical impedance spectroscopy," *Biosensors and Bioelectronics, In Press, Accepted Manuscript*, 2013.

[50] Y. Luo, S. Nartker, H. Miller, D. Hochhalter, M. Wiederoder, S. Wiederoder, E. Setterington, L. T. Drzal, and E. C. Alocilja, "Surface functionalization of electrospun nanofibers for detecting *E. coli* O157:H7 and BVDV cells in a direct-charge transfer biosensor," *Biosensors and Bioelectronics*, vol. 26, no. 4, pp. 1612 – 1617, 2010.

[51] R. Hao, D. Wang, X. Zhang, G. Zuo, H. Wei, R. Yang, Z. Zhang, Z. Cheng, Y. Guo, Z. Cui, and Y. Zhou, "Rapid detection of *Bacillus anthracis* using monoclonal antibody functionalized QCM sensor," *Biosensors and Bioelectronics*, vol. 24, no. 5, pp. 1330 – 1335, 2009.

[52] D. W. Branch and S. M. Brozik, "Low-level detection of a *Bacillus anthracis* simulant using Love-wave biosensors on 36° YX $LiTaO_3$," *Biosensors and Bioelectronics*, vol. 19, no. 8, pp. 849 – 859, 2004.

[53] A. P. Davila, J. Jang, A. K. Gupta, T. Walter, A. Aronson, and R. Bashir, "Microresonator mass sensors for detection of *Bacillus anthracis* Sterne spores in air and water," *Biosensors and Bioelectronics*, vol. 22, no. 12, pp. 3028 – 3035, 2007.

[54] G. A. Campbell and R. Mutharasan, "Detection of *Bacillus anthracis* spores and a model protein using PEMC sensors in a flow cell at 1 mL/min," *Biosensors and Bioelectronics*, vol. 22, no. 1, pp. 78 – 85, 2006.

[55] L. Fu, K. Zhang, S. Li, Y. Wang, T.-S. Huang, A. Zhang, and Z.-Y. Cheng, "In situ real-time detection of *E. coli* in water using antibody-coated magnetostrictive microcantilever," *Sensors and Actuators B: Chemical*, vol. 150, no. 1, pp. 220 – 225, 2010.

[56] J. Wan, M. L. Johnson, R. Guntupalli, V. A. Petrenko, and B. A. Chin, "Detection of *Bacillus anthracis* spores in liquid using phage-based magnetoelastic micro-resonators," *Sensors and Actuators B: Chemical*, vol. 127, no. 2, pp. 559 – 566, 2007.

[57] M. Jantunen, O. Hänninen, K. Koistinen, and J. Hashim, "Fine PM measurements: personal and indoor air monitoring," *Chemosphere*, vol. 49, no. 9, pp. 993 – 1007, 2002.

[58] P. M. Irving, "Air sampling technology: A requirement for biodetection," in *Materials of the Second International Symposium on Detection Technologies, Knowledge Foundation*, (Arlington, VA, USA), December 2002.

[59] http://www.sceptorindustries.com.

[60] M. Allan and G. M. Richardson, "Probability density functions describing 24 h inhalation rates for use in human health risk assessments," *Human and Ecological Risk Assessment*, vol. 4, no. 2, pp. 379 – 408, 1998.

[61] C. J. Peters and D. M. Hartley, "Anthrax inhalation and lethal human infection," *The Lancet*, vol. 359, pp. 710 – 711, 2002.

Chapter 3

Phage-Based Magnetoelastic (ME) Biosensors

Biosensors can be potential alternatives to the conventional bacterial detection methods. However, as described in the previous chapters, the performance of existing biosensors still needs to be improved. In this chapter, the fundamentals of phage-based ME biosensors, a novel class of wireless, mass-sensitive biosensors, will be described in depth.

3.1 Landscape phages as biomolecular-recognition elements

For the past decades, antibodies have been the most commonly used biomolecular-recognition elements [2]. However, their use in on-site bacterial detection might be restricted by such factors as thermal stability, selectivity, and production cost [1,3,4]. Hence, as emerging alternatives, landscape phages have attracted growing attention, and their application to various biosensing systems has been recently reported [3,5–8]. Table 3.1 compares the longevity of a landscape phage and monoclonal antibody specific for β-galactosidase tested at various temperatures [1]. As can be seen, both

Table 3.1: Longevity of a landscape phage and monoclonal antibody at various temperatures.

Temperature	**Landscape phage**	**Antibody**	**Ref.**
Room temp.	$>$ 6 months	$>$ 6 months	[1]
37 °C	950 days (half-life)	107 days (half-life)	[1]
50 °C	5 weeks (half-life)	5 weeks	[1]
63 °C	6 weeks	24 hr	[1]
76 °C	2.4 days	No binding activity	[1]

phage and antibody retain their binding activities at room temperature for greater than 6 months. However, the antibody degrades much faster than the phage at higher temperatures. For on-site bacterial detection, where a wide range of temperatures are anticipated, a high thermal stability with a fair life time is essential for a biomolecular-recognition element. In addition, as shown in Table 3.2, a high selectivity and low production cost are distinct advantages of landscape phages over antibodies.

Table 3.2: Comparison between landscape phages and antibodies in terms of selectivity and production cost.

Recognition element	**Selectivity**	**Production cost**	**Ref.**
Landscape phage	High	Low	[1, 3, 4]
Monoclonal antibody	High	Very high	[1, 4]
Polyclonal antibody	Low	High	[1, 4]

Landscape phages are genetically engineered phages that can be synthesized through the phage display technology [9, 10]. This technology, primarily developed

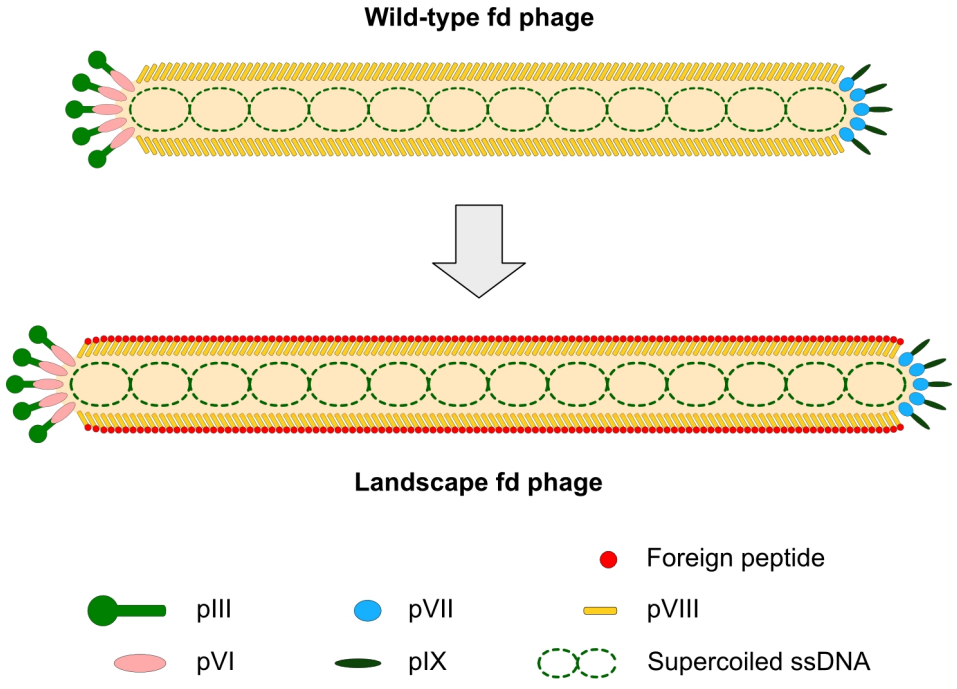

Figure 3.1: Schematic illustration of the wild-type fd phage and its genetically engineered form, displaying a foreign peptide on the major coat protein pVIII.

for the Ff class of filamentous phage strains (i.e., fd, f1, and M13), enables one to construct billions of phage clones that display engineered sequences of peptides on their outer surfaces. For example, Fig. 3.1 shows a schematic illustration of the wild-type fd phage (top) and its genetically engineered form (bottom), displaying a foreign peptide on the major coat protein pVIII.

The wild-type Ff phage strains, which possess virtually identical DNA sequences, are flexible, thread-like particles about 800 to 900 nm long and 6.5 nm in diameter [1]. They consist of a circular single-stranded DNA ($\approx$ 6,400 nucleotides) enclosed in a tube of helically arranged molecules of coat proteins (the N-termini exposed on the outer surface and C-termini in the lumen) [10, 11]. There are approximately 2,700 copies of the major coat protein pVIII along the tube's length, accounting for 98% by mass [1]. In addition, five copies each of the minor coat proteins cap both ends

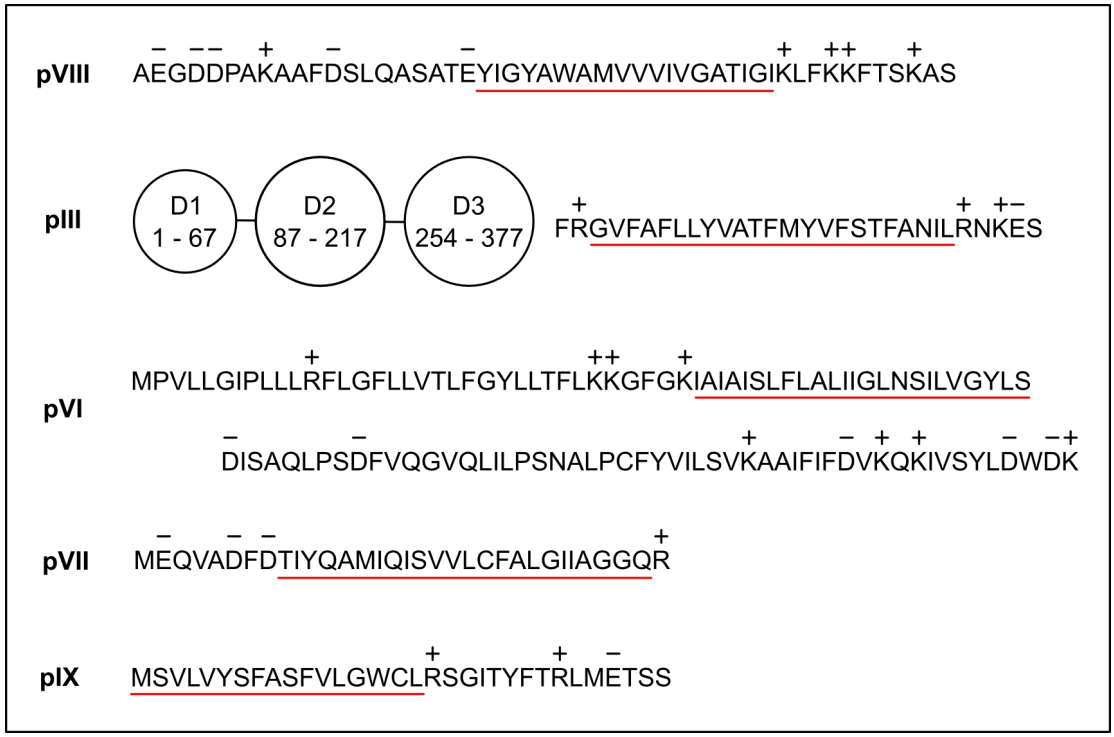

Figure 3.2: Sequences of amino acid residues of the fd coat proteins. The N-terminus is to the left. The hydrophobic domains are underlined, whereas charged residues are indicated by + or -.

of the tube (The minor coat protein pIII and pVI are at one end, whereas the pVII and pIX proteins are at the other end.). Figure 3.2 shows the sequences of amino acid residues of the fd coat proteins (The N-terminus is to the left.) [12]. The sizes of these proteins are: pVIII, 50 residues; pIII, 406 residues; pVI, 112 residues; PVII, 33 residues; and pIV, 32 residues. The N-terminal portion of the protein pIII can be considered as three distinct domains, separated by striking glycine-rich tandem repeat linkers of GGGS and EGGGS between the domains [12]. The numbers within the circles represent amino acid residues assigned to each domain. In the above figure, apolar, hydrophobic domains are underlined, whereas charged residues are indicated by + or -. The major coat protein pVIII, for example, has a hydrophobic domain of continuous 19 amino acid residues (YIGYAWAMVVVIVGATIGI) in the interior of its sequence. Adjacent copies of this protein in the phage virion are held together by hydrophobic interactions between these domains [12]. In addition, the positively charged residues near the C-terminus neutralize the negative charge of the DNA core. Furthermore, all the four minor coat proteins also possess hydrophobic domains similar in length to the hydrophobic domain of pVIII, suggesting that these minor coat proteins may associate with pVIII by hydrophobic interactions [12]. According to Endemann and Model [13], the minor coat proteins pIII, pVI, and pVII all interact with the major coat protein pVIII in phage. Also, the pIII and pIX proteins are exposed to the environment, whereas the pVI and PVII proteins are shielded from the environment.

These wild-type Ff phages are viruses that infect the bacterium *Escherichia coli* bearing F pili. Infection is initiated by the attachment of the N-terminal domain of the pIII protein to the tip of the pilus [10]. As the process continues, the coat proteins dissolve into the surface envelope of the cell, and the viral DNA alone enters the cytoplasm, where a vast number of progeny viral DNA molecules are synthesized by host machinery. These progeny viral DNA molecules are, then, extruded through

the cell envelope, acquiring the coat proteins from the cell membrane and emerging as completed virions [10]. Up to 1,000 progeny virions per cell per division can be secreted continuously without killing the host cell [1], leading to a low production cost. The yield of virions can exceed 0.3 mg/mL [10].

In phage display constructions, a foreign coding sequence is spliced in-frame into one of the five coat protein genes. The resultant foreign peptide encoded by this sequence can be fused to the coat protein and, thereby, displayed on the surface of the virion. In addition, the subsequent length of the phage capsid (i.e., the protein shell of the phage) is altered to match the size of the enclosed recombinant DNA by adding proportionally more pVIII subunits during phage assembly [14].

In this research, three phage clones (E2, JRB7, and SAE10), displaying foreign octamers or nanomers in approximately 4,000 copies of the major coat protein pVIII, were derived from the landscape phage libraries f8/8 and f8/9 [14–16] and used as biomolecular-recognition elements. As shown in Fig. 3.3, three amino acid residues (EGD) of the wild-type pVIII are replaced by a random octamer in the f8/8 library, whereas four residues (EGDD) are replaced by a random nanomer in the f8/9 library, bringing the total size of both fusion pVIII proteins to 55 amino acids. Here, the symbol x represents any amino acid residue. About a half of the pVIII peptide

Figure 3.3: Sequences of amino acid residues of the wild-type and fusion pVIII proteins.

sequence is exposed to the environment, whereas the other half is buried in the capsid [1]. The foreign peptide sequence for each phage clone is shown in Table 3.3.

Table 3.3: Phage clones used in this research.

Phage	**Foreign peptide sequence**	**Target pathogen or analyte**	**Ref.**
E2	VTPPTQHQ	*S.* Typhimurium	[15]
JRB7	EPRLSPHS	*B. anthracis*	[16]
SAE10	VPVGAYSDT	Streptavidin	[14]

3.2 Magnetoelasticity

Any magnetic materials exhibit magnetoelastic (ME) behaviour. In other words, the dimensions and elastic properties of these materials are dependent upon their magnetic states, and their magnetic properties are, by contrast, influenced by internal as well as applied mechanical stresses [17]. Magnetoelasticity has been observed not only in ferromagnets but also in ferrimagnets, antiferrimagnets, paramagnets, and even daimagnets with low susceptibilities [17]. However, from a technical point of view, ferromagnets have been extensively studied for the past centuries. In this work, two amorphous ferromagnets, Metglas Alloy 2826MB and $Fe_{79}B_{21}$, were used for the construction of ME signal transducers.

3.2.1 Joule magnetostriction

An ME material undergoes a change in its dimensions during the process of magnetization. This phenomenon is known as Joule magnetostriction, discovered by and named after James P. Joule [17]. A spherical ME material, for example, may be transformed into an ellipsoid when subjected to an externally applied magnetic field, H, as illustrated in Fig. 3.4. The induced strains measured in the directions parallel and perpendicular to the field, $\lambda_{\parallel}$ and $\lambda_{\perp}$, are largely dependent on the field strength

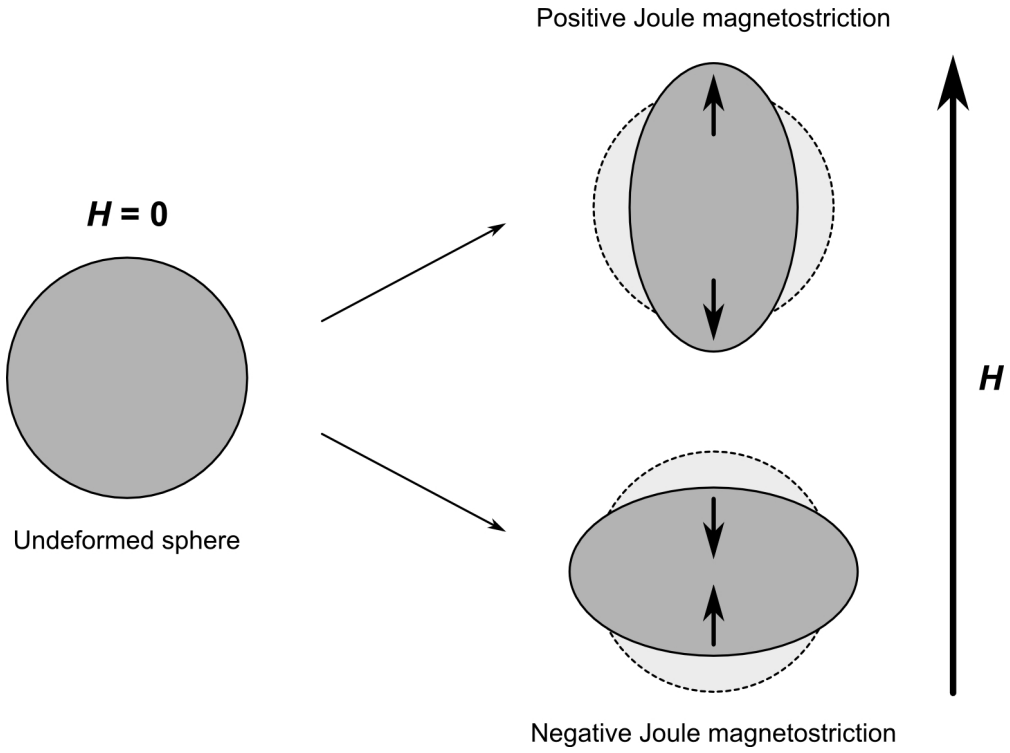

Figure 3.4: Joule magnetostriction of a spherical ME material.

and can be positive or negative, depending on whether the material's deformation is expansive or compressive. These strains reach their limiting values when the material becomes magnetically saturated. From the hypothetical λ – H relationships shown in Fig. 3.5, the saturation Joule magnetostriction, λ_s, can be defined as [18]

$$\lambda_s = \frac{2}{3}(\lambda_{\parallel} - \lambda_{\perp}), \tag{3.1}$$

where $\lambda_{\parallel}$ and $\lambda_{\perp}$ are determined by the extrapolation of the tangents of the linear field dependencies of the strains at the saturated state down to $H = 0$. λ_s is equal to $\lambda_{\parallel}$ when the demagnetized state of the material is isotropic (i.e., $\lambda_{\parallel}/2\lambda_{\perp} = 1$). However, for actual materials, the value of $\lambda_{\parallel}/2\lambda_{\perp}$ is often not equal to 1, depending on both intrinsic parameters (e.g., magnetocrystalline anisotropy) and sample parameters (e.g., demagnetizing field and internal stresses) [17]. Hence, Eq. 3.1, which

remains independent of the demagnetized state of the material, is preferably used to determine λ_s.

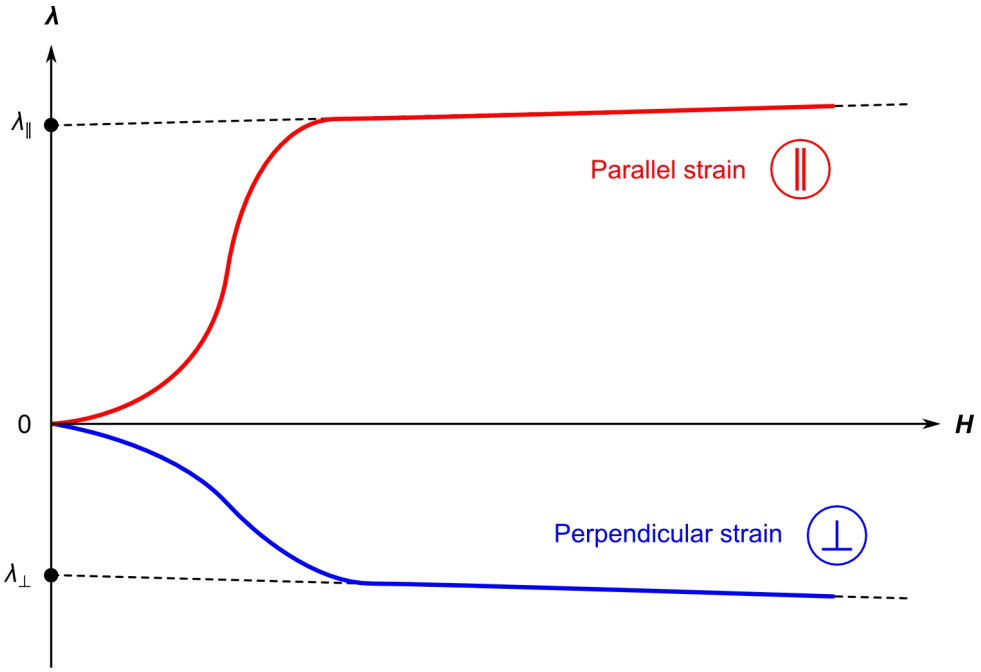

Figure 3.5: Hypothetical field dependencies of $\lambda_{\parallel}$ and $\lambda_{\perp}$.

3.2.2 Magnetization and Joule magnetostriction in ferromagnets

When demagnetized at temperatures lower than its Curie temperature, a ferromagnetic material is divided into a number of magnetic domains to minimize the material's internal energy as schematically illustrated in Fig. 3.6. Each magnetic domain is magnetized in a different direction such that the net magnetization is zero or small. Between any two adjacent domains, the elementary magnetic moments rotate gradually from one easy magnetization direction (D_i) to another (D_j) [17]. When a magnetic field, H, is applied in any given direction, the following processes occur within the material:

1. The domain D_1, whose magnetization direction is the closest to the field direction, expands at the expense of the domain D_3 through the displacement of the 180° domain wall.

2. The magnetization in the domain D_4 is reversed so that the net magnetization is minimized.

3. When a stronger field is applied, the domain D_1 further expands at the expense of the domains D_2 and D_4 (90° domain wall displacement), resulting in the formation of only one single domain D_1.

4. Finally, the magnetization in this single domain rotates out of its easy magnetization direction (D_1) and aligns along the field direction.

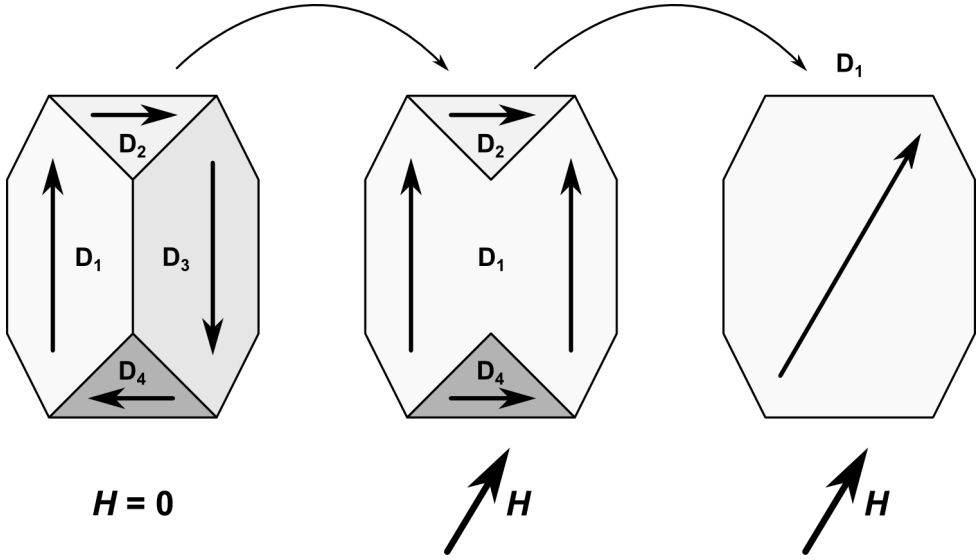

Figure 3.6: Magnetic domains and magnetization processes in a ferromagnet.

During the above magnetization processes, the material is strained due to the ME coupling since the distribution of the elementary magnetic moments becomes anisotropic (upper left illustration in Fig. 3.7a). This anisotropic distribution of magnetic moments may also be induced when an ME material is mechanically stressed (upper right illustration in Fig. 3.7a). As a result, spontaneous Joule magnetostriction is also induced, again due to the ME coupling. When a magnetic field is, then, applied to this material, $\lambda_{\parallel}$ becomes a function of the applied pre-stress [17]. In the case of positive Joule magnetostriction, a compressive stress orients the magnetic moments into the direction perpendicular to the stress direction. Such field

and stress dependence of $\lambda_{\|}$ is shown in Fig. 3.7b. As can be seen, $\lambda_{\|}$ is increased with larger pre-stresses, which rotate more magnetic moments (Note that λ_s is, by contrast, usually nearly stress-independent [17].).

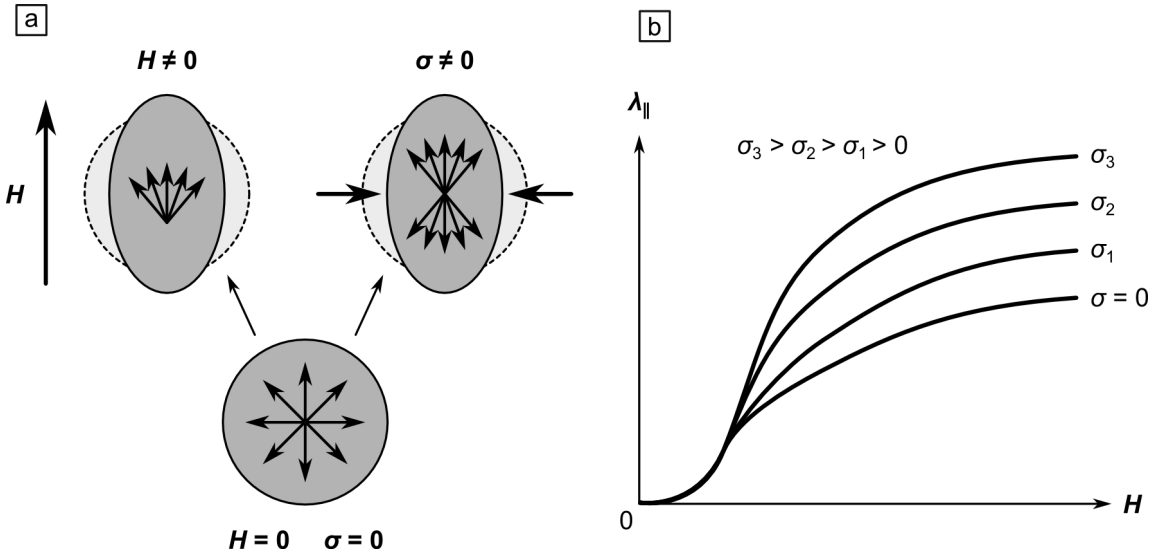

Figure 3.7: (a) Effects of magnetizing field and mechanical stress on the distribution of magnetic moments in a ferromagnet and (b) field dependence of $\lambda_{\|}$ under a compressive stress.

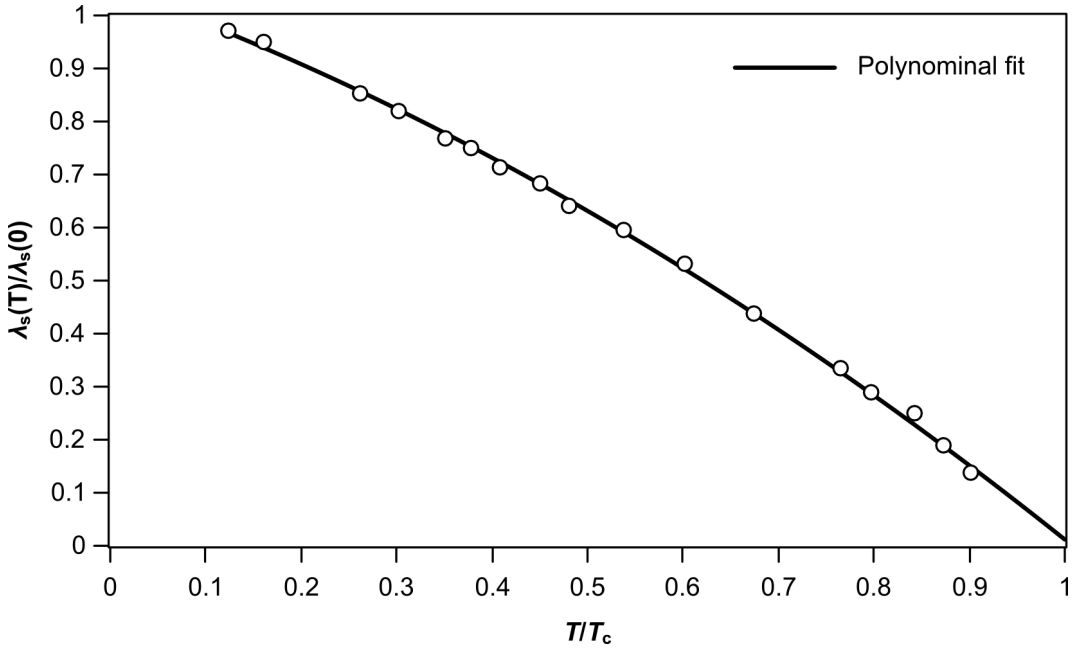

Figure 3.8: Temperature dependence of normalized λ_s in $Fe_{80}B_{20}$.

Joule magnetostriction is also temperature dependent. The thermal dependence of λ_s is usually monotonous as in the case for $Fe_{80}B_{20}$, shown in Fig. 3.8, where T_c is the Curie temperature [17].

3.2.3 ME signal transducers

An ideal material for the construction of ME signal transducers is a magnetically soft material that possesses a high saturation Joule magnetostriction, λ_s, and a high magnetomechanical coupling factor, k, which can be defined as [17]

$$k = \frac{E_{me}}{\sqrt{E_e E_m}}, \tag{3.2}$$

where E_{me}, E_e, and E_m are the mutual elastic and magnetic energy density, elastic self-energy density, and magnetic self-energy density, respectively. This coupling factor can be used to characterize the material's ability to convert a magnetic energy into an elastic energy and vice versa. Traditionally, Metglas Alloy 2826MB (from Honeywell International) with a composition of $Fe_{40}Ni_{38}Mo_4B_{18}$ has been the material for ME signal transducers. This amorphous, ferromagnetic alloy is mechanically robust (e.g., tensile strength of 1 to 2 GPa), and it possesses reasonably high λ_s and k values [19–22]. In addition, the alloy has a low material cost, allowing ME signal transducers made of this alloy to be used on a disposable basis [23].

In recent years, another amorphous, ferromagnetic alloy with a composition close to $Fe_{80}B_{20}$ has also been used for the construction of ME signal transducers [7, 24]. This iron-rich alloy can be easily produced through physical or electrochemical deposition processes. Hence, by combining with standard microelectronic fabrication techniques, batch fabrication of miniature ME signal transducers is also possible, which further reduces the fabrication cost. Some important materials properties for the above alloys are summarized in Table 3.4.

Table 3.4: Materials properties for Metglas 2826MB and $Fe_{80}B_{20}$.

Property	**Metglas 2826MB**	**Ref.**	**$Fe_{80}B_{20}$**	**Reference**
Elastic modulus [GPa]	100 to 110	[22]	166	[25]
Density [$\times 10^3$ kg/m^3]	7.9	[22]	7.4	[25]
Poisson's ratio	0.33	[26]	0.3	[27]
Saturation magnetostriction, λ_s [ppm]	12	[22]	32	[28]
Magnetomechanical coupling factor, k	~ 0.98	[23]	~ 0.64	[29]

3.3 Fabrication of ME sensor platforms

Depending on the size of sensor platforms (i.e., ME signal transducers), two different fabrication methods were employed. A dicing method was used for millimeter-scale sensor platforms (0.5 to 4-mm long), while a co-sputtering-based method was used for micron-scale sensor platforms (100 to 500-μm long).

3.3.1 Dicing method

A ribbon of Metglas Alloy 2826MB was purchased from Honeywell International. Small pieces with a size of 50 mm $\times$ 12.7 mm $\times$ 30 μm were cut from the ribbon and double-side polished down to a thickness of 15 μm. The polished pieces were, then, diced into millimeter-scale strip-shaped sensor platforms (Fig. 3.9) using a automated dicing saw. After cleaning with acetone and ethanol in an ultrasonic bath, these diced sensor platforms were successively coated with thin layers of Cr (90 nm) and Au (150 nm) by electron-beam induced deposition. The Cr layer acts as an adhesive interlayer between the Au layer and sensor platform. The Au layer provides corrosion resistance as well as a ready surface for the immobilization of the phages.

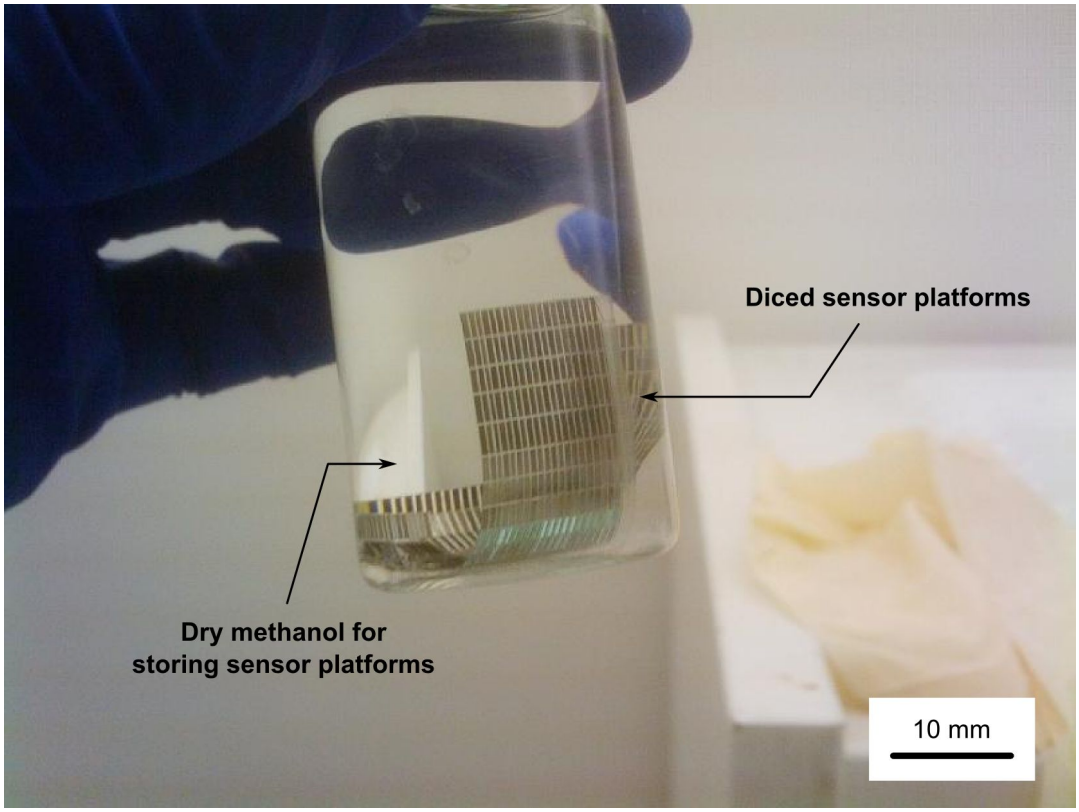

Figure 3.9: Diced sensor platforms stored in dry methanol.

3.3.2 Co-sputtering-based method

Micron-scale ME sensor platforms were batch-fabricated using a co-sputtering-based method reported previously [7]. The fabrication procedure is diagrammed in Fig. 3.10. First, a four-inch gold-coated wafer was photolithographically patterned with 10-μm thick rectangular islands of the STR-1045 photoresist (from Rohm and Haas Electronic Materials, LLC). The lateral dimensions of these photoresist islands were kept the same as those of sensor platforms of target size. Next, the patterned wafer was successively deposited with 50-nm thick Au, 4-μm thick $Fe_{79}B_{21}$ (i.e., co-sputtering of Fe and B), and another 50-nm thick Au using a Denton sputter coater (Fig. 3.11). Then, the Au-enclosed $Fe_{79}B_{21}$ alloy on the photoresist islands was lifted off the wafer to become freestanding ME sensor platforms by dissolving the underlying photoresist with acetone. This method not only ensures the dimensional

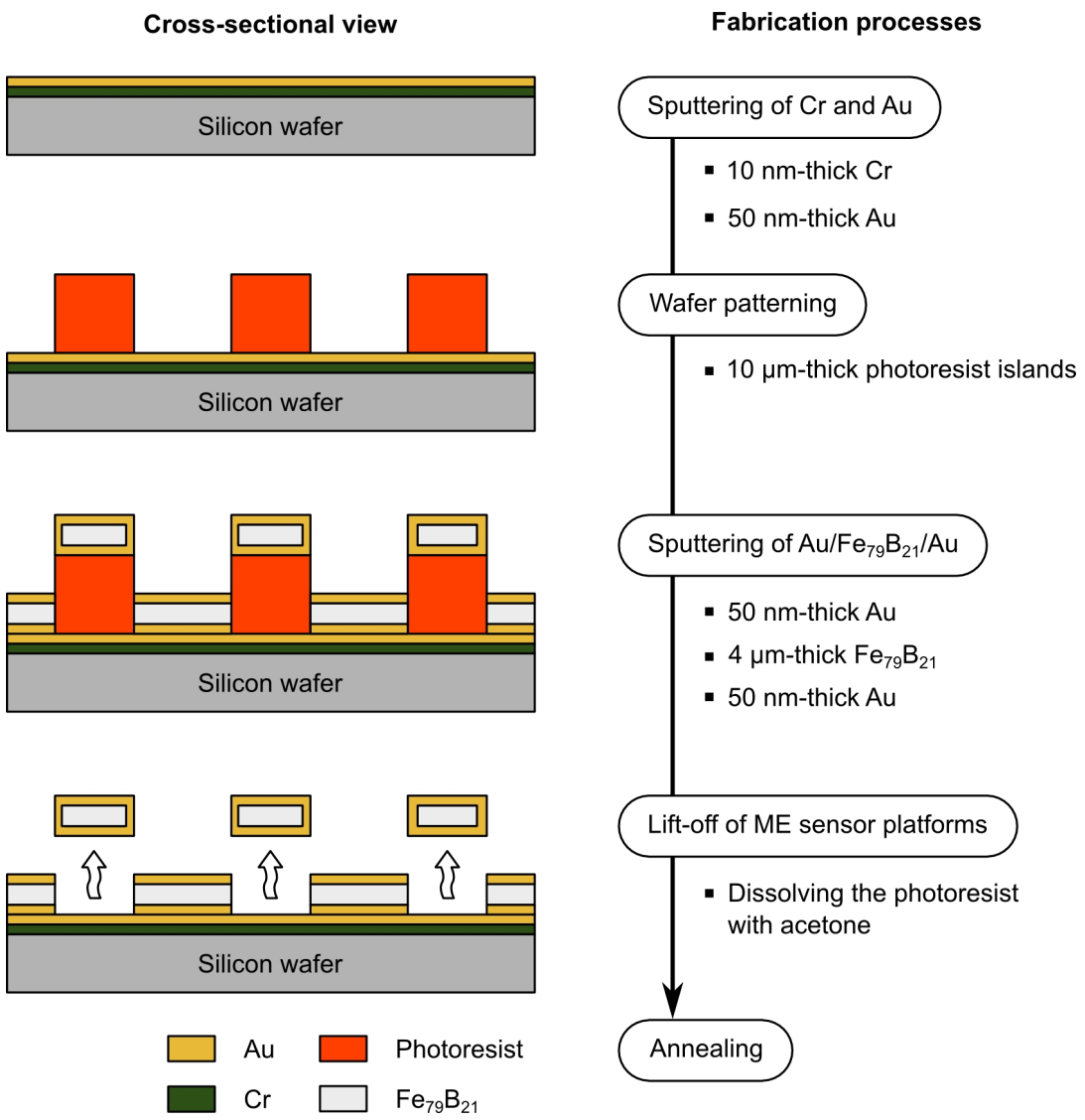

Figure 3.10: Procedure for the co-sputtering-based method.

consistency of the fabricated sensor platforms but also greatly reduces the fabrication cost per sensor platform due to the batch fabrication process (See Fig. 3.12, showing batch-fabricated sensor platforms with a size of 100 μm $\times$ 25 μm $\times$ 4 μm.).

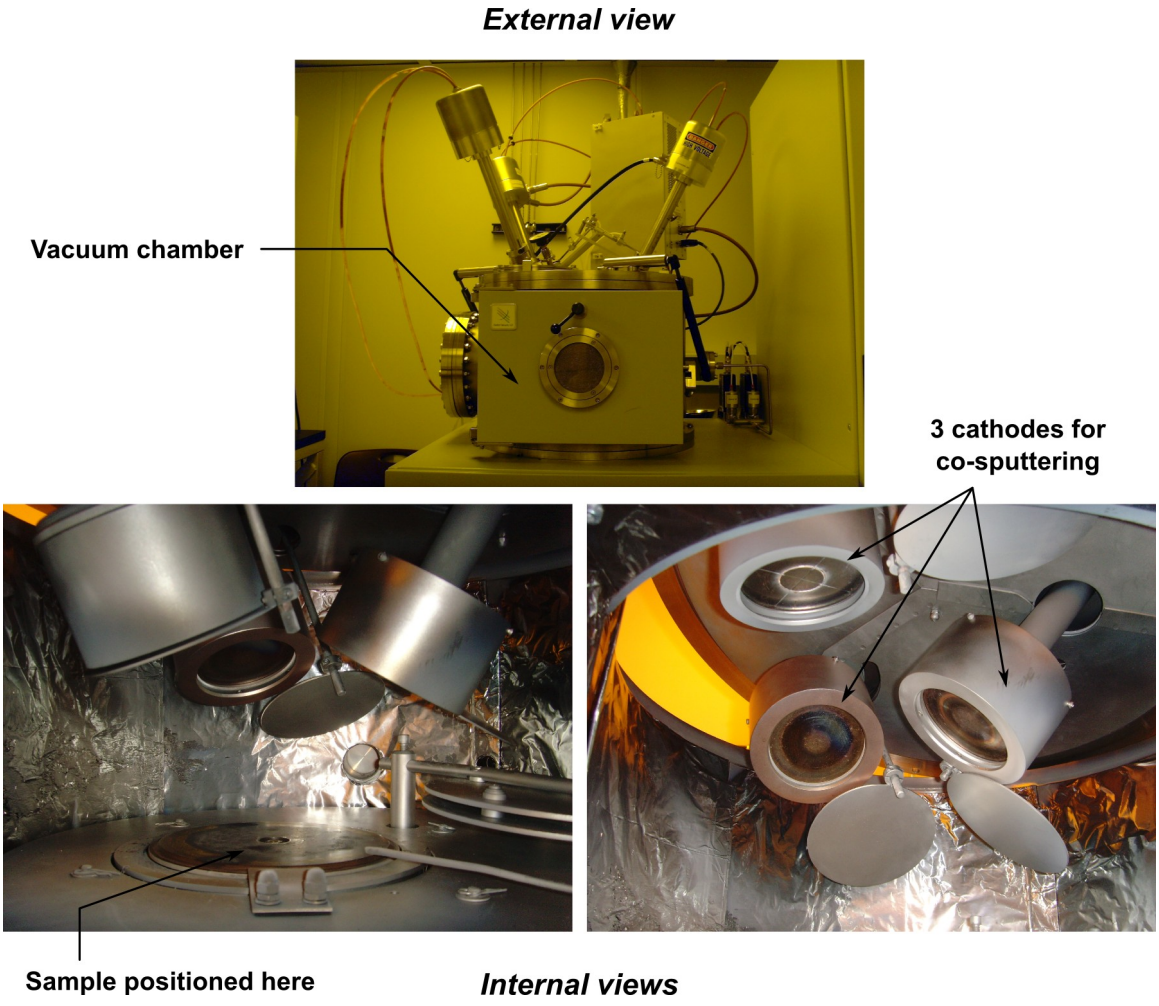

Figure 3.11: Denton sputter coater.

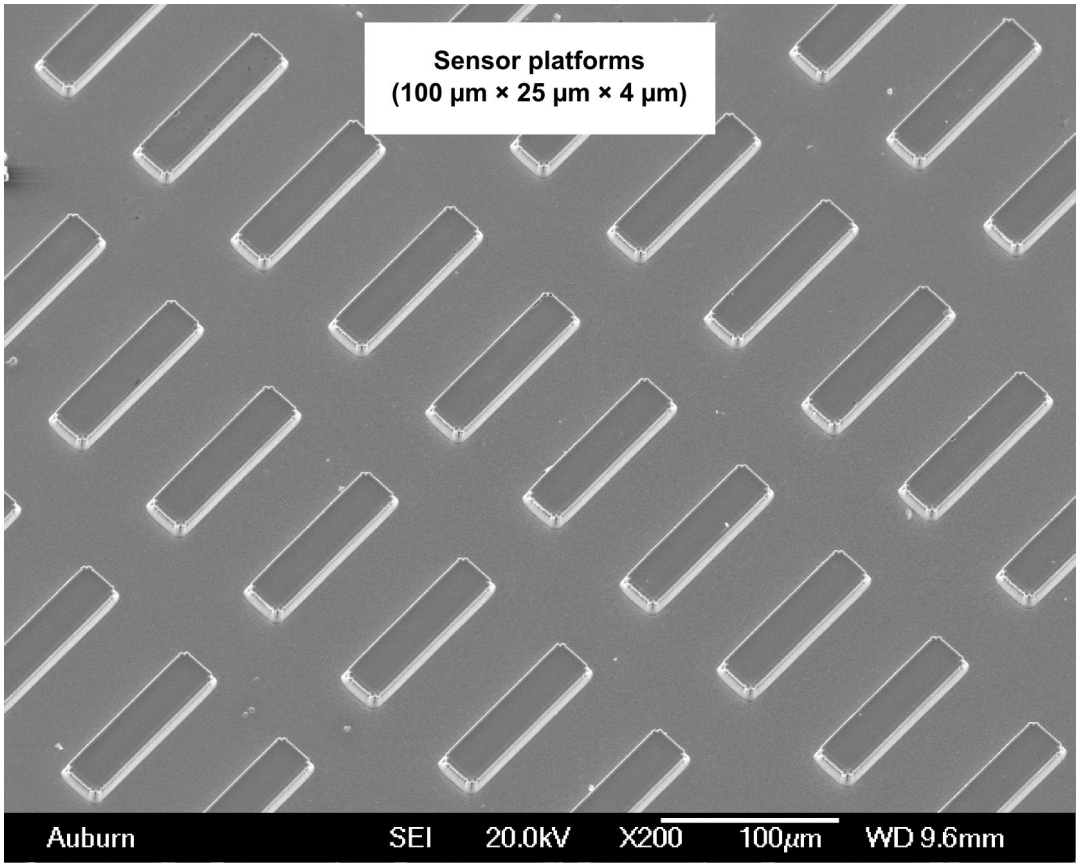

Figure 3.12: Scanning electron micrograph of batch-fabricated sensor platforms with a size of 100 μm $\times$ 25 μm $\times$ 4 μm on a gold-coated wafer.

The sputtering conditions used are summarized in Table 3.5. Prior to sputtering, the chamber was pumped down to 7×10^{-7} Torr in order to minimize residual oxygen in the fabricated sensor platforms. In addition, during the deposition process, the sample stage was rotated so that the uniformity of the deposits can be guaranteed.

Table 3.5: Sputtering conditions used for the fabrication of micron-scale sensor platforms.

Target	**Cathode type**	**Power [W]**	**Time [sec]**	**Ar flow rate [sccm]**
Cr	DC	50	100	25
Au	DC	100	200 $\times$ 3 times	12
Fe	DC	41	64,000	30
B	RF	100	64,000	30

3.3.3 Annealing

The fabricated sensor platforms were finally annealed in vacuum at 220 °C for 2 h to relieve residual internal stresses and minimize the effects of any surface defects from the fabrication processes [30]. This temperature was chosen because it is high enough to effectively anneal the sensor platforms within a reasonable time, yet it is still far below the Curie temperatures as well as the recrystallization temperatures of the ME materials [7].

3.3.4 Fabrication cost per sensor platform

As discussed in Chapter 1, cost is an important factor for the on-site detection of pathogens because proper allocation of limited resources is essential to improving overall safety. Through the batch fabrication of micron-scale sensor platforms, great reduction in fabrication cost can be realized. For a rough estimation of the fabrication cost per sensor platform, the following assumptions were made:

1. The size of sensor platforms to be fabricated is 200 μm $\times$ 40 μm $\times$ 4 μm, and their composition is $Fe_{79}B_{21}$.

2. The size of a silicon wafer on which sensor platforms will be fabricated is four inches in diameter. 80% of the wafer surface area will be used.

3. Only the material costs for metals to be sputtered (i.e., Cr, Au, Fe, and B as shown in Table 3.6) and the silicon wafer ($\approx$ \$20) are considered. In other words, the costs for the STR-1045 photoresist and other required chemicals are not considered.

4. The metals will be sputter-deposited only on the wafer.

5. The electricity costs for photolithography, annealing, and other fabrication processes are not considered. Only the energy charges for sputtering are considered.

An electricity rate of 7.49¢/kWh paid by Auburn University in FY 2009 [31] is used.

Table 3.6: Material costs for the sputtering targets.

Material	**Cost [$/g]**	**Density [g/cm^3]**	**Deposit's thickness**	**Ref.**
Cr	≈ 1	7.2	10 nm	[32]
Au	≈ 75	19.3	150 nm (50 nm $\times$ 3)	[33]
Fe	≈ 2	7.9	3.2 μm (79% of 4 μm)	[34]
B	≈ 2	2.3	0.8 μm (21% of 4 μm)	[35]

Hence, the fabrication cost per sensor platform, C_{sensor}, can be calculated by

$$\begin{aligned} C_{\text{sensor}} &= \frac{\text{material costs} + \text{energy charges}}{\text{number of sensors}} \\ &= \Big[\sum(M_i \times \rho_i \times V_i) + \text{wafer cost} \\ &+ \sum(P_i \times T_i \times \$0.0749/\text{kWh})\Big]/N_{\text{sensor}}, \qquad (3.3) \\ i &= \text{Cr, Au, Fe, or B,} \end{aligned}$$

where M, ρ, and V represent the material cost (per gram), density, and volume for each sputtered metal; P and T denote the power (in kilo-watts) and time (in hours) for sputtering; and N_{sensor} is the number of sensors to be fabricated on the wafer. By using the values shown in Tables 3.5 and 3.6,

$$\begin{aligned} C_{\text{sensor}} &= (\$5.8 \times 10^{-4} + \$1.8 + \$4.1 \times 10^{-1} + \$3.0 \times 10^{-2} + \$20 \\ &+ \$1.0 \times 10^{-4} + \$1.3 \times 10^{-3} + \$5.5 \times 10^{-2} + \$1.3 \times 10^{-1})/8.1 \times 10^{5} \text{ sensors} \\ &\approx \$2.8 \times 10^{-5}. \qquad (3.4) \end{aligned}$$

3.4 Fabrication of phage-based ME biosensors

3.4.1 Immobilization of a phage on the ME sensor platforms

The annealed sensor platforms were individually immersed in 330 μl of a phage suspension (usually, phage in a tris-buffered saline (TBS) buffer solution, 5×10^{11} vir/ml) in a polypropylene PCR tube. The tubes were, then, rotated with a Barnstead LabQuake tube rotator (from Fisher Scientific, Inc.) at 8 rpm for 1 h. In this way, the phage was allowed to uniformly attach to platform surfaces via physical adsorption. Finally, these phage-immobilized ME biosensors (i.e., measurement sensors) were thoroughly rinsed with sterile distilled water to remove any TBS buffer components as well as loosely attached phages from the platform surfaces. Covalent immobilization of a phage on the surface of sensor platforms will be described in Chapter 6.

3.4.2 Surface blocking of the ME biosensors with bovine serum albumin

In order to reduce non-specific adsorption of *S.* Typhimurium cells or *B. anthracis* spores on biosensor surfaces, surface blocking with bovine serum albumin (BSA) was performed. The prepared measurement sensors were individually immersed in a 330-μl solution of BSA (0.01 to 1 % w/v in sterile distilled water) in a PCR tube. After 40 min of tube rotation at 8 rpm, the biosensors were collected from the solution and thoroughly rinsed with sterile distilled water to be ready for use. Control sensors, which are not immobilized with phage but only surface-blocked with BSA, were also prepared and used for background subtraction.

3.5 Principle of detection

The fabricated ME biosensors are made from one of the magnetostrictive alloys (i.e., Metglas 2826MB or $Fe_{79}B_{21}$). Hence, the biosensors can be placed into magneto-mechanical resonance when subjected to an externally applied magnetic field that alternates at the right frequency. For a freestanding, strip-shaped biosensor, the fundamental resonant frequency of longitudinal vibration, f, can be expressed by [26]

$$f = \frac{1}{2L}\sqrt{\frac{E}{\rho(1-\nu)}}, \tag{3.5}$$

where L, E, ρ, and ν denote the length, modulus of elasticity, density, and Poisson's ratio of the biosensor, respectively. When the biosensor and bacterial cells (or spores) come into contact with each other, the phage that is immobilized on the biosensor binds with the cells (or spores) (Fig. 3.13), thereby increasing the total mass of the biosensor. This change in mass causes a corresponding decrease in the biosensor's resonant frequency, which is the principle of detection. In addition, for uniform mass attachment, the mass sensitivity of the biosensor, S_{m}, defined as the ratio of the resonant frequency change, Δf, to the mass change Δm, can be approximated

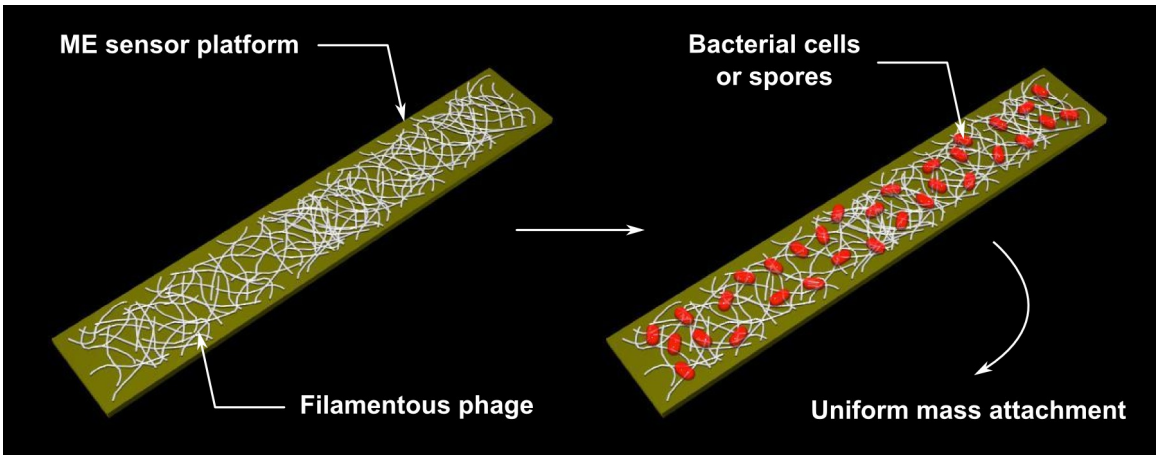

Figure 3.13: Uniform attachment of bacterial cells or spores on a phage-immobilized ME biosensor.

by [23, 36]

$$S_{\mathrm{m}} = \frac{\Delta f}{\Delta m} \approx -\frac{1}{4L^2WT}\sqrt{\frac{E}{\rho^3(1-\nu)}}, \tag{3.6}$$

where W and T represent the width and thickness of the biosensor, respectively. Equation 3.6 describes that the mass sensitivity is largely dependent on the size of the biosensor and inversely proportional to L^2WT.

3.5.1 Minimum detectable number of bacterial cells

Table 3.7 shows ME biosensors of different size and their theoretical detection limits in terms of the minimum detectable number of bacterial cells, N_{min}. The first four biosensors from the top are made of Metglas 2826MB, whereas the rest is made of $Fe_{79}B_{21}$. By rearranging Eq. 3.6, the minimum detectable mass change, Δm_{min}, can be calculated by

$$\Delta m_{\mathrm{min}} = \frac{\Delta f_{\mathrm{min}}}{S_{\mathrm{m}}}, \tag{3.7}$$

where Δf_{min} represents the corresponding minimum detectable frequency change. If the mass of a single bacterial cell is assumed to be 1 pg [37], and a frequency shift of 1,000 Hz (i.e., Δf_{min} = 1,000 Hz) can be resolved, the minimum detectable number of bacterial cells, N_{min}, can then be computed by

$$N_{\mathrm{min}} = \frac{\Delta m_{\mathrm{min}}}{1\text{ pg}} = \frac{\frac{\Delta f_{\mathrm{min}}}{S_{\mathrm{m}}}}{1\text{ pg}} = \frac{1{,}000\text{ Hz}}{1\text{ pg}} \times \frac{1}{S_{\mathrm{m}}}, \tag{3.8}$$

where N_{min} is an integer. As can be seen in the table, detection of a single bacterial cell may be possible with a 50 μm $\times$ 10 μm $\times$ 2 μm sensor.

Table 3.7: Differently sized ME biosensors and their theoretical detection limits.

L [μm]	W [μm]	T [μm]	S_{m} [Hz/pg]	Δm_{min} [pg]	N_{min}	Material
4,000	800	15	7.34×10^{-4}	1.36×10^{6}	1,362,212	Metglas
2,000	400	15	5.87×10^{-3}	1.70×10^{5}	170,277	Metglas
1,000	200	15	4.70×10^{-2}	2.13×10^{4}	21,285	Metglas
500	100	15	3.76×10^{-1}	2.66×10^{3}	2,661	Metglas
500	250	4	7.65×10^{-1}	1.31×10^{3}	1,308	$Fe_{79}B_{21}$
500	167	4	1.15	8.73×10^{2}	874	$Fe_{79}B_{21}$
500	125	4	1.53	6.54×10^{2}	654	$Fe_{79}B_{21}$
500	100	4	1.91	5.23×10^{2}	523	$Fe_{79}B_{21}$
200	100	4	1.20×10^{1}	8.37×10^{1}	84	$Fe_{79}B_{21}$
200	67	4	1.78×10^{1}	5.61×10^{1}	57	$Fe_{79}B_{21}$
200	50	4	2.39×10^{1}	4.18×10^{1}	42	$Fe_{79}B_{21}$
200	40	4	2.99×10^{1}	3.35×10^{1}	34	$Fe_{79}B_{21}$
150	75	4	2.83×10^{1}	3.53×10^{1}	36	$Fe_{79}B_{21}$
150	50	4	4.25×10^{1}	2.35×10^{1}	24	$Fe_{79}B_{21}$
150	38	4	5.59×10^{1}	1.79×10^{1}	18	$Fe_{79}B_{21}$
150	30	4	7.08×10^{1}	1.41×10^{1}	15	$Fe_{79}B_{21}$
100	50	4	9.56×10^{1}	1.05×10^{1}	11	$Fe_{79}B_{21}$
100	33	4	1.45×10^{2}	6.90	7	$Fe_{79}B_{21}$
100	25	4	1.91×10^{2}	5.23	6	$Fe_{79}B_{21}$
100	20	4	2.39×10^{2}	4.18	5	$Fe_{79}B_{21}$
50	10	2	3.82×10^{3}	0.26	1	$Fe_{79}B_{21}$

3.5.2 Measurement of the resonant frequency of the ME biosensors

In order to determine the resonant frequency of the biosensors, they were individually placed into the center of a copper solenoid coil that is connected to a network analyzer (HP/Agilent 8751A from Agilent Technologies, Inc.), operated in the S_{11} reflection mode (Fig. 3.14). An incident AC signal was, then, applied across the coil to magnetically excite the longitudinal vibration of the biosensor, and the resultant reflected signal was compared with the incident signal over a proper range of frequencies. Finally, the resonant frequency of the biosensor was determined to be the frequency at which the largest change in normalized $|S_{11}|$ occurs, due to the magneto-mechanical resonance of the biosensor. To enhance the magnitude of the resonance peak, a proper bias magnetic field was also applied to the biosensor with a bar magnet. Figure 3.15 shows a response of a typical 500 μm $\times$ 100 μm $\times$ 4 μm ME biosensor in air.

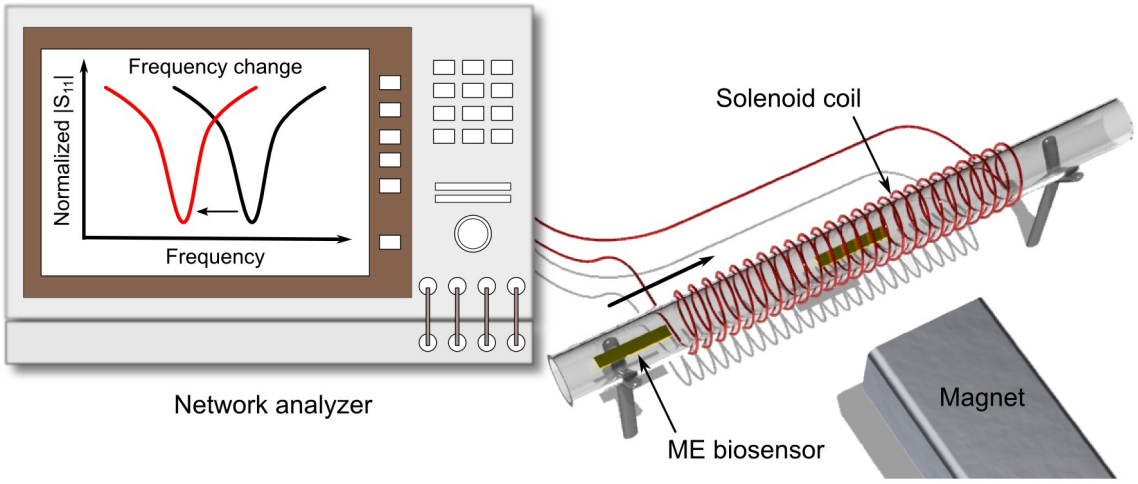

Figure 3.14: Measurement setup.

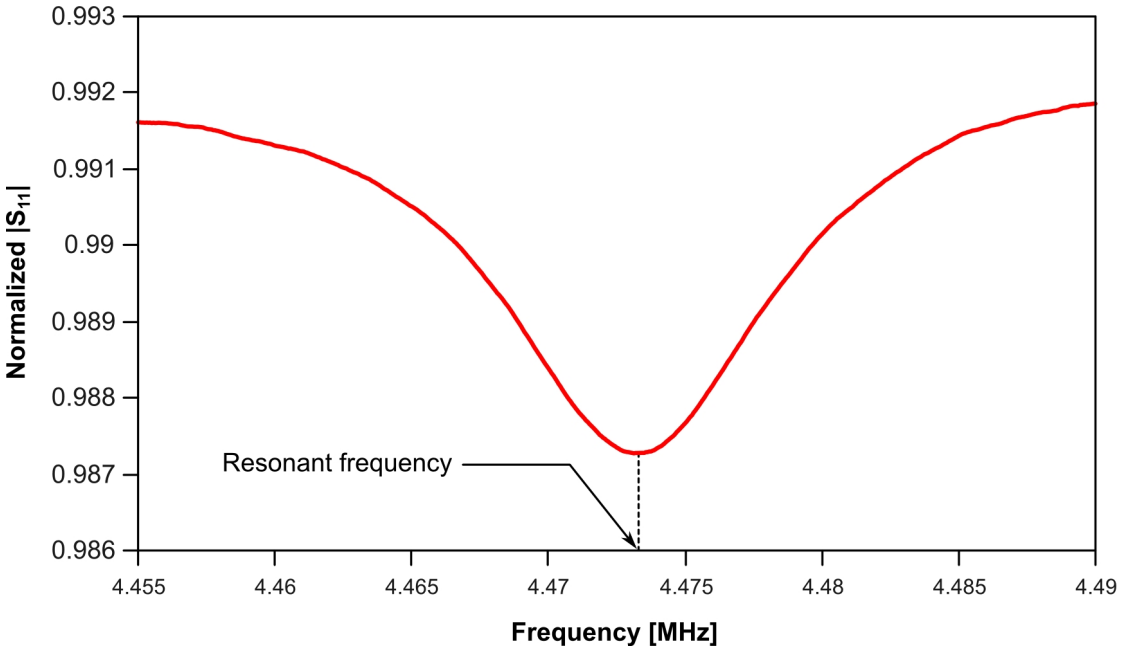

Figure 3.15: Response of a typical 500 μm $\times$ 100 μm $\times$ 4 μm ME biosensor in air.

Bibliography

[1] V. A. Petrenko, "Landscape phage as a molecular recognition interface for detection devices," *Microelectronics Journal*, vol. 39, no. 2, pp. 202 – 207, 2008.

[2] S. Goodchild, T. Love, N. Hopkins, and C. Mayers, "Engineering antibodies for biosensor technologies," vol. 58 of *Advances in Applied Microbiology*, pp. 185 – 226, Academic Press, 2005.

[3] J. Wan, M. L. Johnson, R. Guntupalli, V. A. Petrenko, and B. A. Chin, "Detection of *Bacillus anthracis* spores in liquid using phage-based magnetoelastic micro-resonators," *Sensors and Actuators B: Chemical*, vol. 127, no. 2, pp. 559 – 566, 2007.

[4] V. A. Petrenko and I. B. Sorokulova, "Detection of biological threats. a challenge for directed molecular evolution," *Journal of Microbiological Methods*, vol. 58, pp. 147 – 168, 2004.

[5] C. Mao, A. Liu, and B. Cao, "Virus-based chemical and biological sensing," *Angewandte Chemie International Edition*, vol. 48, pp. 6790 – 6810, 2009.

[6] J. Wan, H. Shu, S. Huang, B. Fiebor, I.-H. Chen, V. A. Petrenko, and B. A. Chin, "Phage-based magnetoelastic wireless biosensors for detecting *Bacillus anthracis* spores," *IEEE Sensors Journal*, vol. 7, pp. 470 – 477, 2007.

[7] M. L. Johnson, J. Wan, S. Huang, Z. Cheng, V. A. Petrenko, D.-J. Kim, I.-H. Chen, J. M. Barbaree, J. W. Hong, and B. A. Chin, "A wireless biosensor using microfabricated phage-interfaced magnetoelastic particles," *Sensors and Actuators A: Physical*, vol. 144, no. 1, pp. 38 – 47, 2008.

[8] R. S. Lakshmanan, R. Guntupalli, J. Hu, D.-J. Kim, V. A. Petrenko, J. M. Barbaree, and B. A. Chin, "Phage immobilized magnetoelastic sensor for the detection of *Salmonella typhimurium*," *Journal of Microbiological Methods*, vol. 71, no. 1, pp. 55 – 60, 2007.

[9] V. A. Petrenko, G. P. Smith, X. Gong, and T. Quinn, "A library of organic landscapes on filamentous phage," *Protein Engneering*, vol. 9, pp. 797 – 801, 1996.

[10] G. P. Smith and V. A. Petrenko, "Phage display," *Chemical Reviews*, vol. 97, pp. 391 – 410, 1997.

[11] V. Petrenko, G. Smith, M. Mazooji, and T. Quinn, "α-helically constrained phage display library," *Protein Engineering*, vol. 15, no. 11, pp. 943 – 950, 2002.

[12] D. Marvin, "Filamentous phage structure, infection and assembly," *Current Opinion in Structural Biology*, vol. 8, no. 2, pp. 150 – 158, 1998.

[13] H. Endemann and P. Model, "Lcoation of filamentous phage minor coat proteins in phage and in infected cells," *Journal of Molecular Biology*, vol. 250, no. 4, pp. 496 – 506, 1995.

[14] G. Kuzmicheva, P. Jayanna, I. Sorokulova, and V. Petrenko, "Diversity and censoring of landscape phage libraries," *Protein Engineering, Design and Selection*, vol. 22, pp. 9 – 18, 2009.

[15] I. B. Sorokulova, E. V. Olsen, I.-H. Chen, B. Fiebor, J. M. Barbaree, V. J. Vodyanoy, B. A. Chin, and V. A. Petrenko, "Landscape phage probes for *Salmonella typhimurium*," *Journal of Microbiological Methods*, vol. 63, no. 1, pp. 55 – 72, 2005.

[16] J. Brigati, D. D. Williams, I. B. Sorokulova, V. Nanduri, I.-H. Chen, C. L. Turnbough, and V. A. Petrenko, "Diagnostic probes for *Bacillus anthracis* spores selected from a landscape phage library," *Clinical Chemistry*, vol. 50, no. 10, pp. 1899 – 1906, 2004.

[17] E. du Trémolet de Lacheisserie, *Magnetostriction: Theory and Applications of Magnetoelasticity*. CRC Press, 1993.

[18] G. Vlasák, "Direct measurement of magnetostriction of rapidly quenched thin ribbons," *Journal of Magnetism and Magnetic Materials*, vol. 215-216, pp. 479 – 481, 2000.

[19] A. Hernando, M. Vazquez, and J. M. Barandiaran, "Metallic glasses and sensing applications," *Journal of Physics E: Scientific Instruments*, vol. 21, pp. 1129 – 1139, 1988.

[20] C. Modzelewski, H. T. Savage, L. T. Kabacoff, and A. E. Clark, "Magnetomechanical coupling and permeability in transversely annealed Metglas 2605 alloys," *IEEE Transactions on Magnetics*, vol. 17, pp. 2837 – 2839, 1981.

[21] R. C. O'Handley, *Modern Magnetic Materials: Principles and Applications*. New York: John Wiley & Sons Inc., 2000.

[22] http://www.metglas.com/products/page5_1_2_7.htm.

[23] C. A. Grimes, C. S. Mungle, K. Zeng, M. K. Jain, W. R. Dreschel, M. Paulose, and K. G. Ong, "Wireless magnetoelastic resonance sensors: A critical review," *Sensors*, vol. 2, pp. 294 – 313, 2002.

[24] S. Li, *Development of novel acoustic wave biosensor platforms based on magnetostriction and fabrication of magnetostrictive nanowires*. PhD thesis, Auburn University, 2007.

[25] L. Davis, R. Ray, C.-P. Chou, and R. O'Handley, "Mechanical and thermal properties of $Fe_{80}B_{20}$ glass," *Scripta Metallurgica*, vol. 10, pp. 541 – 546, 1976.

[26] C. Liang, S. Morshed, and B. C. Prorok, "Correction for longitudinal mode vibration in thin slender beams," *Applied Physics Letters*, vol. 90, p. 221912, 2007.

[27] H.-U. Künzi, "Mechanical properties of metallic glasses," in *Glassy Metal II*, vol. 53 of *Topics in Applied Physics*, pp. 169–216, Springer Berlin Heidelberg, 1983.

[28] C. China, "Magnetic properties of sputter deposited Fe based amorphous thin films for resonator application," Master's thesis, the University of Central Florida, 2006.

[29] M. A. Mitchell, A. E. Clark, H. T. Savage, and R. J. Abbundi, "ΔE effect and magnetomechanical coupling factor in $Fe_{80}B_{20}$ and $Fe_{78}Si_{10}B_{12}$ glassy ribbons," *IEEE Transactions on Magnetics*, vol. 14, pp. 1169 – 1171, 1978.

[30] S. Huang, J. Hu, J. Wan, M. Johnson, H. Shu, and B. Chin, "The effect of annealing and gold deposition on the performance of magnetoelastic biosensors," *Materials Science and Engineering: C*, vol. 28, no. 3, pp. 380 – 386, 2008.

[31] http://rs.acupcc.org/site_media/uploads/cap/699-cap_1.pdf.

[32] http://www.lesker.com/newweb/deposition_materials/depositionmaterials_sputtertargets_1.cfm?pgid=cr1.

[33] http://www.lesker.com/newweb/deposition_materials/depositionmaterials_sputtertargets_1.cfm?pgid=au1.

[34] http://www.lesker.com/newweb/deposition_materials/depositionmaterials_sputtertargets_1.cfm?pgid=fe1.

[35] http://www.lesker.com/newweb/deposition_materials/depositionmaterials_sputtertargets_1.cfm?pgid=bor1.

[36] C. A. Grimes, S. C. Roy, S. Rani, and Q. Cai, "Theory, instrumentation and applications of magnetoelastic resonance sensors: A review," *Sensors*, vol. 11, no. 3, pp. 2809 – 2844, 2011.

[37] http://hypertextbook.com/facts/2003/LouisSiu.shtml.

Chapter 4

Direct Detection of *S.* Typhimurium on Fresh Spinach Leaves

4.1 Introduction

Frequent outbreaks of bacterial food poisoning as well as associated illnesses are significant public health concerns. Hence, to secure the safety of our food supply, proper, routine testing of food products must be implemented throughout the supply chain. Conventionally, such testing has been conducted with phenotypic and/or genotypic assays, including culture- and PCR-based assays [1–10]. Although capable of providing confirmatory results with low detection limits, these methods are often complex, expensive, labour-intensive, and thus, not suitable for the on-site detection of pathogenic bacteria. In addition, rapidness of the testing is among the most important requirements particularly for dealing with a large volume of fresh produce and other essential food items that are consumed daily. To overcome the drawbacks of the conventional detection methods and facilitate on-site bacterial detection, much research has been recently focused on developing label-free biosensors [11–19]. However, even for these biosensors, sample preparation, including the collection, purification, and enrichment of a pathogen-containing sample, is generally required prior to the testing. Hence, there is a motivation for eliminating any pre-test sample preparation steps to simplify the procedure and further reduce the total time and cost of testing.

Attempts using phage-based ME biosensors have been recently made for the rapid, direct detection of *S.* Typhimurium on fresh produce (i.e., tomatoes and shell eggs [20–22]). These biosensors are composed of a freestanding, strip-shaped ME signal transducer coated with the E2 phage [23], which specifically binds with *S.* Typhimurium. These biosensors can be directly placed on produce surfaces due to

their wireless, freestanding nature and used to monitor the presence of the bacterium without pre-test sample preparation. In this investigation, the methodology was employed to test *Salmonella*-spiked spinach leaves.

Figures 4.1a to 4.1c show scanning electron micrographs of the surfaces of various produce: (a) a tomato, (b) a shell egg, and (c) a spinach leaf. As can be seen, surface topography varies from one produce to another. In addition, since spinach leaves are likely to possess complex surface topography as shown in Fig. 4.1d (a close-up view of a leaf surface), these surface features may affect the physical contact between the

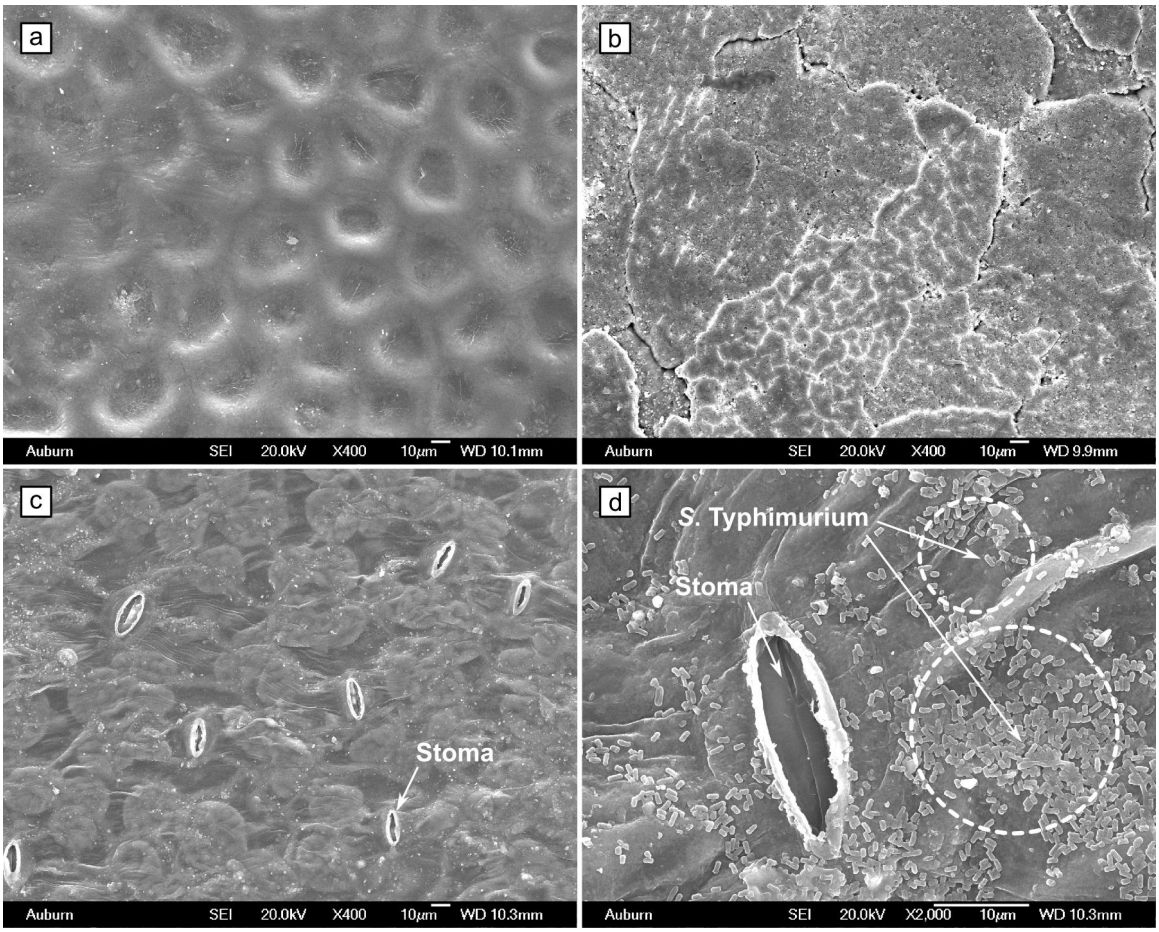

Figure 4.1: Scanning electron micrographs of various produce surfaces: (a) tomato, (b) eggshell, and (c) spinach leaf. A close-up view of a spinach leaf spiked with *S.* Typhimurium is shown in (d).

biosensors and *S.* Typhimurium cells. Hence, three different sizes of biosensors (2-mm, 500-μm, and 150-μm long) were fabricated and tested to investigate the effects of sensor size on the limit of detection (LOD). Furthermore, a formula describing the probability of detection as a function of the size and number of biosensors and the surface density of *S.* Typhimurium was derived. By using the formula, the required number of biosensors to obtain a desired LOD can be determined.

4.2 Material and methods

4.2.1 E2 phage and *S.* Typhimurium

Suspensions of the E2 phage (5×10^{11} virions/ml in a TBS buffer) and *S.* Typhimurium cells (ATCC 13311 at a concentration of 5×10^{8} cells/ml in sterile distilled water) were provided by Dr. James Barbaree's group at Auburn University. The concentrated *Salmonella* suspension was diluted with sterile distilled water as desired prior to use.

4.2.2 Confocal reflectance imaging of spinach leaf surfaces

Both adaxial and abaxial surfaces of fresh spinach leaves were imaged with a confocal scanning laser microscope (Nikon A1 from Nikon Corp.). The leaves were cut into 10 mm $\times$ 10 mm pieces without including any major leaf veins and mounted on a glass slide with double-sided tape. These samples were prepared right before the imaging and individually surface-scanned with a 488-nm line laser at 21 °C and 37% relative humidity. To minimize the degradation of the samples, a low laser power of 1.5% was used exclusively, and the imaging per sample was completed within 30 min. Reflectance from the sample surfaces was collected at magnifications of 40 and 400 with a bandpass filter of 482/35 nm. The collected digital data were saved as images with a pixel resolution of 1,024 $\times$ 1,024. The unit pixel length was 3.11 μm and 0.311 μm for images taken at 40 and 400 magnifications, respectively.

To reconstruct and characterize the topography of the sample surfaces, a series of plane images through the thickness of spinach leaf surfaces was captured. The separation between adjacent slices was 0.1 μm. Fifteen samples were prepared for both adaxial and abaxial surfaces and imaged at the above-mentioned magnifications. The ImageJ software with the SurfCharJ plugin [24] was, then, used to reconstruct the surface topography and extract surface height data associated with their location of pixels. Finally, surface profiles were regenerated and tilt-corrected by subtracting an overall increasing or decreasing linear trend along the sampling length.

4.2.3 Fabrication of ME sensor platforms with three different sizes

Freestanding, strip-shaped ME sensor platforms with three different sizes were fabricated of either Metglas 2826MB or $Fe_{79}B_{21}$, both of which are amorphous, ferromagnetic alloys with ME properties [25, 26]. Millimeter-long sensor platforms with two different sizes (2 mm $\times$ 0.4 mm $\times$ 15 μm and 0.5 mm $\times$ 0.1 mm $\times$ 15 μm) were manufactured by polishing and dicing a sheet of Metglas 2826MB. By contrast,

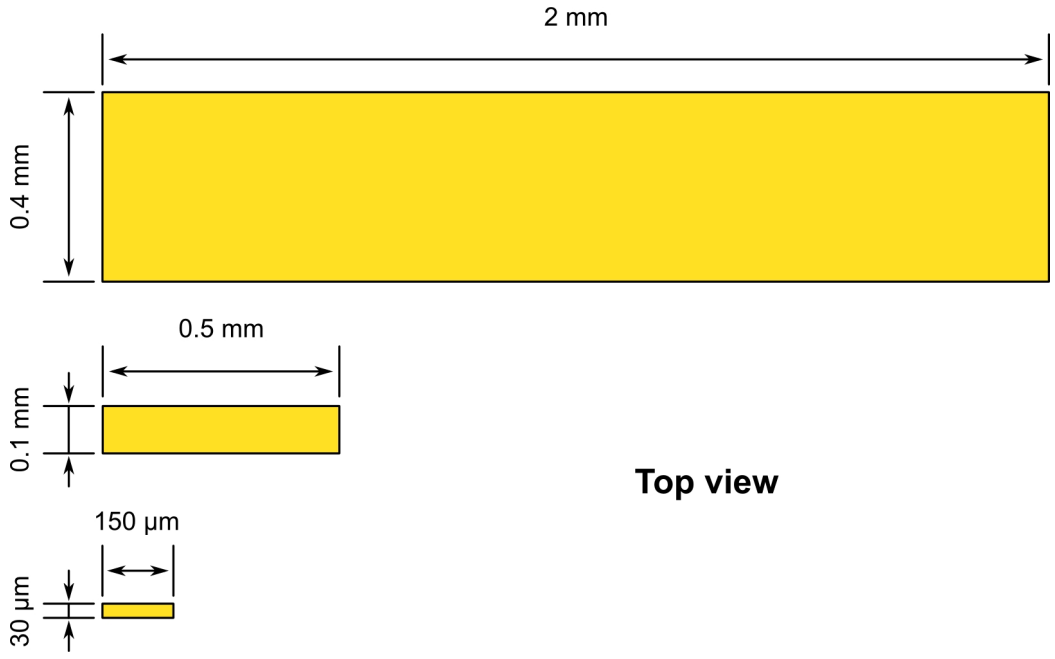

Figure 4.2: Differently sized sensor platforms used (top view).

micrometer-long sensor platforms with a size of 150 μm $\times$ 30 μm $\times$ 4 μm were fabricated of $Fe_{79}B_{21}$ using the co-sputtering-based method described in Chapter 3. Figure 4.2 illustrates the three differently sized sensor platforms used in this investigation.

4.2.4 Fabrication of phage-based ME biosensors

The fabrication of phage-based ME biosensors was completed by following the procedures described in Chapter 3. In addition to measurement sensors, control sensors, which are not immobilized with the E2 phage but only surface-blocked with BSA, were also prepared and used for background subtraction.

4.2.5 Determination of the concentration of BSA for surface blocking

In order to determine a reasonable concentration of BSA for surface blocking, measurement and control sensors (2-mm long) exposed to three different concentrations of BSA (0.01, 0.1, and 1 % w/v) were prepared and tested. These sensors were placed on a wet spinach leaf surface inoculated with *S.* Typhimurium (5×10^8 cells/ml, 40 μL) and, then, allowed for binding. Figure 4.3a shows responses for both measurement and control sensors. As can be seen, the resonant frequency changes for both types of sensors decreased with increased concentrations of BSA. Hence, in terms of surface blocking, a high BSA concentration is preferable. However, the response of control sensors must be minimized without unnecessarily reducing that of measurement sensors. Hence, it is important to find a BSA concentration at which the difference between the responses of measurement and control sensors is statistically maximized. For the three pairs of data in Fig. 4.3a, the confidence level of difference was calculated with a standard t-test [27, 28]. The best result (i.e., highest confidence level of difference) was obtained at a BSA concentration of 0.1 % w/v as shown in Fig. 4.3b. This concentration was, hence, used for surface blocking.

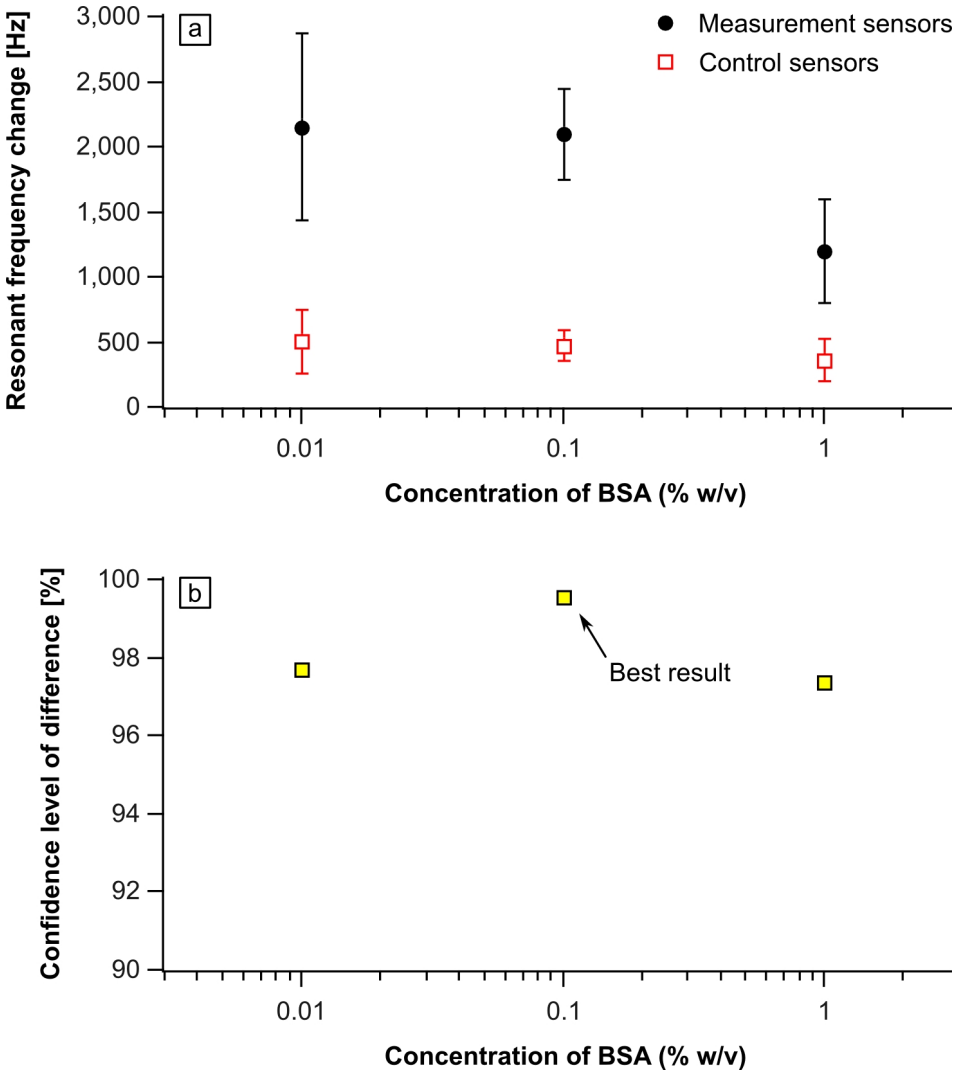

Figure 4.3: Effects of BSA concentration on (a) resonant frequency changes for measurement and control sensors (2-mm long) and on (b) the confidence level of difference.

4.2.6 Direct detection of *S.* Typhimurium on fresh spinach leaves

Pre-washed, bagged, fresh baby spinach leaves (Kroger brand) were purchased from a local grocery store and used as-received. They were, first, individually adhered to a clean, flat surface with double-sided tape. Forty-microliter drops of *S.* Typhimurium with various concentrations (i.e., ten-fold serial dilutions of 5×10^8 cells/ml) were, then, spot-inoculated on the leaf surface as illustrated in Fig. 4.4a. Any major leaf veins, which cause a sudden, large change in surface topography, were avoided. Yet, the total surface area of the major leaf veins was found to be small (7.3

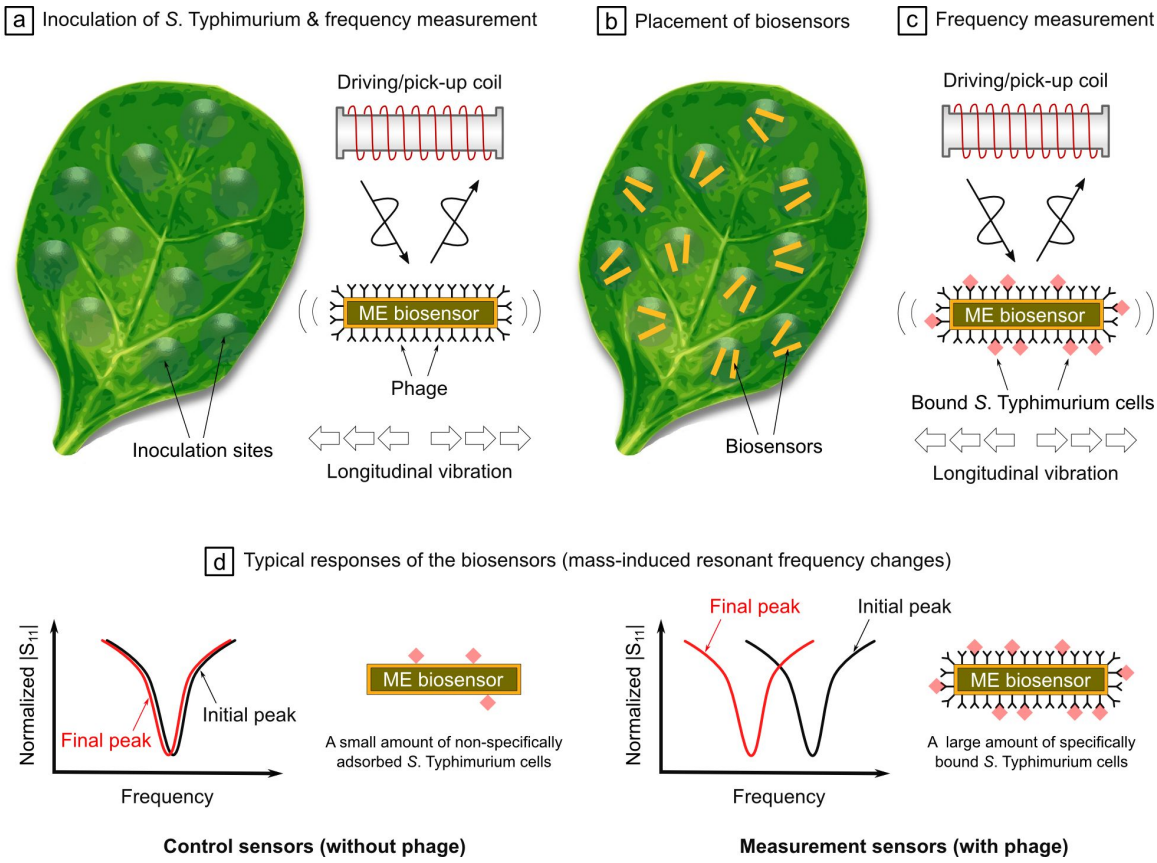

Figure 4.4: Schematic illustration of the test procedure: (a) spot-inoculation of *S.* Typhimurium on the leaf surface and measurement of the initial resonant frequency of biosensors, (b) placement of both measurement and control sensors on the *Salmonella*-inoculated sites (after drying the *Salmonella* drops and misting the leaf surface), (c) measurement of the final resonant frequency of the biosensors, and (d) typical responses of the biosensors.

$\pm$ 2.9 % of a leaf). The inoculated *Salmonella* drops were, then, allowed to dry in air for 90 to 120 min. Next, the leaf surface was uniformly misted by spraying sterile distilled water ($\sim$ 20 μl/cm^2), and both measurement and control sensors with a pre-determined resonant frequency were directly placed on the *Salmonella*-inoculated sites (Fig. 4.4b). After 25 min to allow for binding, the biosensors were collected with a magnet, and measurement of their final resonant frequency was completed within 20 min (Figs. 4.4c and 4.4d) (The method for resonant frequency measurement was described in Chapter 3). The total test time was, hence, roughly 45 min. In this investigation, the test was performed at 23 °C and 35% relative humidity. The three

differently sized biosensors (i.e., 2 mm-, 0.5 mm-, and 150 μm-long sensors) were used to test both adaxial and abaxial surfaces of the leaves. Ten measurement and control sensors each were used for each concentration of *S.* Typhimurium. In order to convert cells/ml into cells/cm^2 (i.e., surface density of *S.* Typhimurium), the area of the inoculation sites was measured and found to be 0.22 $\pm$ 0.02 cm^2 and 0.30 $\pm$ 0.03 cm^2 for the adaxial and abaxial surfaces, respectively.

4.3 Results

4.3.1 Observation of *Salmonella*-inoculated leaf surfaces

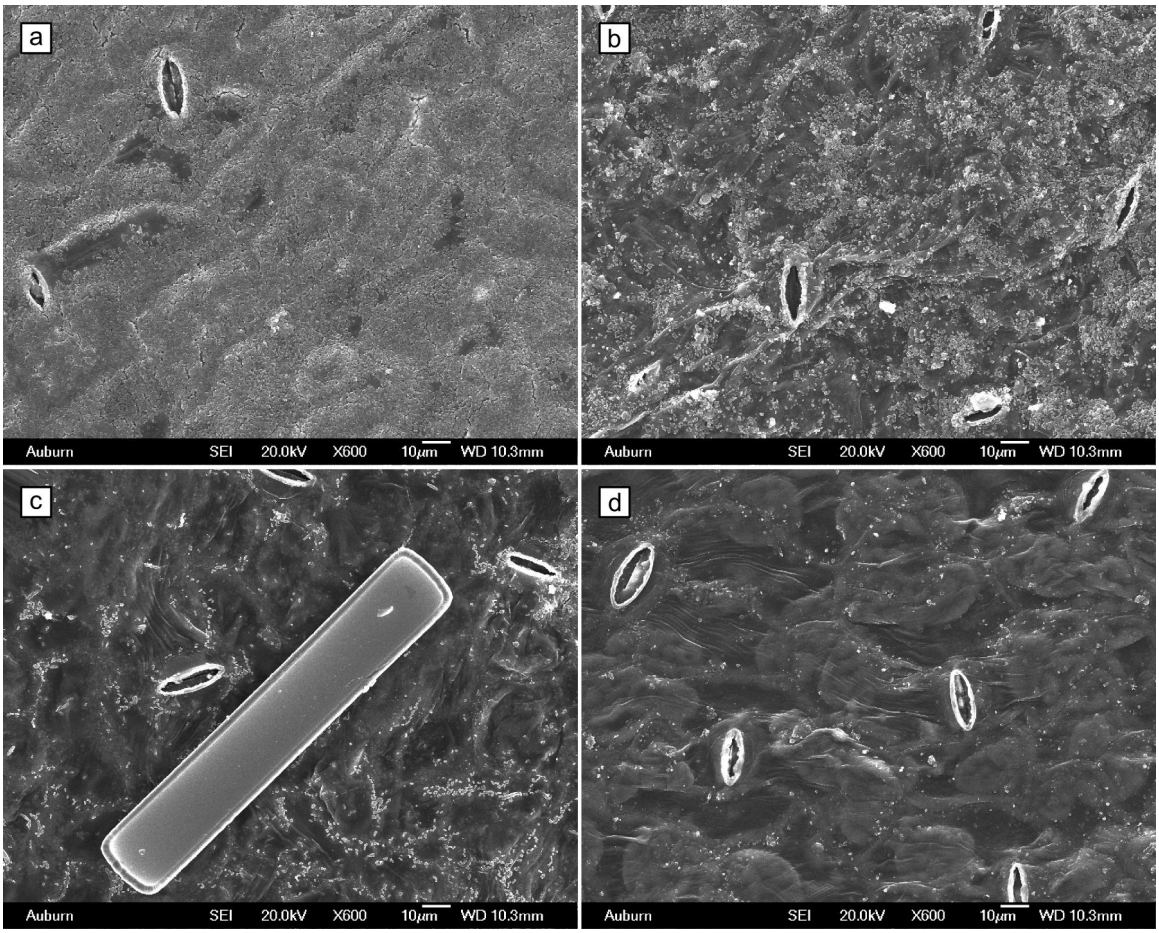

Figure 4.5: Scanning electron micrographs of a spinach leaf surface inoculated with a 40-μl drop of *S.* Typhimurium with various concentrations: (a) 5×10^8 cells/ml, (b) 5×10^7 cells/ml, (c) 5×10^6 cells/ml (with a 150 μm-long ME biosensor), and (d) 0 cells/ml (reference).

Figure 4.5 shows representative scanning electron micrographs of a spinach leaf surface inoculated with a 40-μl drop of *S.* Typhimurium with various concentrations. At a concentration of 5×10^8 cells/ml, the leaf surface was nearly completely covered by *S.* Typhimurium cells (Fig. 4.5a). The number of observable cells, then, decreased with decreased concentrations of inoculated cells as anticipated, and the distribution of cells became non-uniform for lower concentrations (Figs. 4.5b and 4.5c). This localization of cells may be attributed to localized availability of nutrients as well as leaf surface conditions (e.g., hydrophobicity and surface charges), which affect the motility and attachment of the cells [29, 30]. Furthermore, the leaf surface was found to possess complex topography (Fig. 4.5d), which plays a crucial role in physical contact between a biosensor and *S.* Typhimurium cells.

4.3.2 Resonant frequency measurement

Figure 4.6 shows a response of a typical 150 μm $\times$ 30 μm $\times$ 4 μm sensor, which was measured in air with the setup described in Chapter 3. It can be seen that the raw data set (dim gray curve in Fig. 4.6a) contains a high degree of noise even after a 10-time averaging operation. This noisy raw curve is common particularly for small sensors with small peak amplitudes, which requires additional smoothing of the data set. Hence, to further reduce the noise level, the Savitzky-Golay smoothing (25 points, second-order) was performed (black curve in Fig. 4.6a). In addition, Lorentzian fitting of the smoothed curve was finally performed to determine the resonant frequency of the sensor as shown in Fig. 4.6b. This method of data arrangement was also used for larger sensors. The mean resonant frequencies for the three differently sized biosensors are summarized in Table 4.1.

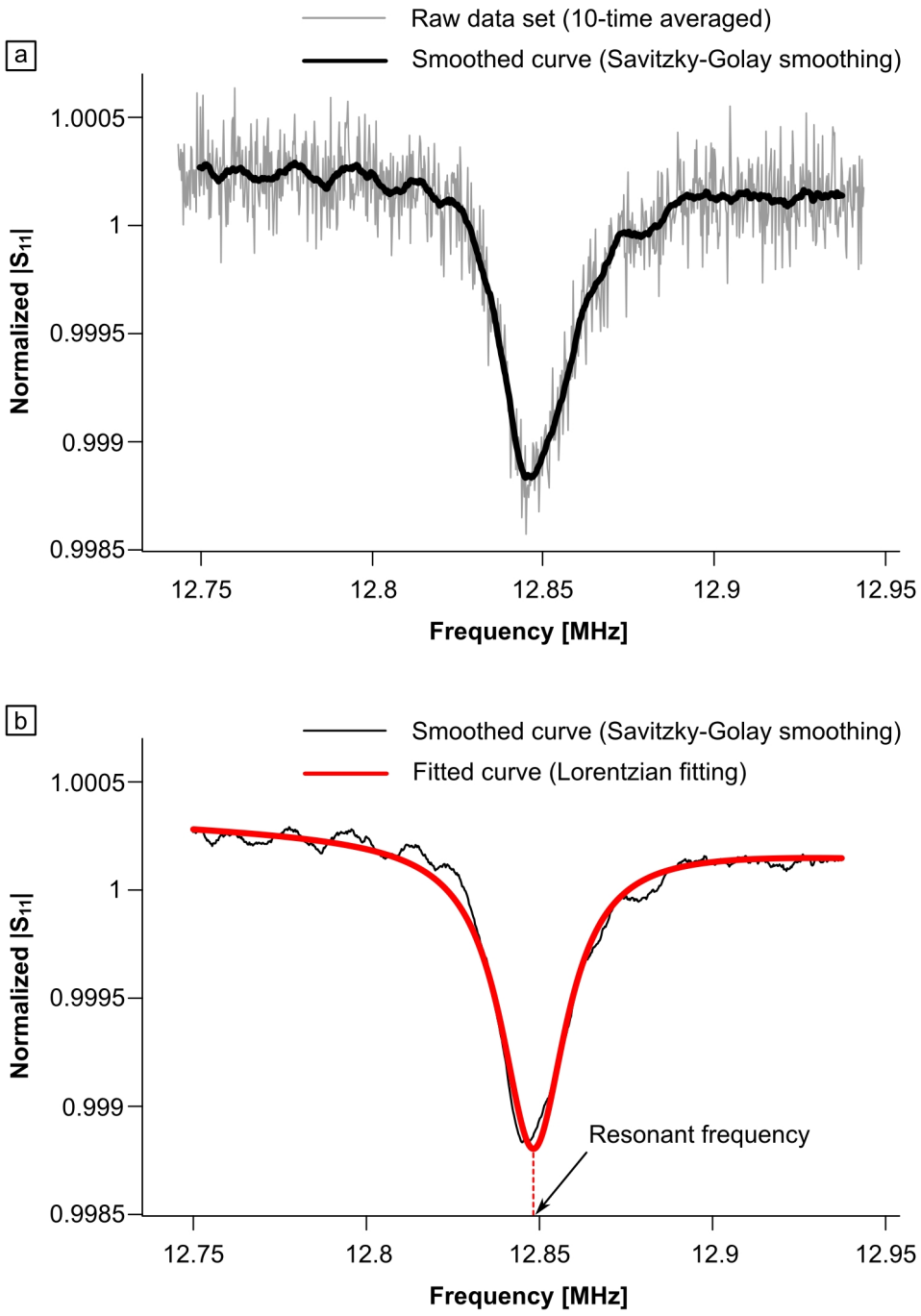

Figure 4.6: Response of a typical 150 μm $\times$ 30 μm $\times$ 4 μm sensor in air: (a) raw data set (10-time averaged) and its smoothed curve and (b) Lorentizan fitting of the smoothed curve.

Table 4.1: Mean resonant frequencies for the differently sized biosensors.

Sensor size	**Mean resonant frequency**
2 mm × 0.4 mm × 15 μm	1.12 ± 0.04 MHz
0.5 mm × 0.1 mm × 15 μm	4.41 ± 0.04 MHz
150 μm × 30 μm × 4 μm	13.06 ± 0.12 MHz

To determine a change in the resonant frequency of a sensor, both the initial and final resonant frequencies (f_{initial} and f_{final}) need to be measured. An example is shown in Fig. 4.7, where the resonant peaks for a 150-μm long sensor before and after placing on a leaf surface inoculated with *S.* Typhimurium (5×10^8 cells/ml) are shown. It can be seen that the final peak appears at a lower frequency due to the attachment of *S.* Typhimurium cells.

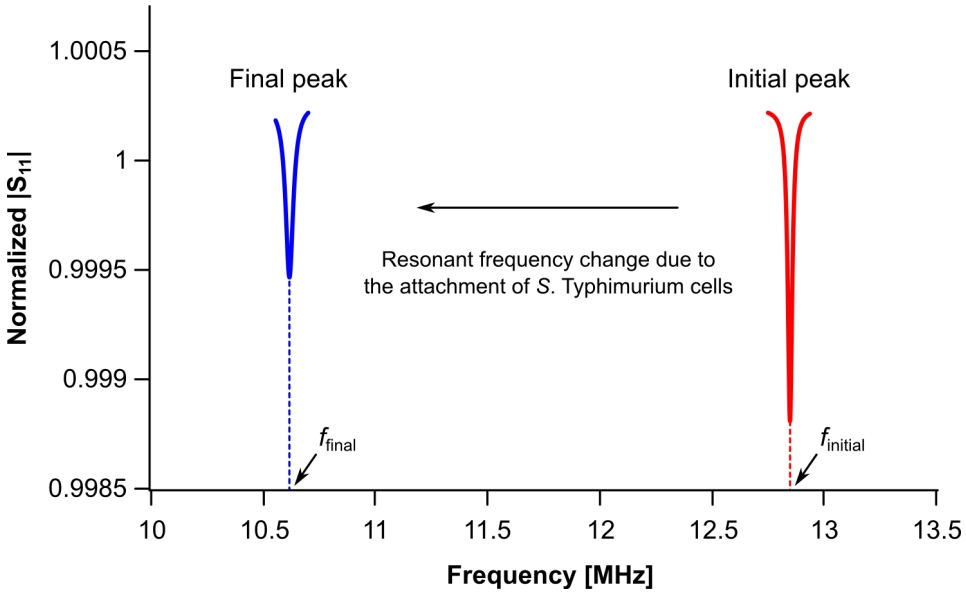

Figure 4.7: Resonant peaks for a 150-μm long sensor before and after placing on a leaf surface inoculated with *S.* Typhimurium at a concentration of 5×10^8 cells/ml.

4.3.3 Dose-response of the ME biosensors

Dose-response relationships for the differently sized biosensors are shown in Fig. 4.8. The plots on the left and right are the results for the adaxial and abaxial surfaces

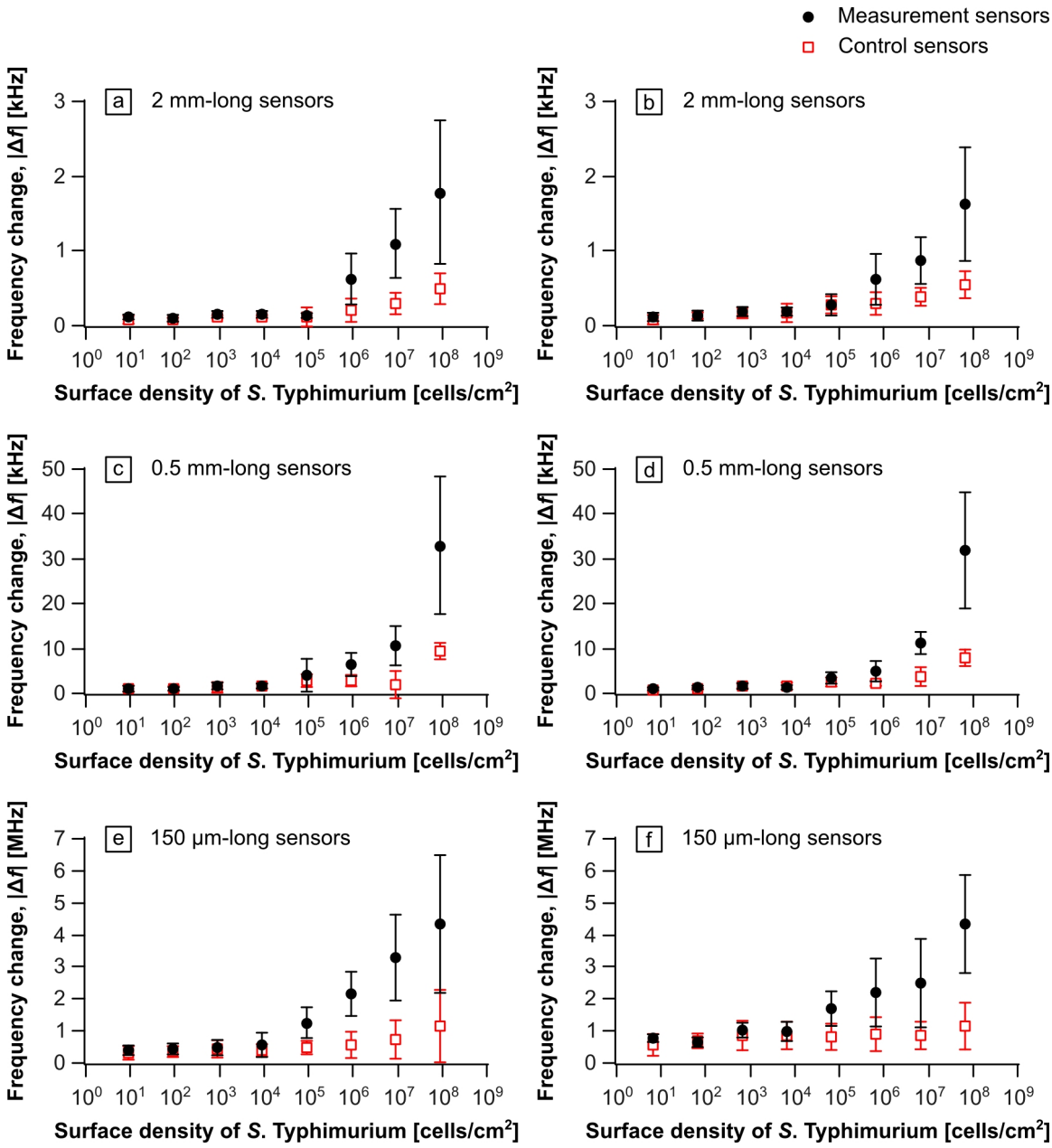

Figure 4.8: Dose-response plots for the differently sized biosensors (2 mm-, 0.5 mm- and, 150 μm-long sensors). The plots on the left and right are the results for the adaxial and abaxial surfaces, respectively.

of spinach leaves, respectively. Resonant frequency changes of measurement sensors (circles) were found to be largely dependent on the surface density of *S.* Typhimurium. By contrast, control sensors (squares) showed much smaller responses, indicating that selective binding of *S.* Typhimurium on the measurement sensors occurred. In

addition, the standard error was found to be large at high surface densities of *S.* Typhimurium, which may be attributed to (1) the complex topography of leaf surfaces and (2) the random locations of the sensors, resulting in non-uniform, inconsistent physical contact between the sensors and *S.* Typhimurium cells.

4.3.4 Determination of the LOD

The LODs for the above dose-response plots were determined as follows:

1. The responses of the control sensors were subtracted from those of the measurement sensors (i.e., background subtraction).

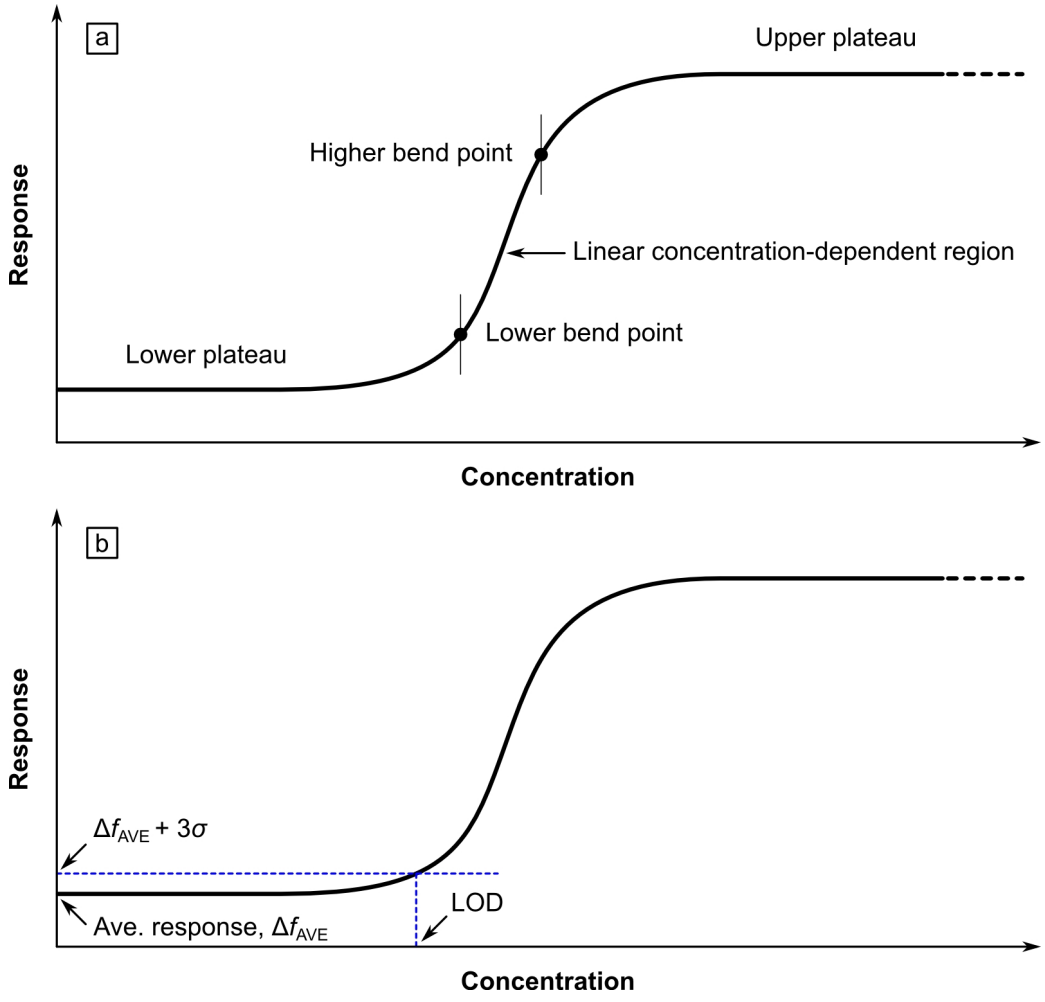

Figure 4.9: (a) Sigmoidal curve and (b) the determination of the LOD.

2. The resultant data were curve-fitted with sigmoidal functions, which are commonly used for the description of the response patterns of bioassays [31]. On a sigmoidal curve, there are usually two concentration-independent regions (i.e., lower and upper plateaus) and one linear concentration-dependent region defined with two bend points as shown in Fig. 4.9a.

3. Finally, the LOD was determined as the concentration at which the fitted response deviates from the average response in the lower plateau region, Δf_{AVE}, by a multiple of the standard error, σ, in the region [32]. The value of the multiple is dependent on a required statistical significance level. In this work, a multiple of three was used (i.e., 3σ) as shown in Fig. 4.9b. Note that the lower plateau region was determined through a linear regression analysis with an R^2 value of greater than 0.95.

Figure 4.10 shows background-subtracted data for the dose-response plots shown in Fig. 4.8. These data were fitted with sigmoidal functions (red solid curves), which can be defined as [31]

$$Y = \frac{a - b}{1 + (X/c)^d} + b, \tag{4.1}$$

where Y, X, a, b, c, and d represent the response, concentration (i.e., surface density of *S.* Typhimurium), lower asymptote, upper asymptote, inflection point, and slope factor, respectively. The R^2 values were found to be all close to the unity, indicating that the curve fitting was well performed. To determine the LOD, the $\Delta f_{\mathrm{AVE}} + 3\sigma$ values were extrapolated to the fitted curves as shown in Fig. 4.10 (blue dashed lines). Table 4.2 summarizes the LODs of the differently sized biosensors for both adaxial and abaxial surfaces of spinach leaves.

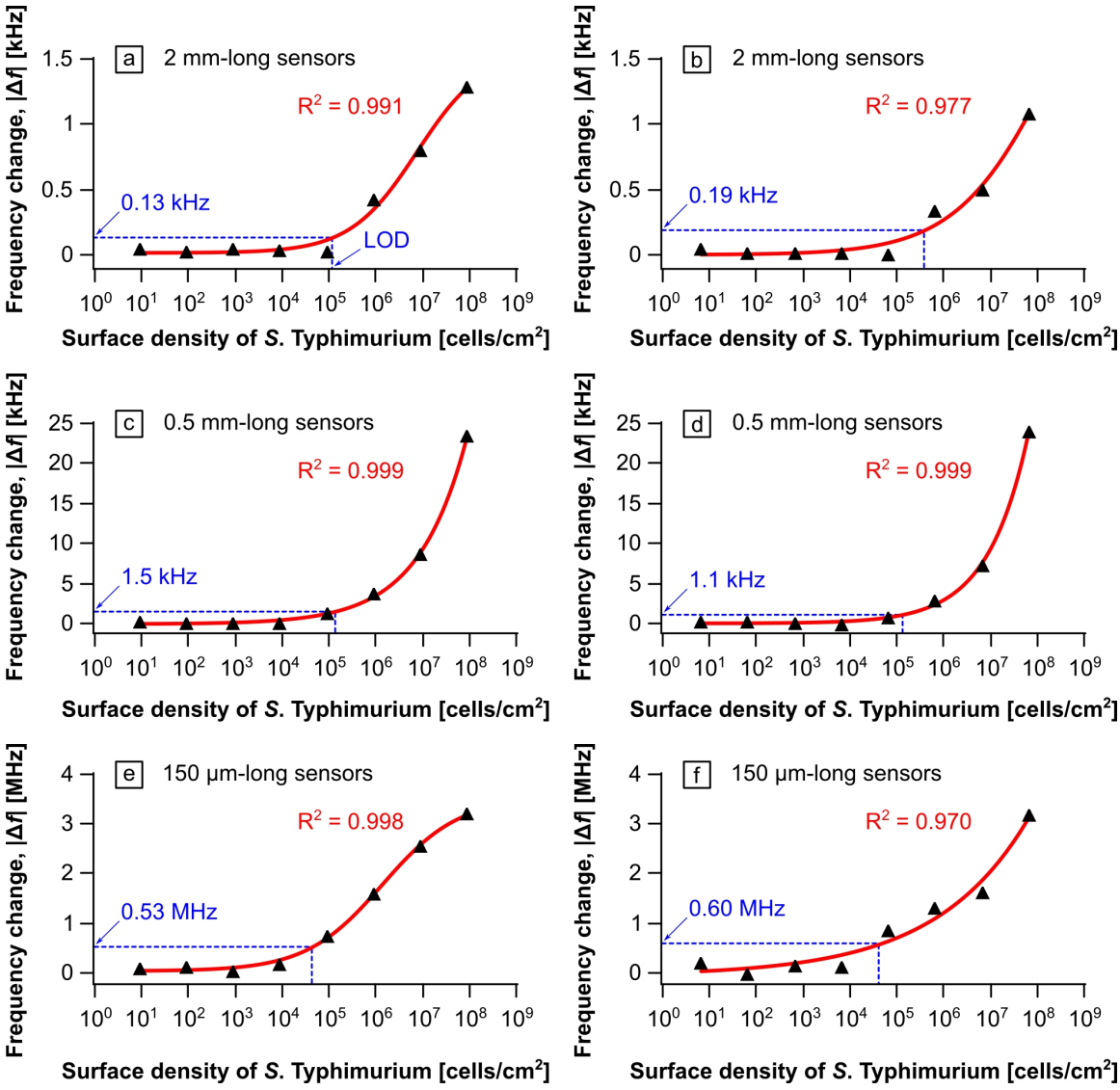

Figure 4.10: Background-subtracted data for the dose-response plots in Fig. 4.8. These data were fitted with sigmoidal functions (red solid curves). The R^2 values were all close to one. The values of $\Delta f_{\mathrm{AVE}} + 3\sigma$ are shown in blue text.

As can be seen in Table 4.2, the LOD was found to be on the order of 10^4 to 10^5 cells/cm^2. The best results were obtained with the 150-μm long sensors although, among the differently sized biosensors, these micron-scale biosensors possess the smallest surface area (i.e., the product of the length and width of the biosensor, LW) to cover a *Salmonella*-inoculated leaf surface. In addition, the LODs for the larger biosensors were found to be higher by half an order to one order of magnitude,

and there were not large differences among them. One possible explanation for these results is that there is a trade-off between the surface area and mass sensitivity of a biosensor as can be seen in Eq. 3.6. In other words, while the surface area of a biosensor increases proportionally to LW, the mass sensitivity decreases proportionally to L^2WT. Hence, the use of a large biosensor, which covers a large area of a leaf surface, may not always lead to sensitive detection of *S.* Typhimurium. Rather, a properly small biosensor may be able to show a measurable response even though a small number of *S.* Typhimurium cells may be bound on this biosensor. In addition, from the preceding microscopic observation, the topography of leaf surfaces and distribution of *S.* Typhimurium cells are both anticipated to affect the LOD.

Table 4.2: LODs of the differently sized biosensors for the adaxial and abaxial surfaces of spinach leaves.

Sensor size	**LOD [cells/cm^2]**	
	Adaxial surface	**Abaxial surface**
2 mm × 0.4 mm × 15 μm	1.28×10^5	4.12×10^5
0.5 mm × 0.1 mm × 15 μm	1.42×10^5	1.37×10^5
150 μm × 30 μm × 4 μm	4.77×10^4	5.22×10^4

4.4 Discussion

4.4.1 Topography of leaf surfaces and its effects on the LOD

In order to characterize the topography of the leaf surfaces, mean roughness (R_a), mean flatness (F_a), and associated major periodicities (T_R and T_F) were quantified. Mean roughness, R_a, is a commonly used roughness parameter and can be defined as the arithmetic average of the absolute values of height deviations measured from the mean plane of a surface [33, 34]. In addition, the same definition can be given to mean flatness, F_a, which was, however, measured with a longer sampling length (i.e., The sampling lengths for R_a and F_a measurements were 318.5 μm and 3185

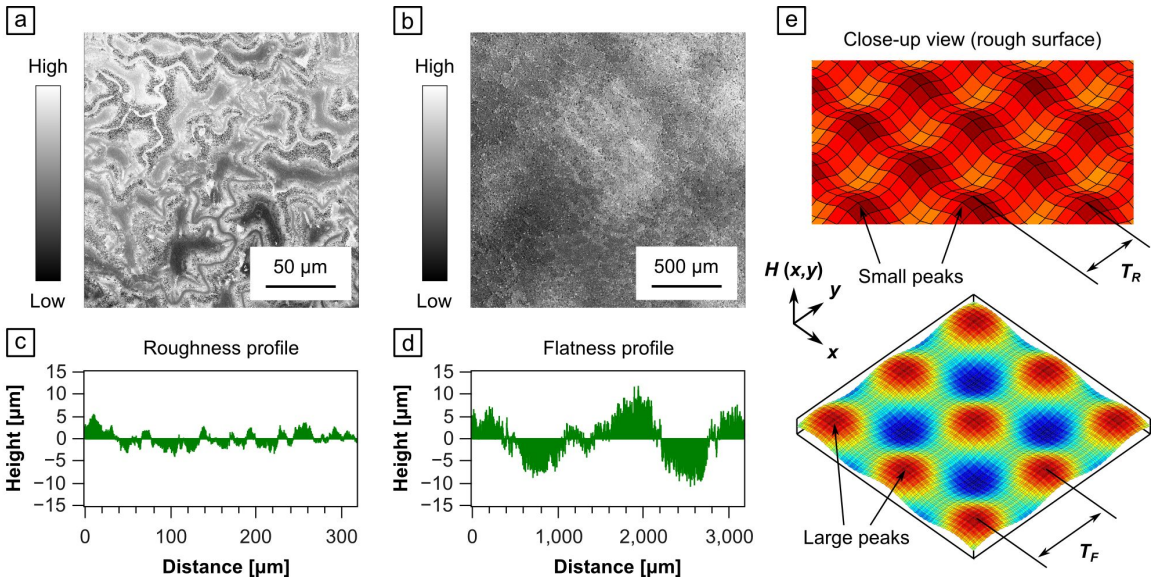

Figure 4.11: Typical height maps (a & b) and associated averaged profiles (c & d) of a leaf surface obtained along different sampling lengths. A three-dimensional representation of a leaf surface expressed by Eq. 4.2 is shown in (e).

μm, respectively.). Figures 4.11a to 4.11d show typical height maps and associated averaged profiles of a leaf surface obtained along different sampling lengths. From the profile with a short sampling length (Fig. 4.11c), it can be seen that the leaf surface possesses a certain degree of roughness, R_a. By contrast, the profile with a long sampling length (Fig. 4.11d) provides insight into the flatness of the surface, F_a. Furthermore, for both surface profiles, the major periodicities, T_R and T_F, can be determined by performing a Fourier transform of the profile ordinates and taking the reciprocal of the main frequency mode. The experimentally determined values for these surface geometric parameters are summarized in Table 4.3. The values are all non-zeros, indicating that leaf surfaces are rough, non-flat surfaces with topographic periodicities. Hence, with all the geometric parameters, the height at an arbitrary location of a leaf surface, H $(x,\ y)$, can be expressed by the superposition of sine

Table 4.3: Surface geometric parameters for the adaxial and abaxial surfaces of spinach leaves. The values are the averages of 15 samples.

Parameter	**Adaxial surface**	**Abaxial surface**
R_a (μm)	1.2 ± 0.2	1.6 ± 0.3
F_a (μm)	8.7 ± 3.7	7.0 ± 1.9
T_R (μm)	56.3 ± 18.4	67.4 ± 27.0
T_F (μm)	1376.7 ± 309.0	874.7 ± 196.1

waves (i.e., when $F_a << T_F$) as

$$\begin{aligned} H(x,y) &= \frac{1}{2}[R_a \sin(\frac{2\pi}{T_R}x) + F_a \sin(\frac{2\pi}{T_F}x) \\ &\quad + R_a \sin(\frac{2\pi}{T_R}y) + F_a \sin(\frac{2\pi}{T_F}y)], \end{aligned} \tag{4.2}$$

where x and y are the lateral coordinates of the leaf surface, respectively. The first and third terms on the right-hand side of Eq. 4.2 describe roughness profiles, whereas the second and forth terms represent flatness profiles along the lateral dimensions of the leaf surface, respectively. A three-dimensional representation of this mathematically expressed surface is shown in Fig. 4.11e, where a periodic arrangement of peaks and valleys can be seen. The periodicities, T_R and T_F, represent the lateral distances between two adjacent peaks of different scale, respectively (i.e., roughness-related small peaks and flatness-related large peaks).

In order to investigate effects of a leaf's surface topography on the physical contact between a biosensor and *S.* Typhimurium cells, the surface area of the biosensor, LW, was compared with two characteristic areas of the leaf surface, A_R and A_F, which are defined by

$$A_R = T_R \times T_R, \tag{4.3}$$

$$A_F = T_F \times T_F, \tag{4.4}$$

$$A_R << A_F \quad (\because T_R << T_F). \tag{4.5}$$

In other words, A_R and A_F are the areas surrounded by four adjacent small and large peaks, respectively. When $LW >> A_F$, the biosensor is likely to stay on large peaks, which greatly reduces the degree of physical contact with the leaf surface (and thus, with *S.* Typhimurium cells). By contrast, when $A_F >> LW >> A_R$, the biosensor can fit among large peaks (but stays on small peaks), which may improve the physical contact. Furthermore, when $LW << A_R$, the effects of the leaf's surface topography can be neglected, and thus, the degree of physical contact can be maximized. In this case, all that matters is the distribution of *S.* Typhimurium cells on the leaf surface. Hence, the characteristic area, A_R, and its associated length, T_R, are important parameters that allow one to choose a properly small biosensor free from the surface topographic effects. As shown in Table 4.3, the values of T_R for the adaxial and abaxial surfaces of spinach leaves were 56.3 $\pm$ 18.4 μm and 67.4 $\pm$ 27.0 μm, respectively. Among the differently sized biosensors used in this investigation, the 150-μm long sensors possess the closest lateral dimensions to these characteristic lengths, indicating that the topographic effects for these micron-scale biosensors were the smallest. By contrast, the millimeter-scale biosensors (i.e., 2-mm and 0.5-mm long sensors) possess lateral dimensions much larger than T_R and, rather, close to T_F. Hence, it is understandable that much larger topographic effects were posed to these larger biosensors. Furthermore, for real leaf surfaces, there exists microscopic irregularity in topography as can be seen in Figs. 4.11a to 4.11d, which is likely to cause reduced degrees of physical contact particularly for large biosensors. Hence, with the aforementioned merit of high mass sensitivity, the use of sufficiently small biosensors (i.e., $LW << A_R$) in proper quantity (number of sensors) may be the key to improving the LOD.

4.4.2 Effects of the number of biosensors on the LOD

Now that a properly small size of biosensor can be determined from the previous section, a remaining key question is how many biosensors of such a size are actually needed to detect *S.* Typhimurium cells on a leaf surface? To answer this question, a simple model that describes the probability of detection will be presented. The probability of detection is dependent on various factors, including the size, number, and mass sensitivity of the biosensor, the surface density and distribution of *S.* Typhimurium cells, and the topography of the leaf surface. Although spinach leaf surfaces were found to be rough, non-flat surfaces, they can be treated as smooth, flat surfaces if the size of the biosensor is sufficiently small (i.e., $LW << A_R$). In this case, the probability of detection, $P(\mathrm{D})$, can be simplified to

$$P(\mathrm{D}) = P(\mathrm{ms})P(\mathrm{pc}), \tag{4.6}$$

where $P(\mathrm{ms})$ is a probability function related to the mass sensitivity of the biosensor, and $P(\mathrm{pc})$ is the probability of physical contact between the biosensor and *S.* Typhimurium cells. $P(\mathrm{ms})$ is given as

$$P(\mathrm{ms}) = \begin{cases} 1 & (N \geq N_{\min}) \\ 0 & (N < N_{\min}) \end{cases}, \tag{4.7}$$

where N is the number of *S.* Typhimurium cells bound on a single biosensor, and $N_{\min}$ is the minimum detectable number of *S.* Typhimurium cells for this biosensor. $N_{\min}$ can be computed using Eq. 3.6 with the minimum detectable response, $\Delta f_{\mathrm{AVE}} + 3\sigma$, defined in Fig. 4.9 and the mass of a single *S.* Typhimurium cell, m_{ST}. By

rearranging Eq. 3.6 and replacing Δf with $\Delta f_{\mathrm{AVE}} + 3\sigma$, N_{min} can be defined as

$$N_{\mathrm{min}} = \frac{\Delta m}{m_{\mathrm{ST}}} \approx \frac{4(|\Delta f_{\mathrm{AVE}} + 3\sigma|)L^2WT}{m_{\mathrm{ST}}}\sqrt{\frac{\rho^3(1-\nu)}{E}}. \tag{4.8}$$

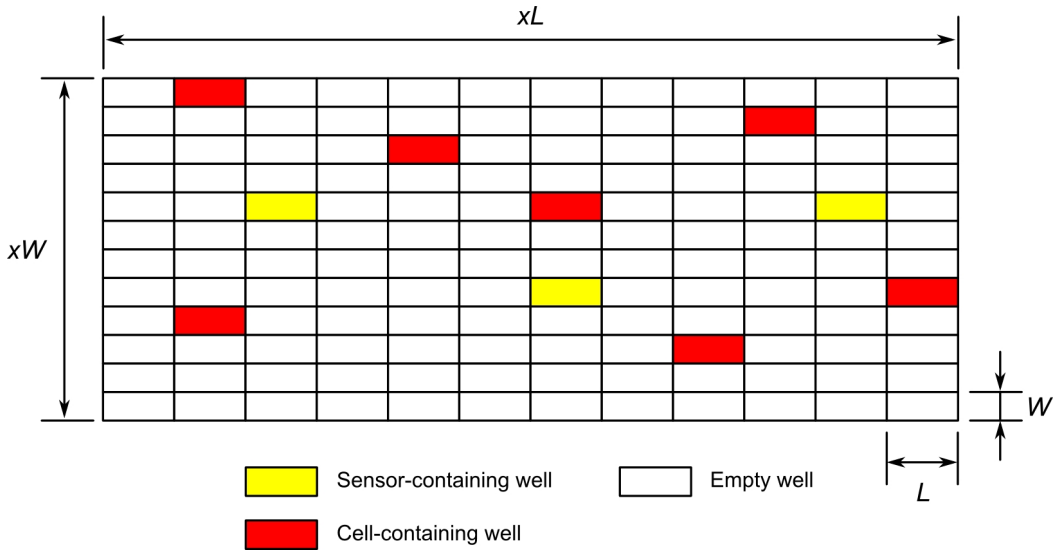

Figure 4.12: Finite well model of a *Salmonella*-inoculated leaf surface. The total surface area is x^2LW. There are three types of wells: sensor-containing wells, cell-containing wells, and empty wells.

Now, let's consider a simple finite well model of a *Salmonella*-inoculated leaf surface with a total surface area of x^2LW as shown in Fig. 4.12. Let m, n, and x^2 be the number of sensor-containing wells, the number of cell-containing wells, and the total number of wells, respectively. For this model, the following assumptions were made:

1. The area of each well is equal to that of a sensor (i.e., LW). Hence, one well can contain one sensor at most. In other words, the number of sensor-containing wells, m, is equal to the number of sensors placed on the surface.

2. The orientation of a sensor and a well matches to each other.

3. There is no overlapping among sensors.

4. Cell-containing wells are randomly located.

5. In each cell-containing well, there are N cells, which are uniformly distributed. When a sensor is placed, all the N cells are attached to the sensor uniformly.

In order to calculate $P(\mathrm{pc})$, first, the multiplication law of probability was used to derive the complement probability, $\overline{P(\mathrm{pc})}$. When $n = 1$, there is only one cell-containing well among x^2 wells as can be seen in Fig. 4.13. Hence, the probability that the first sensor is not placed in the cell-containing well, $\overline{P(\mathrm{pc}_1)}$, is

$$\overline{P(\mathrm{pc}_1)} = \frac{{}_{x^2-1}C_1}{{}_{x^2}C_1} = \frac{x^2-1}{x^2}. \tag{4.9}$$

Likewise, the probability that the second sensor is also not placed in the cell-containing well, $\overline{P(\mathrm{pc}_2)}$, is

$$\overline{P(\mathrm{pc}_2)} = \frac{{}_{x^2-2}C_1}{{}_{x^2-1}C_1} = \frac{x^2-2}{x^2-1}, \tag{4.10}$$

and the probability that the ith sensor is also not placed in the cell-containing well, $\overline{P(\mathrm{pc}_i)}$, is

$$\overline{P(\mathrm{pc}_i)} = \frac{{}_{x^2-i}C_1}{{}_{x^2-i+1}C_1} = \frac{x^2-i}{x^2-i+1}. \tag{4.11}$$

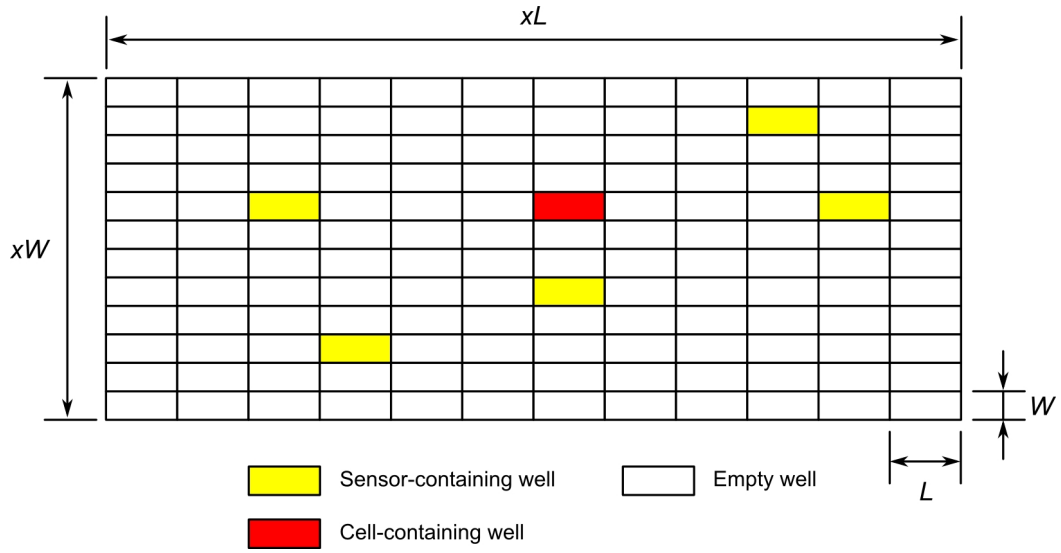

Figure 4.13: Finite well model with $n = 1$ (i.e., one cell-containing well).

Finally, the probability that none of m sensors is placed in the cell-containing well, $\overline{P(\mathrm{pc})_{n=1}}$, can be given as

$$\begin{aligned}\overline{P(\mathrm{pc})_{n=1}} &= \overline{P(\mathrm{pc}_1)} \times \overline{P(\mathrm{pc}_2)} \times \cdots \times \overline{P(\mathrm{pc}_m)} \\ &= \prod_i^m (\frac{x^2 - i}{x^2 - i + 1}).\end{aligned} \tag{4.12}$$

Similarly, when $n = 2$ and $n = 3$, the compliment probabilities can be calculated respectively as

$$\overline{P(\mathrm{pc})_{n=2}} = \prod_i^m (\frac{x^2 - i - 1}{x^2 - i + 1}) \tag{4.13}$$

and

$$\overline{P(\mathrm{pc})_{n=3}} = \prod_i^m (\frac{x^2 - i - 2}{x^2 - i + 1}). \tag{4.14}$$

By analogy, when there are n cell-containing wells among x^2 wells, the probability that none of m sensors is placed in any of the n cell-containing wells, $\overline{P(\mathrm{pc})}$, can be expressed as

$$\overline{P(\mathrm{pc})} = \prod_i^m (\frac{x^2 - i - n + 1}{x^2 - i + 1}). \tag{4.15}$$

Finally, $P(\mathrm{pc})$ can be obtained by subtracting $\overline{P(\mathrm{pc})}$ from the unity as

$$\begin{aligned}P(\mathrm{pc}) &= 1 - \overline{P(\mathrm{pc})} \\ &= 1 - \prod_i^m (\frac{x^2 - i - n + 1}{x^2 - i + 1}).\end{aligned} \tag{4.16}$$

By substituting Eq. 4.16 into Eq. 4.6, the probability of detection, $P(\mathrm{D})$, is, then, given as

$$P(\mathrm{D}) = P(\mathrm{ms})[1 - \prod_i^m (\frac{x^2 - i - n + 1}{x^2 - i + 1})], \tag{4.17}$$

which is a function of $P(\mathrm{ms})$, m, n, and x^2. Figure 4.14, for example, shows the probability of detection, $P(\mathrm{D})$, with respect to the number of biosensors, m, and the

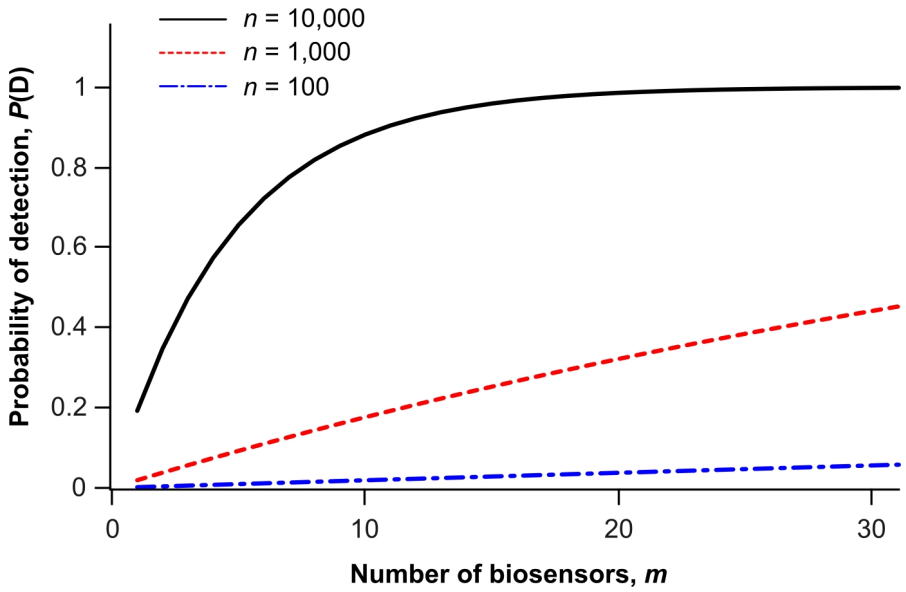

Figure 4.14: Probability of detection with respect to the number of biosensors, m, and the number of cell-containing wells, n. Biosensors with lateral dimensions of 50 μm $\times$ 10 μm were placed on a leaf surface of 0.26 cm^2.

number of cell-containing wells, n, for 50 μm $\times$ 10 μm biosensors (i.e., $LW << A_R$) placed on a leaf surface of 0.26 cm^2, provided that $N \geq N_{\min}$ (i.e., $P(\text{ms}) = 1$). Note that the value of x^2 was calculated by 0.26 cm^2/(LW). As can be seen, P(D) increases with increased numbers of m and n.

Now, theoretical LODs with desired threshold values of P(D) can be determined for a sufficiently small biosensor (i.e., $LW << A_R$). From the assumption #5, the total number of *S.* Typhimurium cells, N_{total}, on the *Salmonella*-inoculated leaf surface can be calculated by

$$N_{\text{total}} = nN. \tag{4.18}$$

Hence, when $N = N_{\min}$, the LOD can be calculated in terms of the surface density of *S.* Typhimurium by

$$\text{LOD} = \frac{N_{\text{total}}}{\text{total surface area}} = \frac{N_{\text{total}}}{x^2 LW} = \frac{nN}{x^2 LW} = \frac{nN_{\min}}{x^2 LW}. \tag{4.19}$$

When $N_{\min} = 1$, Eq. 4.19 can be further simplified to

$$\text{LOD} = \frac{n}{x^2 LW}, \tag{4.20}$$

which is the case for biosensors as small as 50 μm $\times$ 10 μm $\times$ 2 μm, provided that $\Delta f_{\text{AVE}}+3\sigma$ of 1,000 Hz can be resolved (See Table 3.7.). In addition, from Eq. 4.17, the number of cell-containing wells, n, becomes merely a function of the number of biosensors, m, when the values of $P(\text{D})$ and x^2 are given. Hence, for a certain size of biosensor (i.e., for known values of L and W with $LW << A_R$), the LOD can be finally expressed as a function of m by

$$\text{LOD} = \frac{n}{x^2 LW} = \frac{n}{\text{constant}} = f(m). \tag{4.21}$$

Table 4.4, for example, shows the values of m for 50 μm $\times$ 10 μm $\times$ 2 μm biosensors to obtain desired LODs for various values of $P(\text{D})$ (0.1, 0.5, and 0.8). It can be seen that a higher number of biosensors is needed to obtain a lower LOD. In addition, the values of m were found to be largely dependent on the values of $P(\text{D})$, which can also be seen in Fig. 4.15. Hence, by using the derived Eqs. 4.17 and 4.20, one can estimate the LOD with a threshold probability of detection for a certain size and number of biosensors.

Table 4.4: Required number of biosensors, m, to obtain desired LODs for various values of $P(\mathrm{D})$ (0.1, 0.5, and 0.8).

Dimensions [μm]			**Number of wells**				
$\boldsymbol{L}$	$\boldsymbol{W}$	$\boldsymbol{T}$	$\boldsymbol{x^2}$	$\boldsymbol{n}$	$\boldsymbol{P(\mathrm{D})}$	$\boldsymbol{m}$	**LOD (cells/cm^2)**
50	10	2	52,000	1	0.1	5,200	3.85×10^0
50	10	2	52,000	10	0.1	545	3.85×10^1
50	10	2	52,000	100	0.1	55	3.85×10^2
50	10	2	52,000	1,000	0.1	6	3.85×10^3
50	10	2	52,000	1,0000	0.1	1	3.85×10^4
50	10	2	52,000	1	0.5	26,000	3.85×10^0
50	10	2	52,000	10	0.5	3,482	3.85×10^1
50	10	2	52,000	100	0.5	359	3.85×10^2
50	10	2	52,000	1,000	0.5	36	3.85×10^3
50	10	2	52,000	1,0000	0.5	4	3.85×10^4
50	10	2	52,000	1	0.8	41,600	3.85×10^0
50	10	2	52,000	10	0.8	7,730	3.85×10^1
50	10	2	52,000	100	0.8	830	3.85×10^2
50	10	2	52,000	1,000	0.8	83	3.85×10^3
50	10	2	52,000	1,0000	0.8	8	3.85×10^4

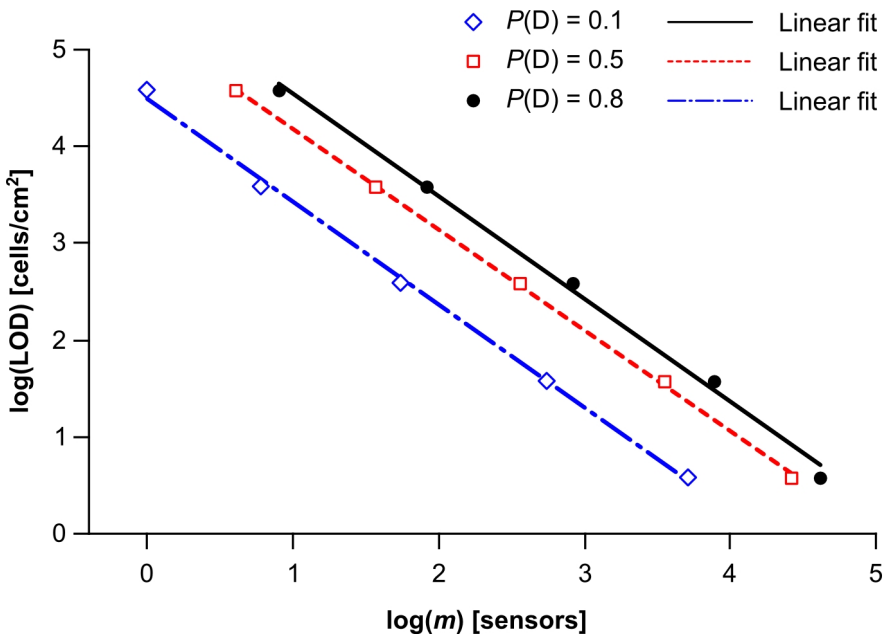

Figure 4.15: Dependence of the LOD on the number of biosensors (50 μm $\times$ 10 μm $\times$ 2 μm), m, for various values of P(D).

4.5 Conclusions

By placing freestanding, strip-shaped ME biosensors on leaf surfaces, rapid detection of *S.* Typhimurium ($<$ 45 min) without any pre-test sample preparation was realized. The LOD was found to be on the order of 10^4 to 10^5 cells/cm^2 for the three differently sized biosensors (2-mm, 0.5-mm, and 150-μm long sensors). Although the best results were obtained with the 150-μm long sensors (4.77×10^4 cells/cm^2 and 5.22×10^4 cells/cm^2 for the adaxial and abaxial surfaces of leaves), the LOD should be dependent not only on the size and mass sensitivity of biosensors, but also on the number of biosensors, the surface distribution of *S.* Typhimurium cells, and the topography of leaf surfaces.

In order to investigate the effects of the topography of leaf surfaces on the LOD, surface geometric parameters of mean roughness (R_a), mean flatness (F_a), and associated major periodicities (T_R and T_F) were quantified. Then, the characteristic sizes of biosensors free from the surface topography effects were determined.

Finally, a formula describing the probability of detection as a function of the size and number of biosensors and the surface density of *S.* Typhimurium was derived. By using the formula, the required number of biosensors to obtain a desired LOD can be determined.

Bibliography

[1] B. Lungu, W. D. Waltman, R. D. Berghaus, and C. L. Hofacre, "Comparison of a real-time PCR method with a culture method for the detection of *Salmonella enterica* serotype Enteritidis in naturally contaminated environmental samples from integrated poultry houses," *Journal of food protection*, vol. 75, no. 4, pp. 743 – 747, 2012.

[2] S. Artault, J. L. Blind, J. Delaval, Y. Dureuil, and N. Gaillard, "Detecting *Listeria monocytogenes* in food," *International Food Hygiene*, vol. 12, p. 23, 2001.

[3] B. Brooks, J. Devenish, C. Lutze-Wallace, D. Milnes, R. Robertson, and G. Berlie-Surujballi, "Evaluation of a monoclonal antibody-based enzyme-linked immunosorbent assay for detection of *Campylobacter fetus* in bovine preputial washing and vaginal mucus samples," *Veterinary Microbiology*, vol. 103, no. 12, pp. 77 – 84, 2004.

[4] E. L. Crowley, C. K. O'Sullivan, and G. G. Guilbault, "Increasing the sensitivity of *Listeria monocytogenes* assays: Evaluation using ELISA and amperometric detection," *Analyst*, vol. 124, pp. 295 – 299, 1999.

[5] L. P. Mansfield and S. Forsythe, "The detection of *Salmonella* serovars from animal feed and raw chicken using a combined immunomagnetic separation and ELISA method," *Food Microbiology*, vol. 18, no. 4, pp. 361 – 366, 2001.

[6] B. W. Blais, J. Leggate, J. Bosley, and A. Martinez-Perez, "Comparison of fluorogenic and chromogenic assay systems in the detection of *Escherichia coli* O157 by a novel polymyxin-based ELISA," *Letters in Applied Microbiology*, vol. 39, no. 6, pp. 516 – 522, 2004.

[7] P. G. Klein and V. K. Juneja, "Sensitive detection of viable *Listeria monocytogenes* by reverse transcription-PCR.," *Applied and Environmental Microbiology*, vol. 63, no. 11, pp. 4441 – 4448, 1997.

[8] P. Villari, E. Motti, C. Farullo, and I. Torre, "Comparison of conventional culture and PCR methods for the detection of *Legionella pneumophila* in water," *Letters in Applied Microbiology*, vol. 27, no. 2, pp. 106 – 110, 1998.

[9] J. A. Higgins, S. Nasarabadi, J. S. Karns, D. R. Shelton, M. Cooper, A. Gbakima, and R. P. Koopman, "A handheld real time thermal cycler for bacterial pathogen detection," *Biosensors and Bioelectronics*, vol. 18, no. 9, pp. 1115 – 1123, 2003.

[10] M. Lund, S. Nordentoft, K. Pedersen, and M. Madsen, "Detection of *Campylobacter* spp. in chicken fecal samples by real-time PCR," *Journal of Clinical Microbiology*, vol. 42, no. 11, pp. 5125 – 5132, 2004.

[11] G. C. Bokken, R. J. Corbee, F. van Knapen, and A. A. Bergwerff, "Immunochemical detection of *Salmonella* group B, D and E using an optical surface plasmon resonance biosensor," *FEMS Microbiology Letters*, vol. 222, no. 1, pp. 75 – 82, 2003.

[12] B.-K. Oh, Y.-K. Kim, K. W. Park, W. H. Lee, and J.-W. Choi, "Surface plasmon resonance immunosensor for the detection of *Salmonella typhimurium*," *Biosensors and Bioelectronics*, vol. 19, no. 11, pp. 1497 – 1504, 2004.

[13] H. J. Watts, C. R. Lowe, and D. V. Pollard-Knight, "Optical biosensor for monitoring microbial cells," *Analytical Chemistry*, vol. 66, no. 15, pp. 2465 – 2470, 1994.

[14] B. H. Schneider, J. G. Edwards, and N. F. Hartman, "Hartman interferometer: versatile integrated optic sensor for label-free, real-time quantification of nucleic acids, proteins, and pathogens," *Clinical Chemistry*, vol. 43, no. 9, pp. 1757 – 1763, 1997.

[15] J. Lehtinen, S. Järvinen, M. Virta, and E.-M. Lilius, "Real-time monitoring of antimicrobial activity with the multiparameter microplate assay," *Journal of Microbiological Methods*, vol. 66, no. 3, pp. 381 – 389, 2006.

[16] C. Ruan, H. Wang, and Y. Li, "A bienzyme electrochemical biosensor coupled with immunomagnetic separation for rapid detection of *Escherichia coli* O157:H7 in food samples," *Transactions of the ASABE*, vol. 45, no. 1, pp. 249 – 255, 2002.

[17] L. Yang, C. Ruan, and Y. LI, "Rapid detection of *Salmonella typhimurium* in food samples using a bienzyme electrochemical biosensor with flow injection," *Journal of Rapid Methods & Automation in Microbiology*, vol. 9, no. 4, pp. 229 – 240, 2001.

[18] L. Yang, Y. Li, C. L. Griffis, and M. G. Johnson, "Interdigitated microelectrode (IME) impedance sensor for the detection of viable *Salmonella typhimurium*," *Biosensors and Bioelectronics*, vol. 19, no. 10, pp. 1139 – 1147, 2004.

[19] D. W. Branch and S. M. Brozik, "Low-level detection of a *Bacillus anthracis* simulant using Love-wave biosensors on 36° YX $LiTaO_3$," *Biosensors and Bioelectronics*, vol. 19, no. 8, pp. 849 – 859, 2004.

[20] M.-K. Park, H. C. W. III, Y. Chai, S. Horikawa, W. Shen, and B. A. Chin, "The effect of incubation time for *Salmonella* Typhimurium binding to phage-based magnetoelastic biosensors," *Food Control*, vol. 26, no. 2, pp. 539 – 545, 2012.

[21] S. Li and Z.-Y. Cheng, "Nonuniform mass detection using magnetostrictive biosensors operating under multiple harmonic resonance modes," *Journal of Applied Physics*, vol. 107, p. 114514, 2010.

[22] Y. Chai, S. Li, S. Horikawa, M.-K. Park, V. Vodyanoy, and B. A. Chin, "Rapid and sensitive detection of *Salmonella* Typhimurium on eggshells by using wireless biosensors," *Journal of Food Protection*, vol. 75, no. 4, pp. 631 – 636, 2012.

[23] I. B. Sorokulova, E. V. Olsen, I.-H. Chen, B. Fiebor, J. M. Barbaree, V. J. Vodyanoy, B. A. Chin, and V. A. Petrenko, "Landscape phage probes for *Salmonella typhimurium*," *Journal of Microbiological Methods*, vol. 63, no. 1, pp. 55 – 72, 2005.

[24] G. Chinga, P. O. Johnssen, R. Dougherty, E. L. Berli, and J. Walter, "Quantification of the 3-D micro-structure of SC surfaces," *Journal of Microscopy*, vol. 227, pp. 254 – 265, 2007.

[25] M. L. Johnson, J. Wan, S. Huang, Z. Cheng, V. A. Petrenko, D.-J. Kim, I.-H. Chen, J. M. Barbaree, J. W. Hong, and B. A. Chin, "A wireless biosensor using microfabricated phage-interfaced magnetoelastic particles," *Sensors and Actuators A: Physical*, vol. 144, no. 1, pp. 38 – 47, 2008.

[26] S. Li, S. Horikawa, M. kyung Park, Y. Chai, V. J. Vodyanoy, and B. A. Chin, "Amorphous metallic glass biosensors," *Intermetallics*, vol. 30, no. 0, pp. 80 – 85, 2012.

[27] http://office.microsoft.com/en-us/excel-help/ttest-HP005209325.aspx.

[28] projectile.sv.cmu.edu/research/public/talks/t-test.htm\#types.

[29] R. M. Harshey, "Bacterial motility on a surface: Many ways to a common goal," *Annual Review of Microbiology*, vol. 57, pp. 249 – 273, 2003.

[30] B. Li and B. E. Logan, "Bacterial adhesion to glass and metal-oxide surfaces," *Colloids and Surfaces B: Biointerfaces*, vol. 36, pp. 81 – 90, 2004.

[31] J. L. Sebaugh and P. D. McCray, "Defining the linear portion of a sigmoid-shaped curve: bend points," *Pharmaceutical Statistics*, vol. 2, no. 3, pp. 167 – 174, 2003.

[32] R. P. Buck and E. Lindner, "Recomendations for nomenclature of ion-selective electrodes," *Pure and Applied Chemistry*, vol. 66, pp. 2527 – 2536, 1994.

[33] S. Sheen, G. Bao, and P. Cooke, "Food surface texture measurement using reflective confocal laser scanning microscopy," *Journal of Food S*, vol. 73, pp. E227 – E234, 2008.

[34] H. Wang, H. Feng, W. Liang, Y. Luo, and V. Malyarchuk, "Effect of surface roughness on retention and removal of *Escherichia coli* O157:H7 on surfaces of selected fruits," *Journal of Food Science*, vol. 74, pp. E8 – E15, 2009.

Chapter 5

Detection of *B. anthracis* Spores with the Aid of A Microfluidic Flow Cell

5.1 Introduction

The bacterium *B. anthracis*, among the Category A bioterrorism agents, has the ability to form a spore under starvation conditions. This spore is a dehydrated, thick-walled cell that can remain metabolically dormant for years and survive in a wide range of harsh environments [1]. Yet, once entering a nutrient-rich host, the spore can germinate and grow to a vast number of vegetative cells, which in turn causes the disease anthrax with high mortality rates. Although early, proper antibiotic treatments have proven effective in reducing the high mortality rates, such treatments are often difficult to provide due to initial, non-specific symptoms in infected patients [2]. Hence, anthrax infection is a significant public health-concern and must be prevented through early detection of *B. anthracis* spores preferably before their entry into the human body.

Since the 2001 anthrax mail attacks in the United States, substantial progress has been made in the development of label-free biosensors for the low-cost, rapid, on-site detection of *B. anthracis* spores. Among the most successful examples are mass-sensitive biosensors, such as those based on a cantilever and a quartz-crystal microbalance (QCM) as the signal transducer. These biosensors combined with an antibody as the biomolecular-recognition element have shown the potential to rapidly detect the spores at low concentrations (e.g., as few as 50 spores in water with 20 μm-long silicon cantilevers [3]; 300 spores/ml with piezoelectric-excited millimeter-sized cantilever sensors [4]; and 10^3 spores/ml with a QCM [5]). However, due to low thermal stability of antibodies in general, the outdoor use as well as longevity of

these antibody-based biosensors may be problematic [6]. As a result, there is a need for thermally robust biosensors that can function outdoors for a fair period of time while possessing cost-effectiveness, rapidness, and high sensitivity as the minimum performance requisites.

Phage-based ME biosensors, a class of wireless, mass-sensitive biosensors, are among potential candidates that could meet the above-mentioned need. These biosensors are composed of a freestanding, strip-shaped ME resonator as the wireless signal transducer and a thermally stable landscape phage as the biomolecular-recognition element [7–10]. Previously, a landscape phage with high binding affinity for *B. anthracis* spores has been reported (i.e., the JRB7 phage with a binding peptide sequence of EPRLSPHS [11]). ME biosensors based on this phage have shown the retention of binding activity at various temperatures (25, 45, and 65 °C) for at least a hundred days. By contrast, the best antibody-based ME biosensors tested alongside have retained binding activity for a maximum of 5 days at 65 °C [12]. In addition, the phage-based ME biosensors are not only inexpensive and rapid in response time, but they can be easily replaced after use due to their wireless nature, which may facilitate the on-site monitoring of the presence of the spores. However, a remaining key issue has been sensitivity. Theoretically, sensitivity improves as the size of the ME resonator is reduced [13]. Hence, efforts have been made to manufacture and use small-sized resonators for the sensitive detection of *B. anthracis* spores [12, 14–16]. However, due to the challenge in acquiring a measurable transduced signal from small-sized resonators, their length has been limited to millimeters to half a millimeter (5 to 0.5 mm), which are not significantly small to enable the detection of a few spores (e.g., on the order of 10 or less). In other words, further reduction in the size of the resonator is needed for the ME biosensors to be competitive in sensitivity. In addition, when such miniature ME biosensors are used with a traditional large flow cell, the chances of physical contact between the biosensor and spores in the flow cell is greatly reduced.

This speculation points to a need for a properly designed microfluidic flow cell that efficiently guides a stream of the spores towards the biosensor. Hence, this chapter presents an investigation into the potential use of a micron-scale phage-based ME biosensor combined with a microfluidic flow cell for the rapid, sensitive detection of *B. anthracis* spores. In this work, 200 μm-long ME resonators were batch-fabricated and used (i.e., $\sim 10^6$ resonators on a four-inch wafer). In this way, the fabrication cost per resonator was reduced to a fraction of a cent, which allows the biosensors to be disposable, and thus, free of cross-contamination.

5.2 Material and methods

5.2.1 JRB7 phage and *B. anthracis* Sterne spores

Suspensions of the JRB7 phage (5×10^{11} virions/ml in a PBS buffer, pH 7.2) and *B. anthracis* Sterne spores (5×10^8 spores/ml in sterile distilled water) were kindly provided by Dr. James Barbaree's group at Auburn University. The Sterne strain of *B. anthracis* is an attenuated strain that is incapable of causing anthrax infection in humans and, thus, convenient for safe laboratory experiments. Yet, all antigenic markers on the external surface of a Sterne spore are common with those of a pathogenic spore. Hence, the binding characteristics of the affinity-selected JRB7 phage to the Sterne and pathogenic spores are expected to be identical. The concentrated spore suspension was diluted with sterile distilled water as desired prior to use.

5.2.2 Batch-fabrication of micron-scale ME resonators

ME resonators with a size of 200 μm $\times$ 40 μm $\times$ 4 μm were batch-fabricated using the co-sputtering-based method described in Chapter 3. Figure 5.1 shows scanning electron micrographs of the fabricated ME resonators. After lift-off, these ME resonators were annealed and immobilized with the JRB7 phage.

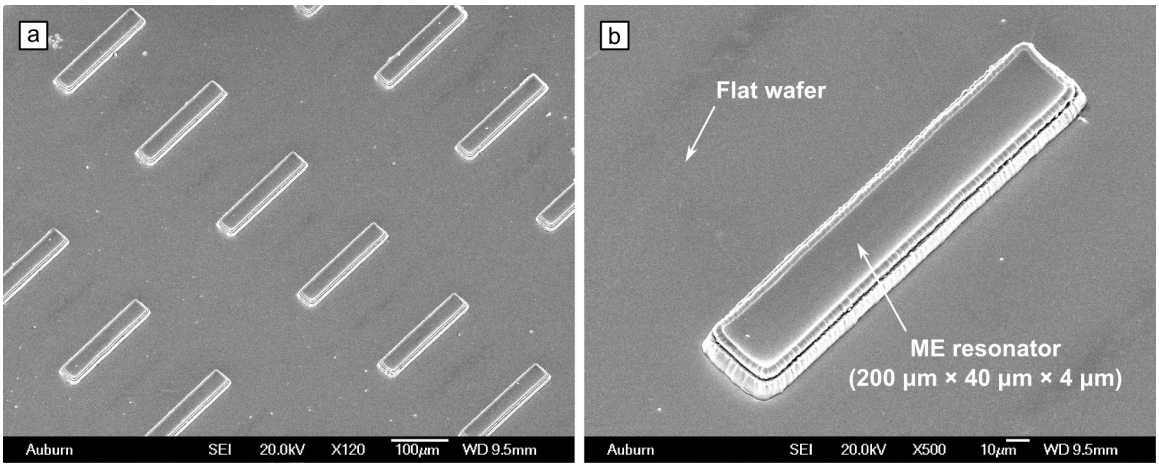

Figure 5.1: Scanning electron micrographs of 200 μm $\times$ 40 μm $\times$ 4 μm ME resonators fabricated on a flat wafer: (a) batch-fabricated resonators and (b) a close-up view.

5.2.3 Microfluidic flow cells

In order to ensure efficient physical contact between the biosensor and *B. anthracis* spores, microfluidic flow cells were designed and fabricated of a silicone elastomer, poly(dimethylsiloxane) (PDMS), by multilayer soft lithography (Fig. 5.2). In this investigation, the following two types of flow cells were fabricated and used:

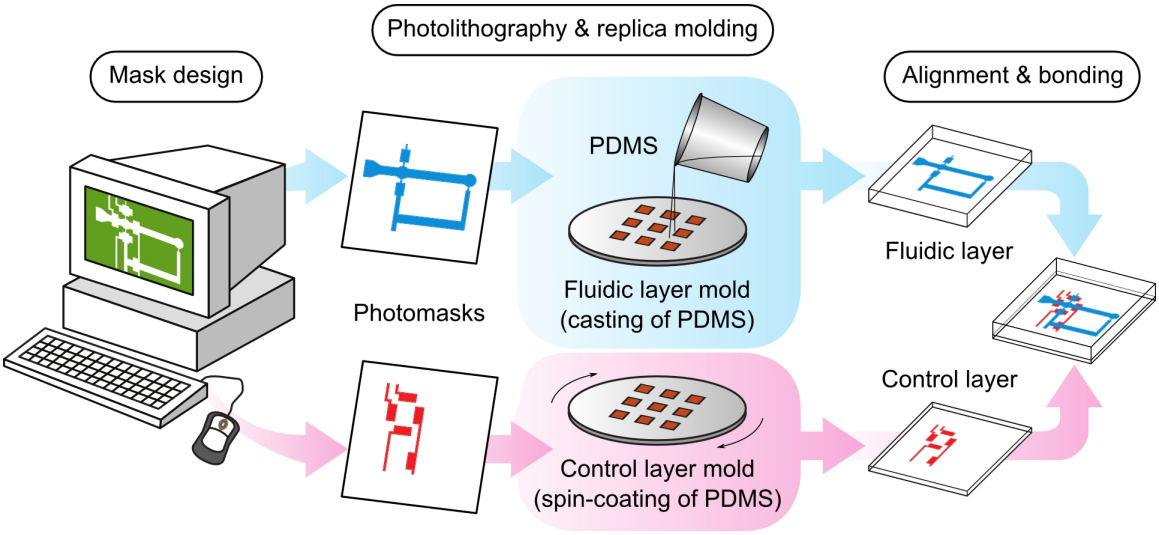

Figure 5.2: Procedure for the fabrication of a microfludic chip by multilayer soft lithography.

1. Type I microfluidic flow cell with pneumatic push-up valves for a proof-of-concept experiment (i.e., manipulation of sensors and micro-spheres).

2. Type II microfluidic flow cell with pneumatic push-down valves integrated with an ME biosensor for the rapid, sensitive detection of *B. anthracis* spores.

5.2.3.1 Design and fabrication of the Type I microfluidic flow cell

The design of the Type I microfluidic flow cell is shown in Fig. 5.3. The flow cell is composed of one reaction chamber (300 μm $\times$ 300 μm $\times$ 50 μm) and four channels that were used for the injection and removal of a sensor and micro-spheres. Pneumatic push-up valves were used to open and close the connections between the chamber and channels. Two PDMS layers, the fluidic and control layers, are needed to realize this actuation mechanism. The control layer mold was fabricated using the SPR 220-7.0 photoresist (Rohm and Haas Electronic Materials, LLC.) with a typical height of 15 μm. By contrast, the mold for the fluidic layer was manufactured using two different photoresists, AZ P4620 (AZ Electronic Materials USA Corp.) and SU-8 2025 (Microchem Corp.) for micro-features of different height. The fabricated micro-features shown in blue and green lines in Fig. 5.3 have typical heights of 20 μm and 50 μm, respectively.

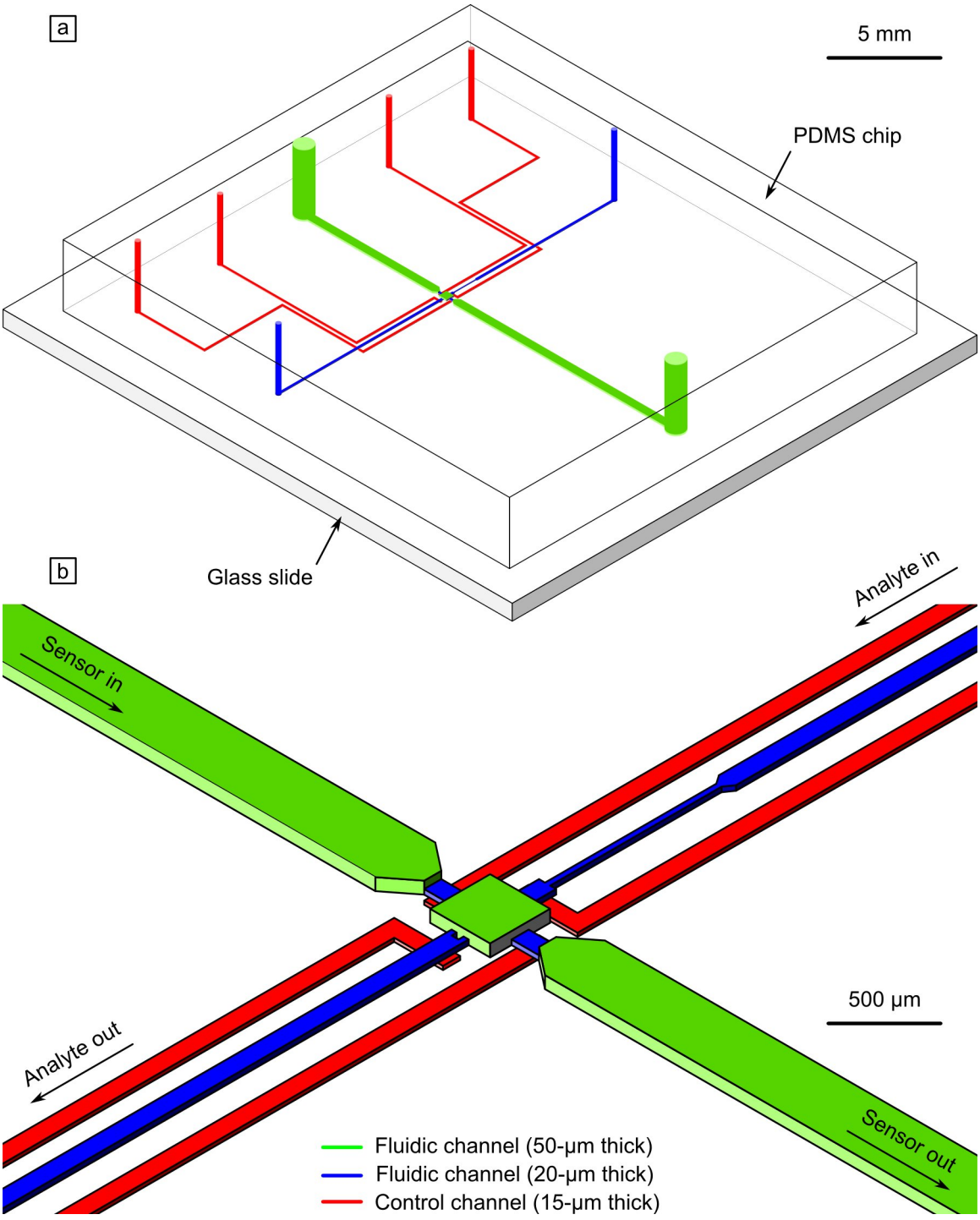

Figure 5.3: Design of the Type I flow cell: (a) a three-dimensional view of the whole chip and (b) a close-up view of the key elements of the chip.

Commercially available GE RTV 615 was used to make the PDMS microfluidic flow cell. Typically, 5 parts of GE RTV 615 part A (base) was mixed thoroughly with 1 part of part B (curing agent), followed by degasification under vacuum for 1 to 2 hours. This mixture was, then, gently poured onto the fluidic layer mold and cured at 80 °C for 45 min. When cooled down, the PDMS replica was gently peeled off the mold. After access holes were punched into this replica, this PDMS fluidic layer was stored in a clean-room chamber until use. For the fabrication of the PDMS control layer, 20 parts of GE RTV 615 A was mixed thoroughly with 1 part of part B, followed by degasification under vacuum for 15 minutes. The mixture was, then, spin-coated onto the control layer mold at a rotation speed of 3,200 rpm for 120 sec and cured at 80 °C for 30 min. The PDMS fluidic layer, which was pre-cleaned with methanol and dried, was, then, aligned to the control layer using an optical microscope. Afterwards, the aligned chip was cured at 80 °C for 4 hours to complete the bonding between the two layers. The final chip was sealed against a clean glass slide, which was pre-coated with a thin layer of PDMS. The final bonding between the chip and glass slide was performed at 80 °C for 4 hours.

5.2.3.2 Design and fabrication of the Type II microfluidic flow cell

The design of the Type II microfluidic flow cell is similar to that of Type I. The differences between them are as follows:

1. The Type II flow cell has push-down valves (Fig. 5.4). In other words, the control layer is located on the fluidic layer.

2. The Type II flow cell was sealed against a slotted glass slide, which facilitates the collection of an ME biosensor after exposure to *B. anthracis* spores for subsequent resonant frequency measurement. Figure 5.5 shows the design of the Type II flow cell.

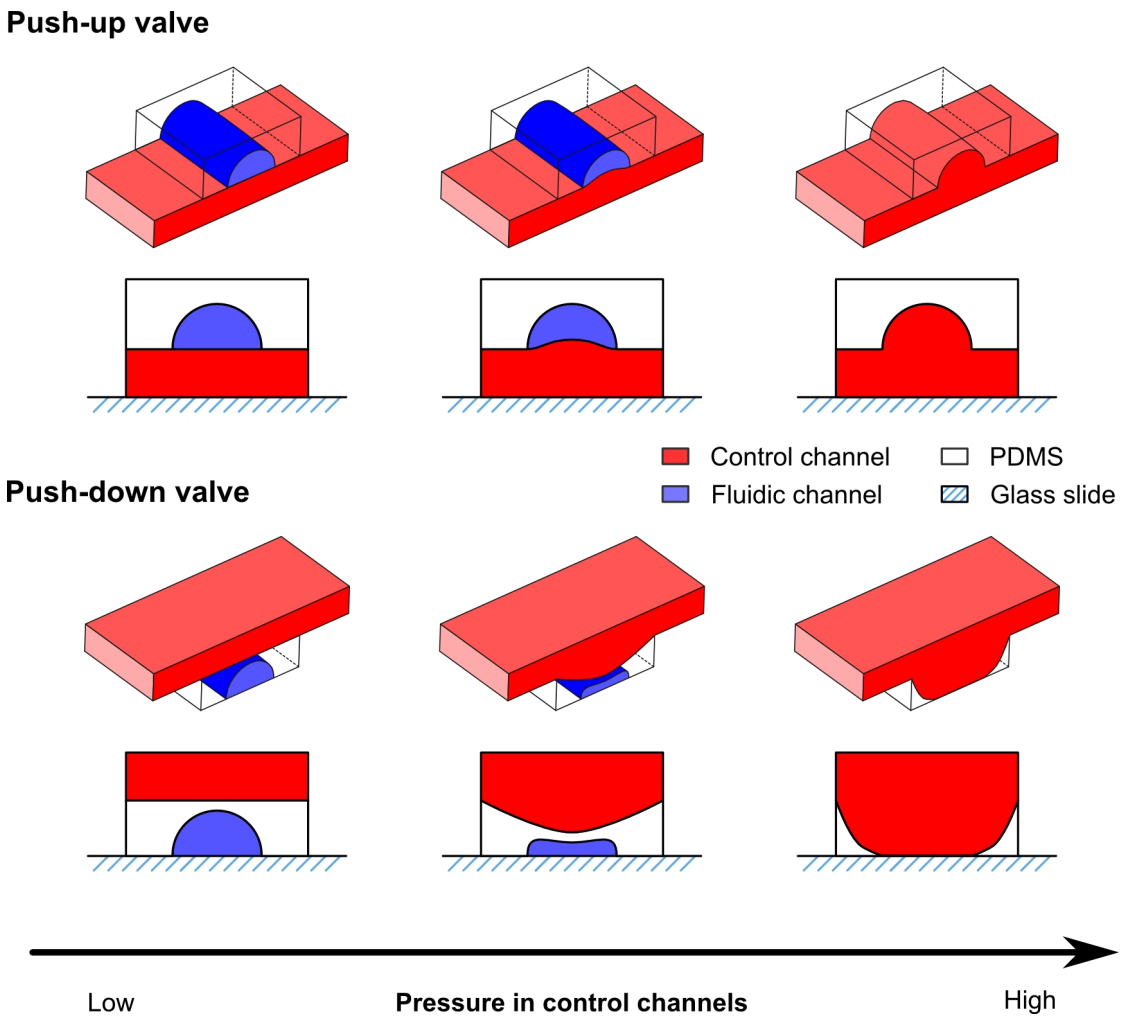

Figure 5.4: Push-up and push-down valves.

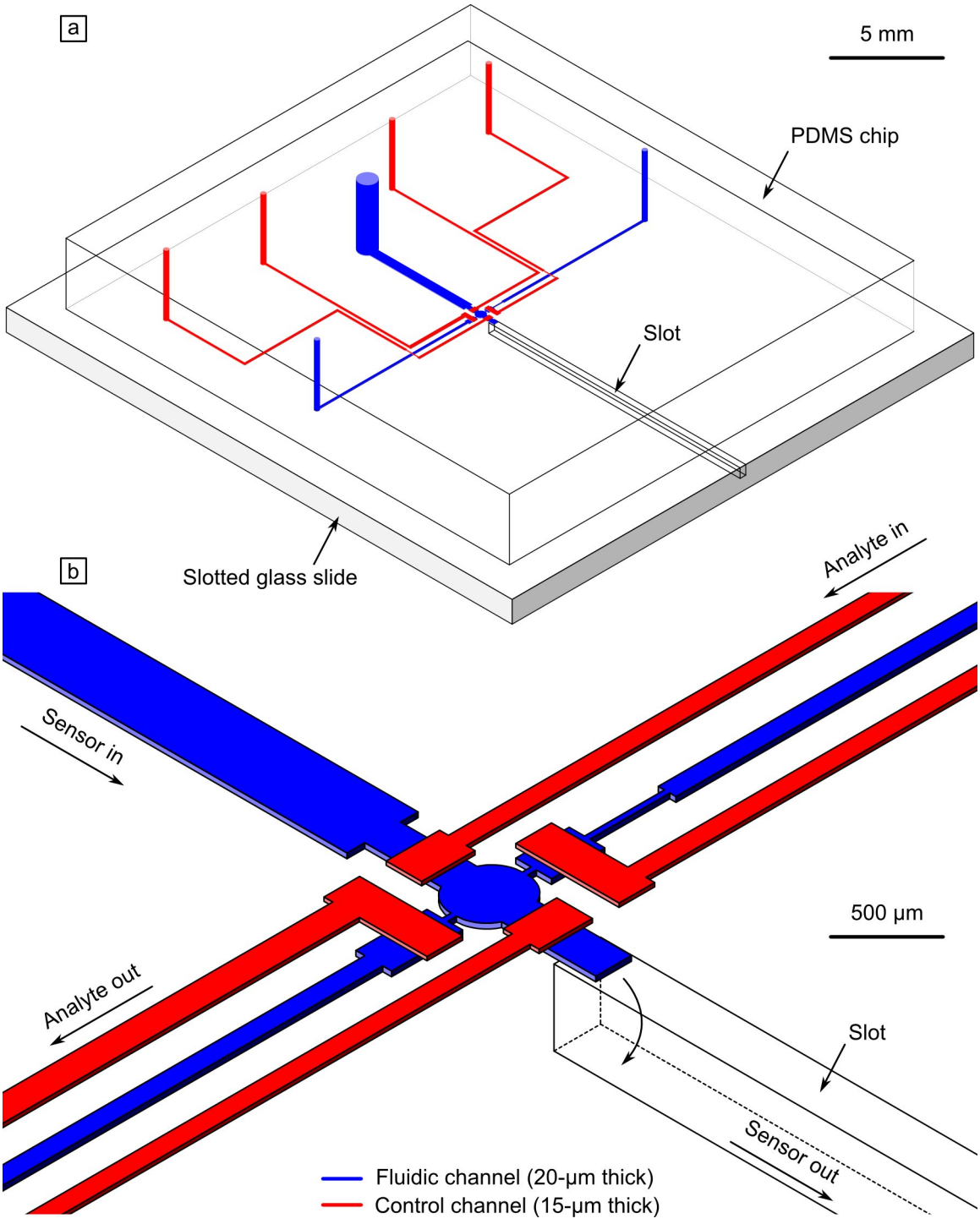

Figure 5.5: Design of the Type II flow cell: (a) a three-dimensional view of the whole chip on a slotted glass slide and (b) a close-up view of the key elements of the chip.

5.3 Valve actuation and sample injection

The actuation of pneumatic valves was tested with a controlled pressure from a nitrogen gas source. Fluidic pressure controllers and manifolds (Fluidigm corporation) were used to control the pressure supply to the control channels filled with water. For the fluidic channels, a much smaller pressure was needed to control the travel speed of analytes (i.e., micro-spheres and spores). Hence, a digital pressure gauge (DPG1203-005 from Omega Engineering Inc.) connected with a low pressure regulator (Go Regulator Company) was used to adjust the pressure required for the manipulation of the analytes. Flexible polymeric tubing (TYGON from Saint-Gobain PPL Corp.) and metal pins were connected to inject liquid samples into chips as shown in Fig. 5.6.

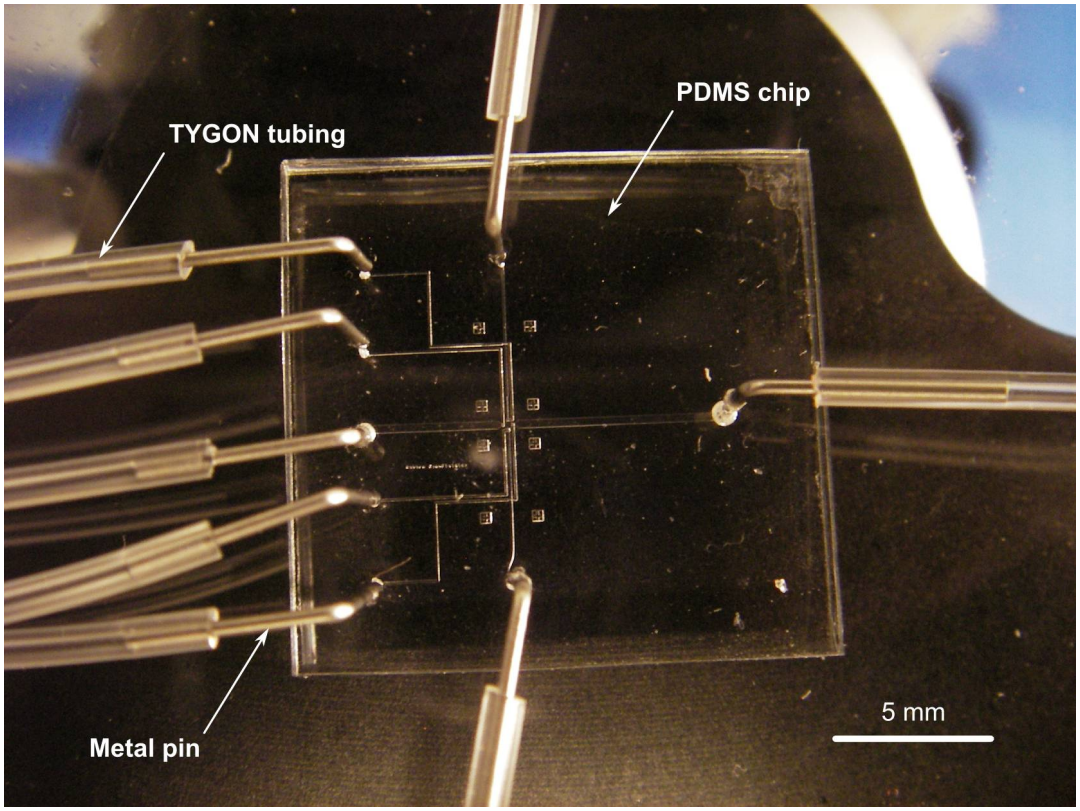

Figure 5.6: A close-up top view of a fabricated chip (Type I), connected to external pressure sources for valve actuation and sample injection.

5.4 Results and discussion

5.4.1 Confirmation of valve actuation

Valve actuation was confirmed by optical microscopic observation. As shown in Fig. 5.7a, all the four valves of a Type I flow cell were successfully closed at a pressure of 15 psi. In this way, the center chamber can be separated from all the connected fluidic lines, which enables the mechanical separation of any tiny analyte when injected into the flow cell. To further test the separation capabilities of the flow cell, a green food dye was injected into the chamber through the vertical fluidic channels while the #2 and #4 valves were kept closed. As can be seen in Fig. 5.7b, the green dye only filled the chamber, and no leakage towards the horizontal fluidic channels occurred.

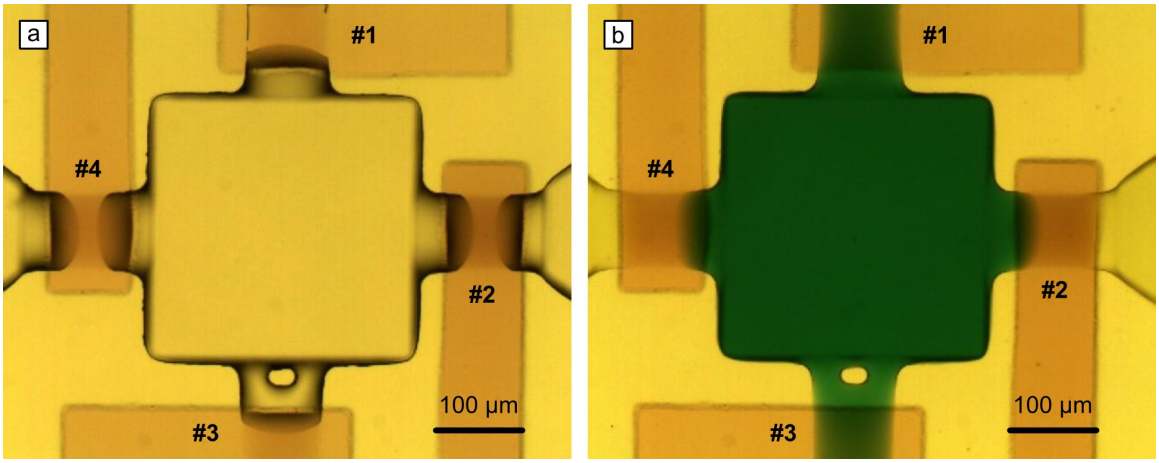

Figure 5.7: Close-up top views of a Type I flow cell: (a) All the valves (#1 through #4) are closed, and (b) only the #2 and #4 valves are closed such that the green dye injected through the vertical channels can only fill out the center chamber.

5.4.2 Manipulation of fluorescent-labeled micro-spheres

Fluorescent-labeled micro-spheres that have equivalent dimensions to *B. anthracis* spores (about 1.5 μm) were used to test the manipulation capabilities of the Type I microfluidic flow cell. The micro-spheres were injected through the vertical

fluidic channels and traced under an inverted fluorescence microscope (Axiovert 40 CFL from Carl Zeiss, Inc.). Once a desired number of spheres reached the chamber, they were isolated by closing valves. The results in Fig. 5.8 show the feasibility of manipulating a small number of micro-spheres. Figures 5.8a to 5.8c show the separation of four spheres, two spheres, and one sphere, respectively.

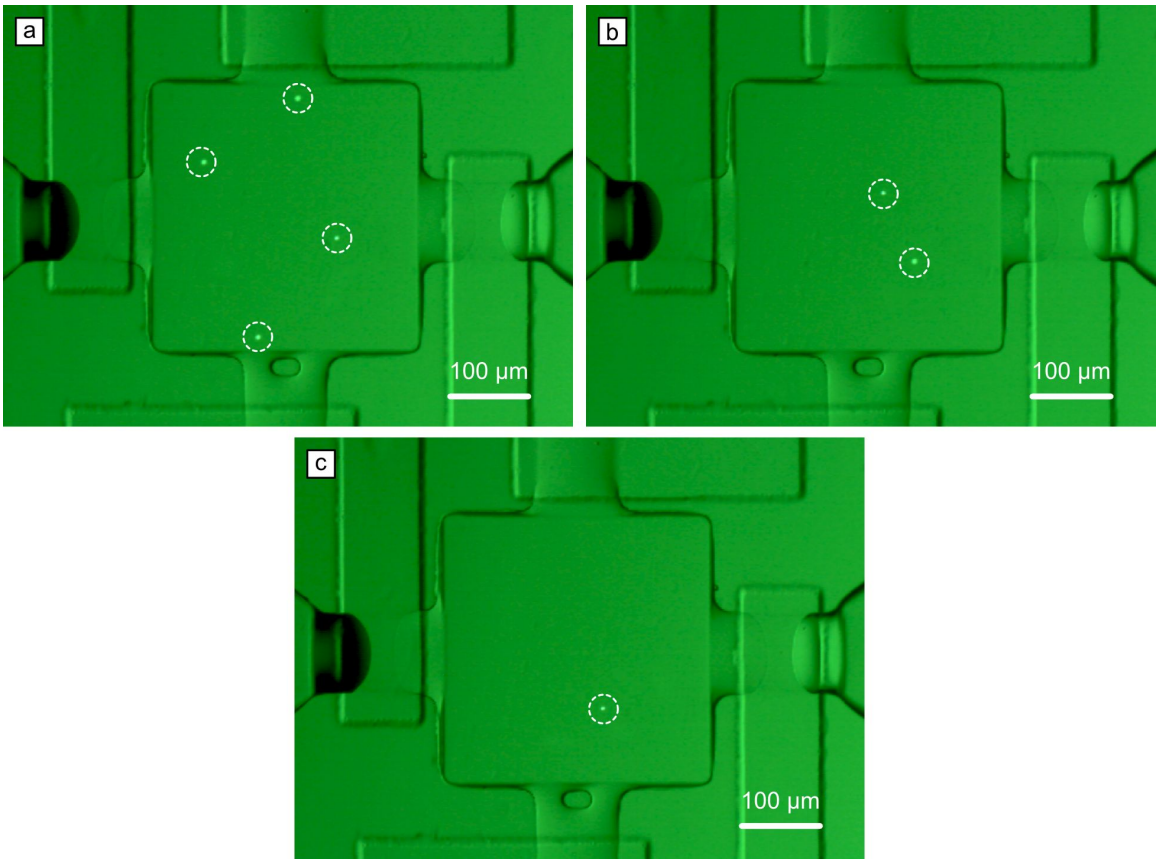

Figure 5.8: Fluorescent micrographs showing that the flow cell can separate a few micro-spheres into the reaction chamber: (a) separation of four spheres, (b) two spheres, and (c) one sphere.

5.4.3 Manipulation of a sensor

Similarly, a sensor can be injected through the horizontal channels and positioned in the reaction chamber as shown in Fig. 5.9.

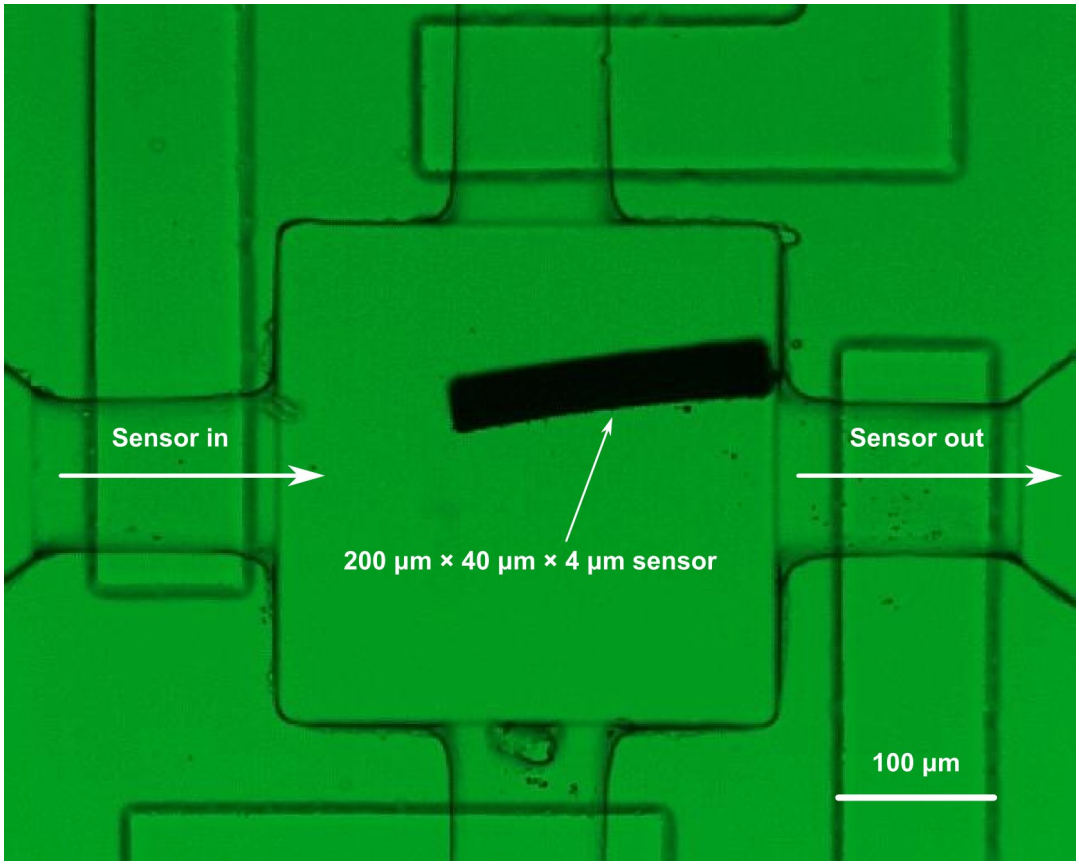

Figure 5.9: Injection of a 200 μm $\times$ 40 μm $\times$ 4 μm sensor into the chamber through the horizontal channels.

5.4.4 Detection of *B. anthracis* spores with the Type II microfluidic flow cell

With the Type I micofluidic flow cell, the potential usefulness of a polymeric microfludic system with pneumatic valves was verified. For the enhanced detection of *B. anthracis* spores, the Type II flow cell in combination with a 200 μm-long ME biosensor was employed. The Type II flow cell was sealed on a slotted glass slide, which facilitates the collection of the ME biosensor after exposure to *B. anthracis* spores for subsequent resonant frequency measurement. Figure 5.10 shows an optical micrograph of the key elements of the Type II microfluidic flow cell. In this flow cell, *B. anthracis* spores were injected and removed though the vertical channels at a flow velocity of 100 to 150 μm/s in the circular reaction chamber, whereas the

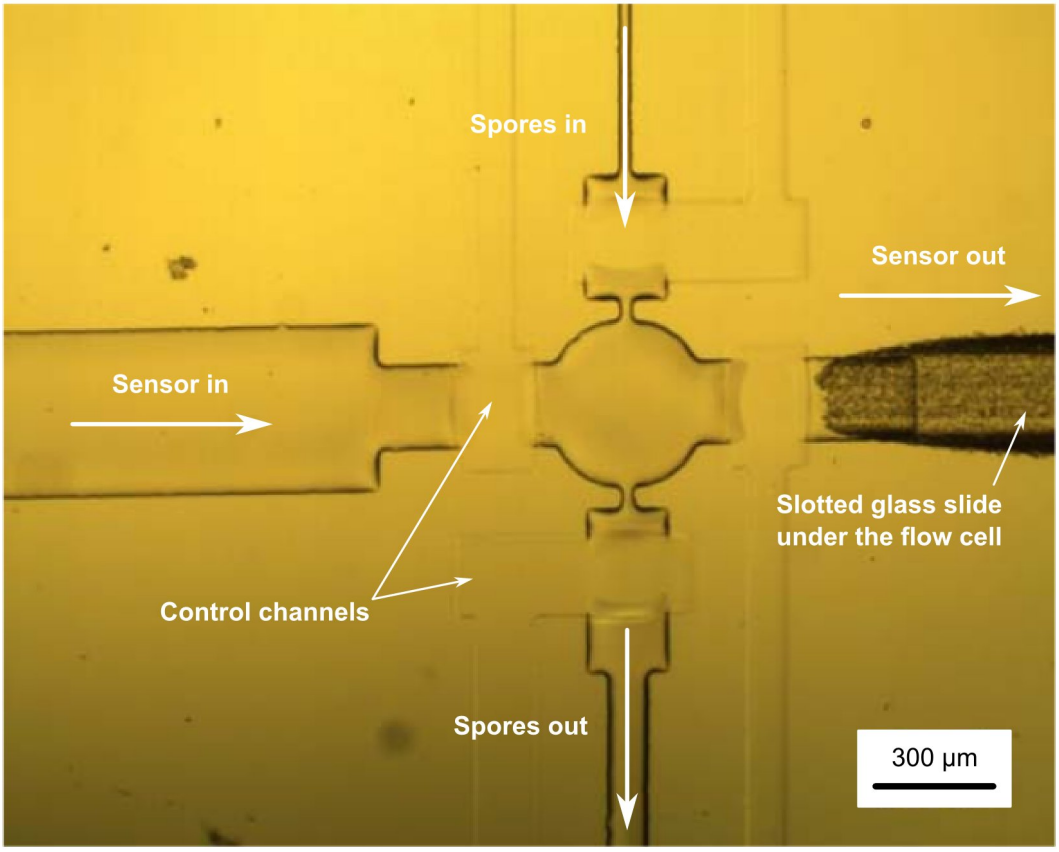

Figure 5.10: Optical micrograph of the Type II microfluidic flow cell. All the push-down valves are closed.

ME biosensor was moved through the horizontal channels using a bar magnet. After exposure to *B. anthracis* spores in the chamber, the sensor was collected through the slot in the glass slide, which is located under the flow cell. A representative image of the testing is shown in Fig. 5.11, where the binding of fluorescent-labeled spores on a 200 μm $\times$ 40 μm $\times$ 4 μm ME biosensor can be seen. Interestingly, the binding process occurred very quickly (on the order of minutes), which can be monitored in a real-time manner using the microscope. After this binding step, the biosensor was collected, and measurement of it's final resonant frequency was completed within 5 min. Hence, the total assay time was only about 10 min.

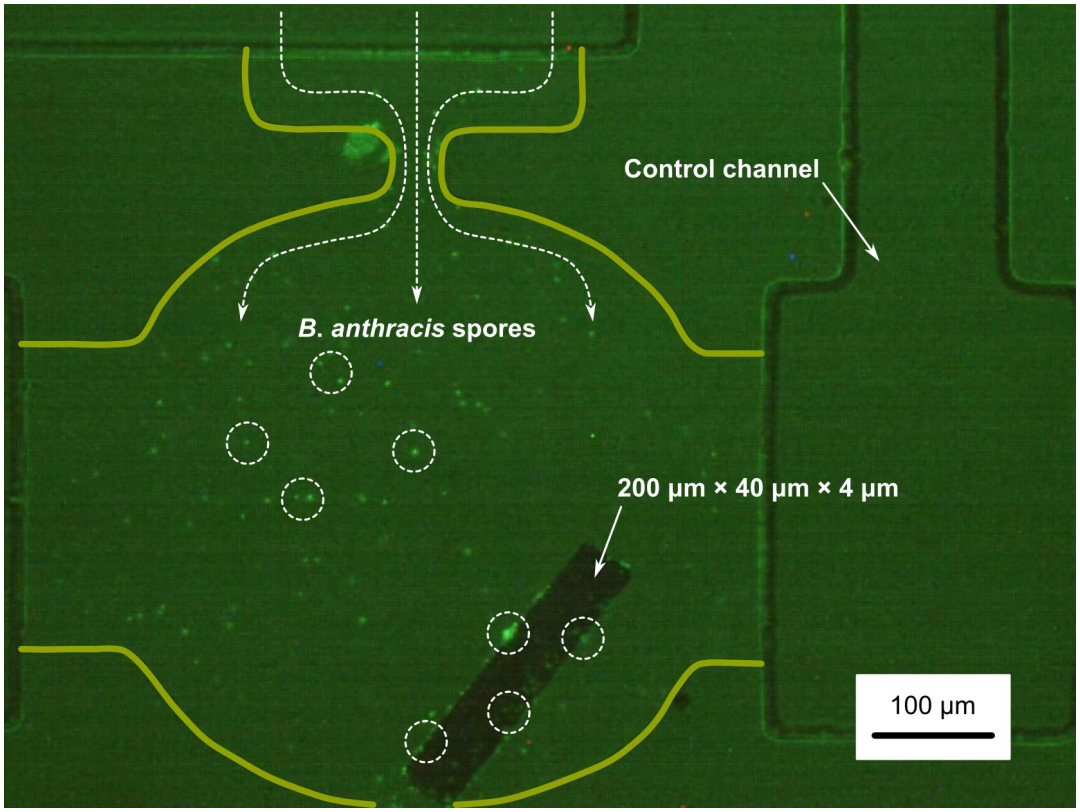

Figure 5.11: Fluorescent micrograph showing *B. anthracis* spores are bound on a 200 μm $\times$ 40 μm $\times$ 4 μm ME biosensor. The chamber was outlined with a yellow solid line for better visualization.

Figure 5.12 shows a result of a streamline analysis using the Caedium software [17]. The streamlines represent the instantaneous paths of massless particles. Due to the limited paths that spores can take in the micron-scale flow cell, the chances of physical contact between the sensor and spores were greatly enhanced. In addition, the flow velocity in the reaction chamber was found to be low when compared with those in the connected fluidic channels. This decreased velocity is also likely to facilitate the binding of spores on the sensor surfaces.

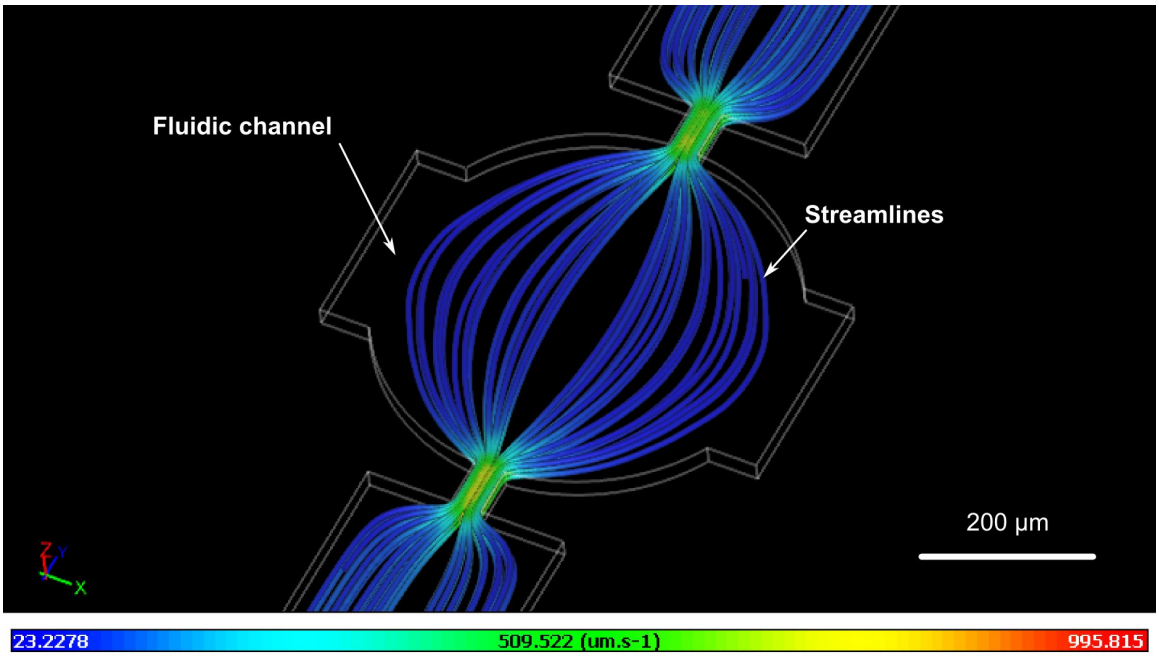

Figure 5.12: Streamlines in the microfluidic flow cell. The color bar below indicates the magnitude of flow velocity.

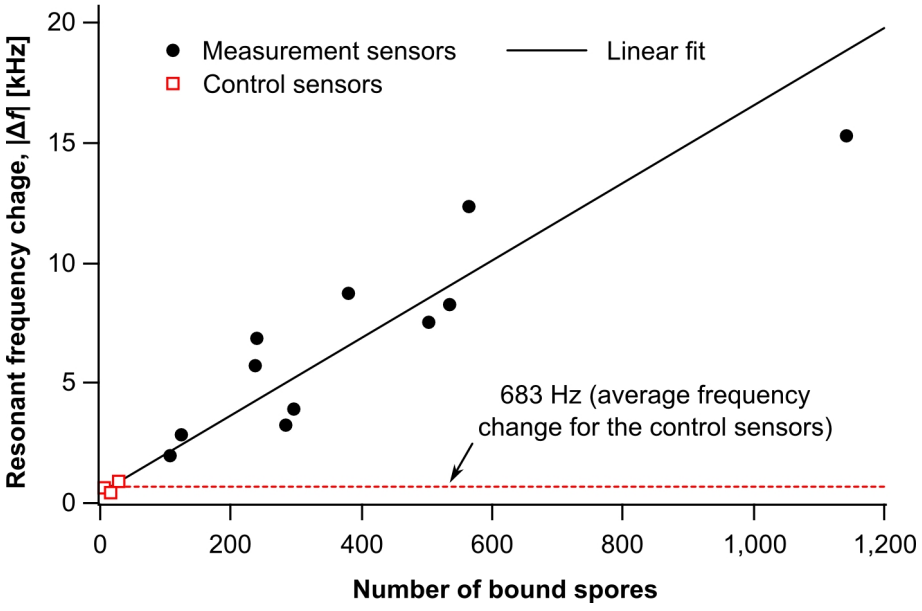

Figure 5.13: Responses of ME biosensors (200 μm $\times$ 40 μm $\times$ 4 μm) to various numbers of spores.

Finally, Fig. 5.13 shows responses of 200 μm $\times$ 40 μm $\times$ 4 μm ME biosensors to various numbers of *B. anthracis* spores. As can be seen, resonant frequency changes for measurement sensors (black circles) were largely dependent on the number of bound spores. At 106 spores, a minimum frequency change of 1,993 Hz was obtained. In addition, the same experimental procedure was used to test control sensors, which were not immobilized with the JRB7 phage but only surface-blocked with BSA. The number of non-specifically bound spores on the control sensors was found to be very small (6 to 28 spores), and the average of the corresponding resonant frequency changes was 683 $\pm$ 240 Hz. This average response is much smaller than the minimum response of the measurement sensors (i.e., 1,993 Hz for 106 spores). Hence, it can be concluded that 200 μm-long ME biosensors were capable of detecting 106 spores. All the dose-response data are summarized in Table 5.1.

Table 5.1: Number of bound spores and corresponding resonant frequency changes for measurement and control sensors.

Sample #	**Number of bound spores**	**Resonant frequency change [Hz]**
Measurement 1	238	6,890
Measurement 2	282	3,299
Measurement 3	124	2,865
Measurement 4	534	8,270
Measurement 5	562	12,390
Measurement 6	106	1,993
Measurement 7	1,142	15,299
Measurement 8	296	3,968
Measurement 9	502	7,562
Measurement 10	236	5,739
Measurement 11	378	8,768
Control 1	6	638
Control 2	28	943
Control 3	14	469

5.5 Conclusions

PDMS microfluidic flow cells were designed, fabricated, and used with 200 μm $\times$ 40 μm $\times$ 4 μm ME biosensors for the enhanced detection of *B. anthracis* spores. Due to the enhanced chances of physical contact between the biosensors and spores, the time required for the testing was only about 10 min. In addition, with the micron-scale ME biosensors, down to 106 spores were experimentally detected.

Bibliography

[1] A. Driks, "The *Bacillus anthracis* spore," *Molecular Aspects of Medicine*, vol. 30, no. 6, pp. 368 – 373, 2009.

[2] T. V. Inglesby, T. O'Toole, D. A. Henderson, J. G. Bartlett, M. S. Ascher, E. Eitzen, A. M. Friedlander, J. Gerberding, J. Hauer, J. Hughes, J. McDade, M. T. Osterholm, G. Parker, T. M. Perl, P. K. Russell, and K. Tonat, "Anthrax as a biological weapon, 2002: Updated recommendations for management," *The Journal of the American Medical Association*, vol. 287, no. 17, pp. 2236 – 2252, 2002.

[3] A. P. Davila, J. Jang, A. K. Gupta, T. Walter, A. Aronson, and R. Bashir, "Microresonator mass sensors for detection of *Bacillus anthracis* Sterne spores in air and water," *Biosensors and Bioelectronics*, vol. 22, no. 12, pp. 3028 – 3035, 2007.

[4] G. A. Campbell and R. Mutharasan, "Detection of *Bacillus anthracis* spores and a model protein using PEMC sensors in a flow cell at 1 mL/min," *Biosensors and Bioelectronics*, vol. 22, no. 1, pp. 78 – 85, 2006.

[5] R. Hao, D. Wang, X. Zhang, G. Zuo, H. Wei, R. Yang, Z. Zhang, Z. Cheng, Y. Guo, Z. Cui, and Y. Zhou, "Rapid detection of *Bacillus anthracis* using monoclonal antibody functionalized QCM sensor," *Biosensors and Bioelectronics*, vol. 24, no. 5, pp. 1330 – 1335, 2009.

[6] V. A. Petrenko, "Landscape phage as a molecular recognition interface for detection devices," *Microelectronics Journal*, vol. 39, no. 2, pp. 202 – 207, 2008.

[7] Y. Chai, S. Li, S. Horikawa, M.-K. Park, V. Vodyanoy, and B. A. Chin, "Rapid and sensitive detection of *Salmonella* Typhimurium on eggshells by using wireless biosensors," *Journal of Food Protection*, vol. 75, no. 4, pp. 631 – 636, 2012.

[8] S. Horikawa, D. Bedi, S. Li, W. Shen, S. Huang, I.-H. Chen, Y. Chai, M. L. Auad, M. J. Bozack, J. M. Barbaree, V. A. Petrenko, and B. A. Chin, "Effects of surface functionalization on the surface phage coverage and the subsequent performance of phage-immobilized magnetoelastic biosensors," *Biosensors and Bioelectronics*, vol. 26, no. 5, pp. 2361 – 2367, 2011.

[9] S. Li and Z.-Y. Cheng, "Nonuniform mass detection using magnetostrictive biosensors operating under multiple harmonic resonance modes," *Journal of Applied Physics*, vol. 107, p. 114514, 2010.

[10] M.-K. Park, H. C. W. III, Y. Chai, S. Horikawa, W. Shen, and B. A. Chin, "The effect of incubation time for *Salmonella* Typhimurium binding to phage-based magnetoelastic biosensors," *Food Control*, vol. 26, no. 2, pp. 539 – 545, 2012.

[11] J. Brigati, D. D. Williams, I. B. Sorokulova, V. Nanduri, I.-H. Chen, C. L. Turnbough, and V. A. Petrenko, "Diagnostic probes for *Bacillus anthracis* spores selected from a landscape phage library," *Clinical Chemistry*, vol. 50, no. 10, pp. 1899 – 1906, 2004.

[12] J. Wan, H. Shu, S. Huang, B. Fiebor, I.-H. Chen, V. A. Petrenko, and B. A. Chin, "Phage-based magnetoelastic wireless biosensors for detecting *Bacillus anthracis* spores," *IEEE Sensors Journal*, vol. 7, pp. 470 – 477, 2007.

[13] C. A. Grimes, C. S. Mungle, K. Zeng, M. K. Jain, W. R. Dreschel, M. Paulose, and K. G. Ong, "Wireless magnetoelastic resonance sensors: A critical review," *Sensors*, vol. 2, pp. 294 – 313, 2002.

[14] S. Huang, H. Yang, R. Lakshmanan, M. Johnson, J. Wan, I.-H. Chen, H. W. III, V. Petrenko, J. Barbaree, and B. Chin, "Sequential detection of *Salmonella typhimurium* and *Bacillus anthracis* spores using magnetoelastic biosensors," *Biosensors and Bioelectronics*, vol. 24, no. 6, pp. 1730 – 1736, 2009.

[15] M. L. Johnson, J. Wan, S. Huang, Z. Cheng, V. A. Petrenko, D.-J. Kim, I.-H. Chen, J. M. Barbaree, J. W. Hong, and B. A. Chin, "A wireless biosensor using microfabricated phage-interfaced magnetoelastic particles," *Sensors and Actuators A: Physical*, vol. 144, no. 1, pp. 38 – 47, 2008.

[16] J. Wan, M. L. Johnson, R. Guntupalli, V. A. Petrenko, and B. A. Chin, "Detection of *Bacillus anthracis* spores in liquid using phage-based magnetoelastic micro-resonators," *Sensors and Actuators B: Chemical*, vol. 127, no. 2, pp. 559 – 566, 2007.

[17] http://www.symscape.com/.

Chapter 6

Enhancing the Detection Capabilities of Phage-Based ME Biosensors

In this chapter, the following two effects will be investigated to further enhance the detection capabilities of phage-based ME biosensors:

1. Effects of mass position on the sensitivity of ME biosensors
2. Effects of surface functionalization on surface phage coverage.

6.1 Effects of mass position on the mass sensitivity of ME biosensors

6.1.1 Introduction

One of the ultimate goals to be reached for phage-based ME biosensors is the real-time detection of single pathogenic bacteria. Although the principle of detection for freestanding, strip-shaped ME biosensors has been well documented, conventional theories describe only the case where attached masses are uniformly distributed over the ME sensors [1]. For non-uniformly distributed masses, the mass sensitivity of ME sensors is largely dependent on the position of the masses attached to the sensor surfaces [2]. Considering this dependence is crucial to detection of dilute analytes (e.g., low-concentration bacterial samples) because their local attachment may cause varying sensor responses. To address the issue, three-dimensional finite element (FE) models were constructed for differently sized phage-based biosensors with a single localized mass. The FE simulations allow one to predict the mass-position-dependent resonant frequency changes of biosensors.

6.1.2 Material and methods

6.1.2.1 Microcontact printing

In order to address the issue, resonant frequency measurements of phage-based ME biosensors with localized masses were first performed. Gold-coated ME sensor platforms (4 mm × 0.8 mm × 30 μm), made of Metglas 2826MB (from Honeywell International, Inc.), were manufactured with the procedure described in Chapter 3. The sensor platforms were, then, loaded with the SAE10 phage, which specifically binds with streptavidin (See Table 3.3), and finally with BSA (0.1 % w/v in 330-μl, 100-mM HEPES) for surface blocking. Microcontact printing was used to locally place streptavidin-coated polystyrene beads (hereafter, SA beads, 0.68 ± 0.11 μm in diameter, from Spherotech, Inc.) on the phage-based ME biosensors as shown in Fig.

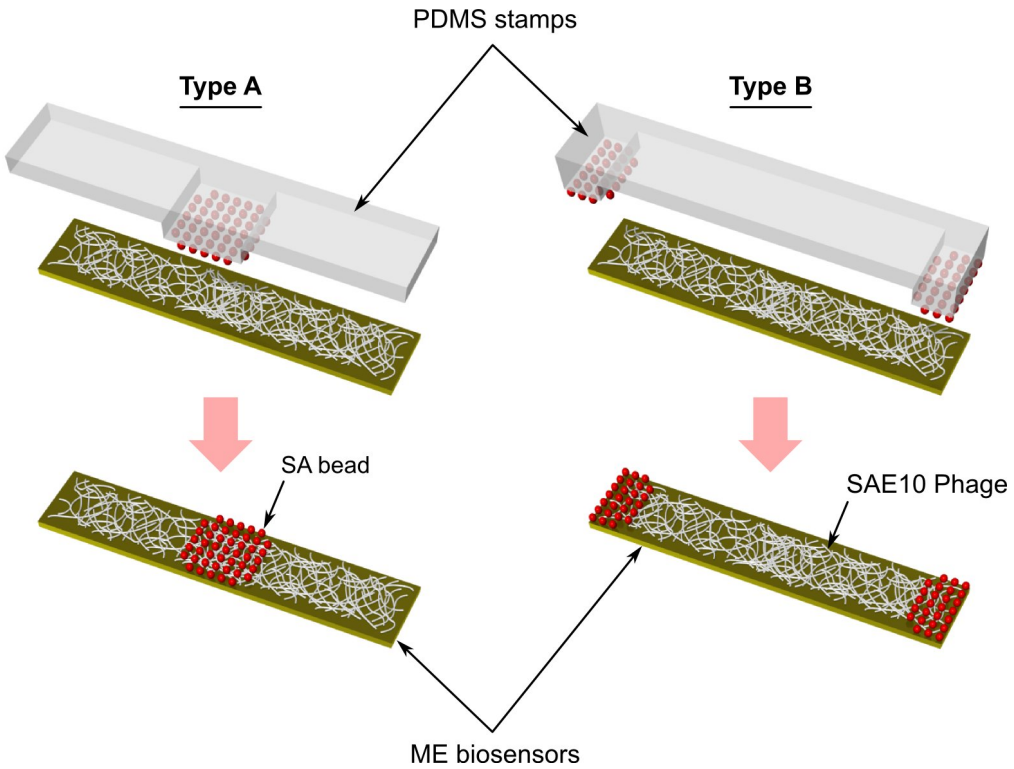

Figure 6.1: PDMS stamps and microcontact printing. SA beads (not to scale) were placed in the middle (stamping area: 1 mm × 0.8 mm) or (b) at both ends (stamping area: 0.5 mm × 0.8 mm each) of a phage-immobilized ME biosensor using the Type A or Type B stamp, respectively. BSA is not shown.

6.1. Two types of printing stamps, made of PDMS (from Momentive Performance Materials, Inc.), were fabricated by soft lithography and used. The Type A stamp places SA beads in the middle of a sensor (1 mm $\times$ 0.8 mm), whereas the type B stamp locates SA beads at both ends of a sensor (0.5 mm $\times$ 0.8 mm). The total stamping areas were kept the same for both types such that equivalent total masses could be placed at different locations on the sensor surfaces. A suspension of SA beads (3.6×10^{10} beads/ml) was pipetted onto the islands of the PDMS stamps. In this way, the beads were transferred to the surfaces of the ME biosensors. This procedure was followed by washing with filtered DI water three times to remove unbound and loosely bound SA beads.

Resonant frequency measurements of the ME biosensors were performed in air with the setup described in Chapter 3. The fundamental resonant frequency of longitudinal vibration was measured in this investigation.

6.1.3 Results and discussion

Figure 6.2 shows scanning electron micrographs of the phage-immobilized ME biosensors (4 mm $\times$ 0.8 mm, top view) loaded with SA beads. As a reference, an ME biosensor with uniform coverage of beads is also shown (Fig. 6.2c). The brightly colored regions on the sensors are where the SA beads are loaded. The average surface bead coverage in these regions was found to be 51.9%. As shown in Table 6.1, nonequivalent resonant frequency changes were experimentally obtained for the ME biosensors with localized bead masses at different positions (middle vs. ends). The mass sensitivity was low when the mass was loaded in the middle of the ME biosensors. By contrast, a higher mass sensitivity was obtained for the placement of the mass at both ends of the sensors. These results are reasonable because the nodal point (i.e., the point with zero displacement) is located in the middle of the biosensors for the fundamental mode of longitudinal vibration [2].

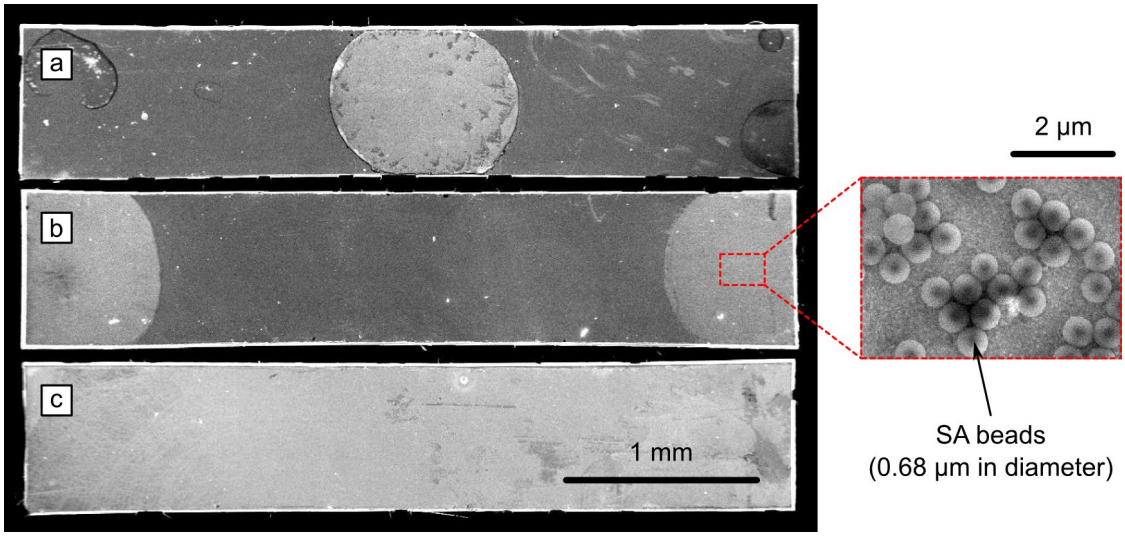

Figure 6.2: Phage-based ME biosensors loaded with SA beads. Beads are attached (a) in the middle, (b) at both ends, or (c) uniformly on both sides of the ME biosensors.

Table 6.1: Resonant frequency changes in Hz.

Mass position	**Experimental result**	**Numerical result**
Middle	-33 ± 17	-10
Ends	-212 ± 48	-179
Uniform[1]	-797 ± 52	-755

[1] Beads are attached to the back side as well.

6.1.3.1 Finite element modal simulation

Three-dimensional finite element (FE) analysis was performed to simulate the above phenomena (CalculiX, ver. 2.5, Convergent Mechanical Solutions, Seattle, WA). Convergence tests were conducted for all FE models, prior to eigenfrequency analysis, to ensure the element sizes that were chosen were fine enough to simulate the ME biosensor (i.e., quadratic brick elements with a size of 30 to 50 μm). In this work, the SA beads attached to the sensor surfaces were modeled as an orthotropic film mass (0.68-μm thick) as shown in Fig. 6.3a. Because of the discontinuities among the SA beads in reality, the materials constants for the film mass were given accordingly as summarized in Table 6.2. For simplification, flat rectangular films (1 mm × 0.8 mm in the middle and 0.5 mm × 0.8 mm at both ends) were modeled. The

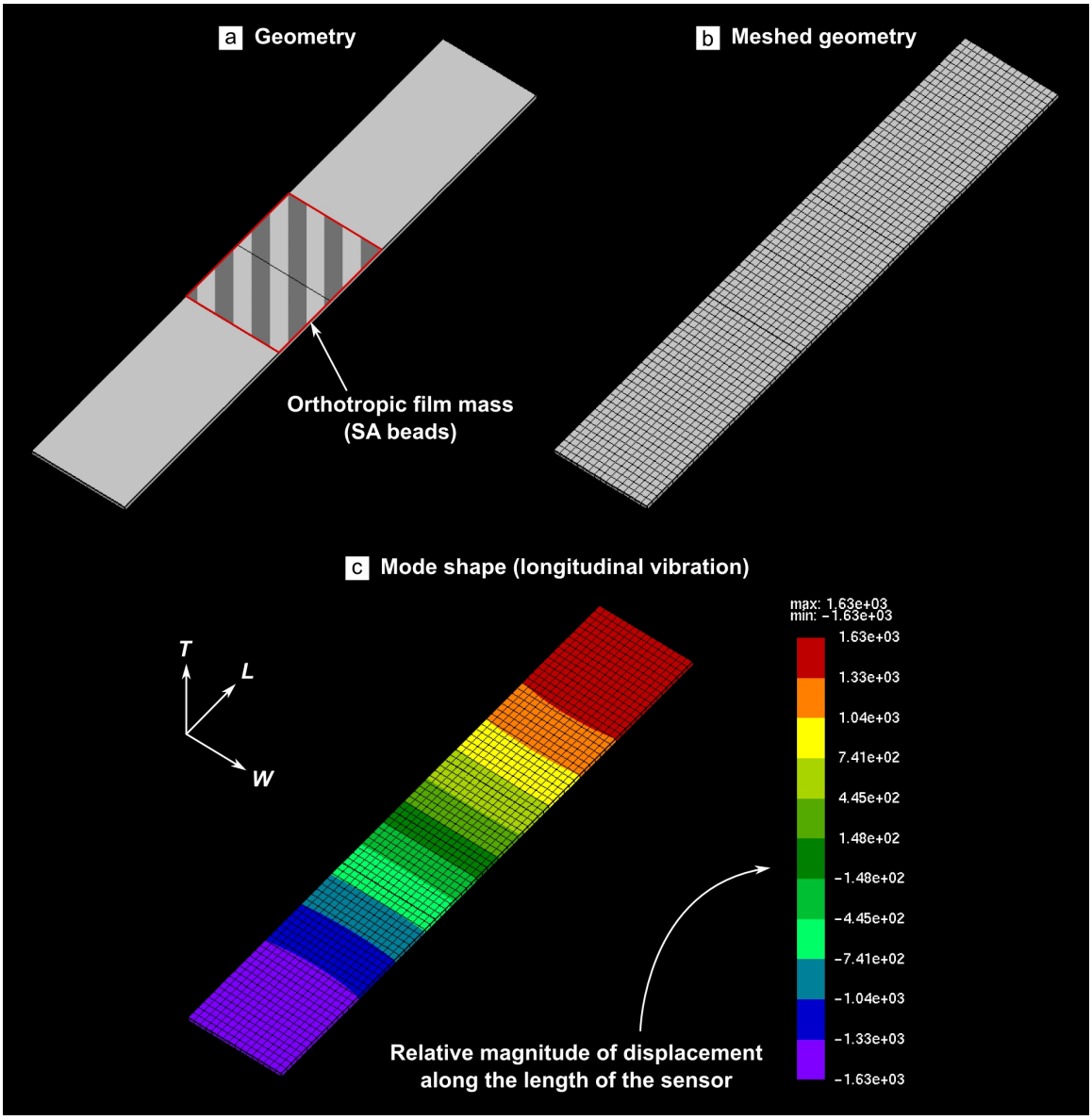

Figure 6.3: Three-dimensional FE model: (a) geometry, (b) meshed geometry, and (c) resultant mode shape.

metal deposits [3] (90-nm thick Cr and 150-nm thick Au) and phage layer ($\sim$ 10 nm) on the ME biosensor platforms were neglected because of their small effects on the sensors' resonant frequencies. As shown in Table 6.1, the simulation results showed close agreement with the experimental results.

After this validation of the FE method, similar FE models were constructed and used to predict the mass sensitivity of phage-immobilized ME biosensors loaded with

Table 6.2: Materials constants used in FE simulations[a].

Part	[GPa] E	[GPa] $E_L = E_W$	[GPa] E_T	[GPa] $G_{LW=WT=TL}$	[g/cm^3] ρ	ν	$\nu_{LW=WT=TL}$
Beads[b]	—	10^{-5}	1.56	10^{-5}	0.54	—	0
Bacteria[c]	0.025	—	—	—	1.05	0.499	—
Sensor[d] (Metglas)	105	—	—	—	7.9	0.33	—
Sensor[e] ($Fe_{80}B_{20}$)	166	—	—	—	7.4	0.3	—

[a] E, G, ρ, and ν denote the elastic modulus, shear modulus, density, and Poisson's ratio, respectively. The subscripts L, W, and T represent the axes along the length, width, and thickness of the ME biosensor.

[b] E_T was estimated by the rule of mixture from the surface bead coverage (51.9%) and a rough elastic modulus of a polystyrene bead (3 GPa [5]). ρ was calculated from both the surface bead coverage and density of a polystyrene bead (1.05 g/cm^3 from Spherotech, Inc.) to keep the mass of the film equivalent to that of the SA beads attached to the ME biosensors.

[c] E from [6] and ρ from [7]. Due to the high water content in a bacterial cell, $\nu \approx 0.5$ was used.

[d] Values obtained from Ref. [4].

[e] Values previously shown in Table 3.4.

a single bacterial mass. To investigate the effects of the sensor's dimensions on the mass sensitivity, FE models with varying lengths (100 – 500 μm), widths (lateral aspect ratios of 5 – 100), and thicknesses (1 – 15 μm) were built. The bacterial mass, treated as an isotropic mass (Table 6.2), was placed in the middle of the width and at different longitudinal positions of the ME biosensors (the effect of the mass position along the width was small). The dimensions of the mass were chosen to be 2 μm $\times$ 0.4 μm $\times$ 0.4 μm, which is of typical of the bacteria *Listeria* [6].

Figure 6.4 shows representative results of the dependence of mass sensitivity, $\Delta f/\Delta m$, on the longitudinal position of the attached mass and dimensions of ME biosensors. Similar to the results presented above, the mass sensitivity was largely dependent on the longitudinal mass position. Symmetric double-sigmoidal curves were found to show the best fit to the simulation data points (Fig. 6.4a). It was also

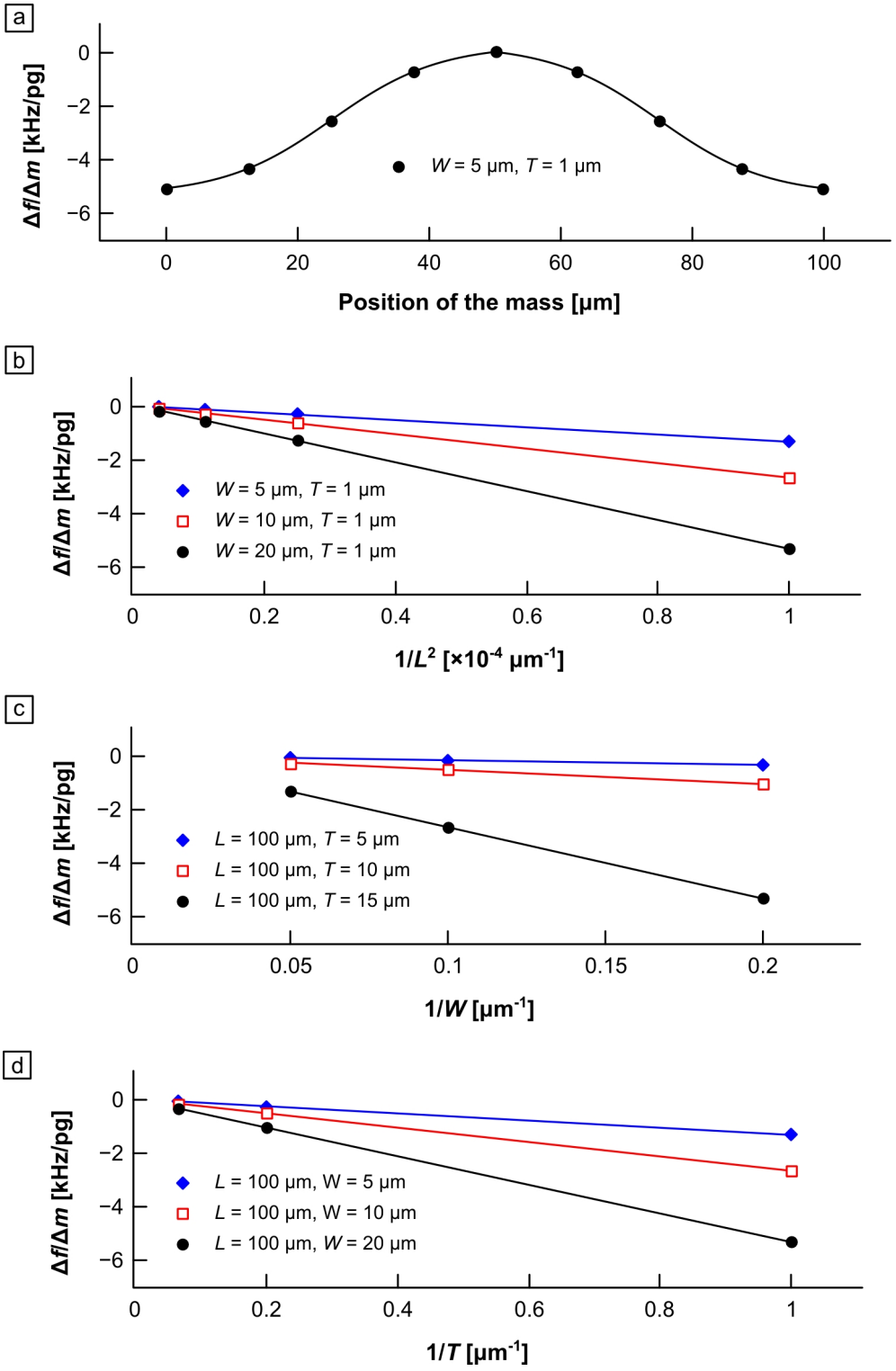

Figure 6.4: Dependence of the mass sensitivity, $\Delta f/\Delta m$, on the longitudinal position of the attached mass and on the dimensions of the ME biosensors.

found that the mass sensitivity is inversely proportional to L^2, W, and T as shown in Figs. 6.4b – 6.4d, where L, W, and T denote the length, width, and thickness of the ME biosensors, respectively.

From the FE simulation results, the mass sensitivity of a phage-immobilized ME biosensor loaded with a single bacterium was derived to be

$$\frac{\Delta f}{\Delta m}[\text{Hz/pg}] \approx -\frac{1}{L^2WT}\left[\frac{2.805\times10^8}{1+\exp\left(\frac{L'-L/4}{-0.082L-0.239}\right)}-1.310\times10^7\right], \tag{6.1}$$

where Δf, Δm, and L' denote the resonant frequency change, mass of the attached bacterium, and longitudinal distance of the attached bacterium from the center of the ME biosensor, respectively. Equation (6.1) describes a Boltzmann function whose amplitude is influenced by the dimensional variables, L, W, and T (the unit is μm). Hence, this equation allows one to estimate the mass sensitivity and, thus, resonant frequency change of differently sized ME biosensors upon the attachment of a single bacterium (Δm here is 2 μm $\times$ 0.4 μm $\times$ 0.4 μm $\times$ 1.05 g/cm^3 = 0.336 pg).

In summary, the mass sensitivity of ME biosensors is largely dependent on the longitudinal mass position and dimensions of the sensors. The equation derived in this investigation can be used to predict the mass sensitivity and resonant frequency change of differently sized ME biosensors for the detection of single pathogenic bacteria.

6.2 Effects of surface functionalization on surface phage coverage

Traditionally, phage-based ME biosensors have been constructed by immobilizing a landscape phage on gold-coated ME resonators via physical adsorption. Although the physical adsorption method is simple, the immobilization stability and surface coverage of a phage on differently functionalized sensor surfaces need to be evaluated as a potential way to enhance the detection capabilities of the biosensors.

6.2.1 Introduction

The phage display technology, primarily developed for the Ff class of filamentous phages [8,9], enables one to construct billions of phage clones that display engineered sequences of peptides on their outer surfaces. Today, such phage clones are called landscape phages, and they are being used in a variety of applications due to their diversity, low cost, ease of production, and environmental robustness [10, 11]. In bacterial detection, for instance, a number of attempts have been recently made to employ landscape phages as biomolecular recognition elements, which substitute for commonly used antibodies.

A biomolecular recognition element is a key component of a biosensor used to specifically target and bind a pathogen of interest to the signal transducer [12]. Hence, in phage-based biosensing systems, robust and efficient immobilization of a phage has been one of the spotlighted issues. Widely used immobilization methods include physical adsorption, biotin – avidin coupling, and covalent attachment through a self-assembled monolayer (SAM). Among these methods, physical adsorption is the simplest method, and it has been traditionally used to construct our phage-based ME biosensors. However, the immobilization stability and quantity of physically adsorbed phages may be lower than those of biotin – avidin coupled and covalently bound phages because of the weak, non-specific bonding of physical adsorption. Recently, a covalent immobilization of a landscape phage has been reported [13]. A SAM of

N-hydroxysuccinimide thioctic ester was used to covalently bind M13 phage onto a gold-coated quartz-crystal microbalance. The immobilization chemistry yielded a surface phage density of 1.1×10^{11} virions/cm^2, which is 70% higher than the highest reported surface density of a physically adsorbed fd-tet phage [14]. In addition, a study of chemical immobilization of T4 phage on gold surfaces has shown that phage immobilization through glutaraldehyde-activated cysteine/cysteamine produced a 37-fold increase in surface phage density and a 9-fold increase in the surface density of subsequently captured *E. coli* host cells, compared to those with physical phage adsorption [15]. Hence, these pieces of recent research have indicated that surface functionalization may affect the stability and quantity of immobilized phages.

The primary objectives of this work are: (1) to investigate the effects of surface functionalization on the surface coverage of a filamentous fd-tet phage and (2) to find the correlation between the observed surface phage coverage and the quantity of a subsequently captured target analyte. As a model study, an fd-tet phage that specifically binds with streptavidin (the SAE10 phage in Table 3.3) was adsorbed on gold-coated ME resonators with a size of 1 mm $\times$ 0.2 mm $\times$ 15 μm. The surfaces of the resonators were either bare or functionalized with three different SAMs as shown in Fig. 6.5: (a) AC (activated carboxyl-terminated SAM: 1-[5-(1,2-dithiolan-3-yl)pentanoyl]oxypyrrolidine-2,5-dione); (b) ALD (aldehyde-terminated SAM: *N*-[19-(1,2-dithiolan-3-yl)-15-oxo-4,7,10-trioxa-14-azanonadec-1-yl]-4-formylbenzamide); and (c) MT (methyl-terminated SAM: hexanethiol). Surface functionalization with these SAMs was based on the sulfur - gold chemistry, which was verified by contact angle goniometry and X-ray photoelectron spectroscopy (XPS). Atomic force microscopy (AFM) was used to quantify surface phage coverage and to visualize the distribution of the filamentous phage on the ME resonator surfaces. In addition, dose-responses of the phage-immobilized ME biosensors to streptavidin-coated microbeads were obtained through resonant frequency measurements.

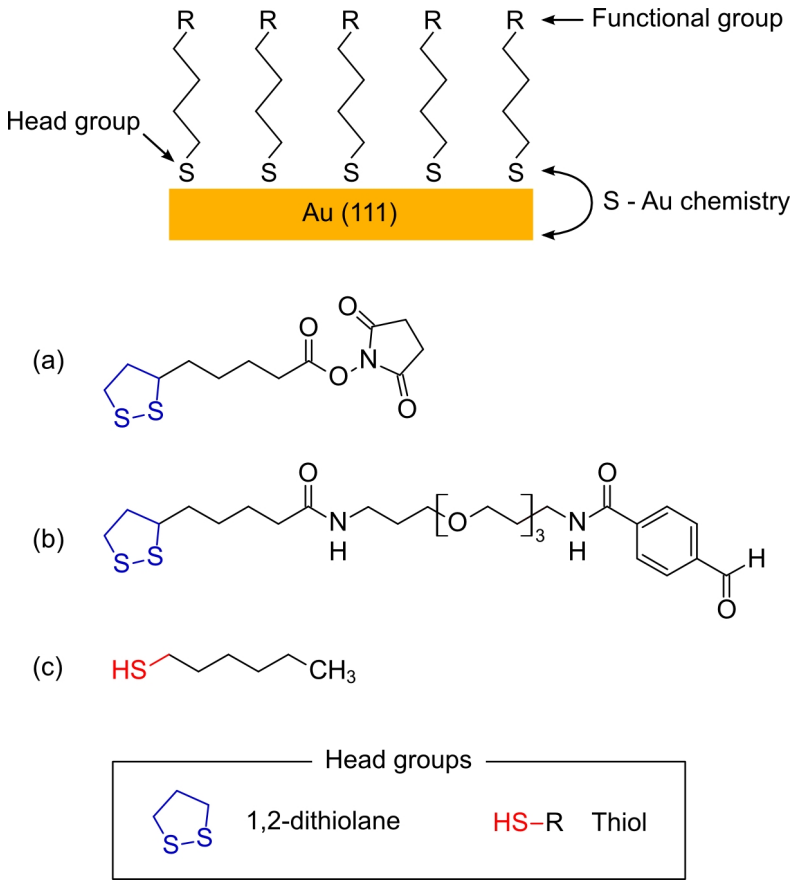

Figure 6.5: Surface functionalization of gold (1 1 1) with three SAM chemicals, based on the sulfur - gold chemistry: (a) AC (activated carboxyl-terminated), (b) ALD (aldehyde-terminated), and (c) MT (methyl-terminated).

6.2.2 Material and methods

All chemical and biological reagents were purchased from Fisher Scientific (Pittsburgh, PA, USA), Sigma-Aldrich (St.Louis, MO, USA), or SoluLinK (San Diego, CA, USA) and used as-received unless otherwise noted. Filtered deionized (DI) water (pH 7.4) was prepared with SimPak 1 Purification Pack Kit (Millipore, Billerica, MA, USA) and used for solution making and sample washing. A HEPES buffer (100-mM, pH 7.3) was prepared and filtered with Stericup filter units (Millipore, Billerica, MA, USA) prior to use.

6.2.2.1 Preparation of biological samples

The SAE10 phage, which specifically binds with streptavidin [16], was prepared in a 100 mM HEPES buffer (6.5×10^{11} virions/ml, pH 7.3). Streptavidin-coated polystyrene microbeads (hereafter, SA beads, 0.68 ± 0.11 μm in diameter (measured), 3.6×10^{10} beads/ml) were purchased from Spherotech, Inc. (Lake Forest, IL, USA), transferred to a 100-mM HEPES buffer (pH 7.3) by centrifugation, and used for dose-response experiments of ME biosensors. Serial dilutions of the bead suspension were also prepared with a 100-mM HEPES buffer (pH 7.3).

6.2.2.2 Manufacture of gold-coated ME resonators

ME resonators with a size of 1 mm $\times$ 0.2 mm $\times$ 15 μm were manufactured with the dicing-based procedure described in Chapter 3. After annealing, chromium (90-nm thick) and gold (150-nm thick) were successively deposited on all the resonator surfaces by sputtering at 2.5×10^{-6} Torr (Denton Vacuum, Moorestown, NJ, USA). The predominant crystallographic orientation of the gold deposit was (111), verified by x-ray diffraction analysis (D/MAX-B, Rigaku, Inc., Danvers, MA, USA). The outer-coat gold deposit protects ME resonators from corrosion as well as provides suitable surfaces for surface functionalization (i.e., sulfur – gold chemistry-based) and immobilization of the phage.

6.2.2.3 Surface functionalization of gold-coated ME resonators

Surface functionalization, based on the sulfur – gold chemistry [17], was performed. The three SAM chemicals, AC, ALD, and MT, possess either 1,2-dithiolane ($C_3H_6S_2$) or a thiol group (–SH) in their structures as the head group (Figure 6.5). AC and ALD were individually dissolved (16.5 mM each) in dry dimethylformamide (DMF, 99.8% pure), whereas MT was dissolved (1 mM) in dry ethanol ($\geq$ 99.5% pure). Freshly prepared gold-coated ME resonators were immersed in each of the

SAM chemical solutions for 36 hours at 23°C in a desiccator, protected from UV exposure. The surface-functionalized ME resonators were, then, washed with dry DMF once and dry ethanol twice (The MT-functionalized ME resonators were washed with dry ethanol three times.). After drying with high quality argon gas ($\geq$ 99.999% pure, Airgas South, Kennesaw, GA, USA), the surface-functionalized ME resonators were stored in a desiccator, protected from UV exposure, until used.

6.2.2.4 X-ray photoelectron spectroscopy

Photoemission measurements were performed for bare and SAM-modified gold surfaces in a load-locked Kratos XSAM 800 surface analysis system (Kratos Analytical Inc., New York, USA). The base pressure of the system was 1×10^{-10} torr. XPS spectra were recorded in the fixed analyzer transmission (FAT) mode with a pass energy of 20 eV, appropriate for acquisition of high resolution, high signal-to-noise spectra. The magnification of the analyzer in the FAT mode was selected to collect electrons from the smallest allowable area (5 mm^2) on the specimen. The resolution of the instrument at the operating parameters was measured from the full-width-at-half-maximum of the $Ag3d_{5/2}$ peak to be 1.0 eV. The XPS energy scale was calibrated by setting the $Ag3d_{5/2}$ line on clean silver to exactly 368.3 eV referenced to the Fermi level. Because of specimen charging during x-ray irradiation of the organic specimens, the energy axis of each XPS spectra was shifted to make the C1s binding energy line equal to 284.7 eV, a standard hydrocarbon energy (C-H and C-C bonds) used to reference charge-affected materials. The uncertainty of the binding energies recorded was 0.1 eV. The photoelectrons were excited by a water-cooled Kratos Model WG-170 dual anode x-ray gun equipped with an aluminum window. The angle of the incidence of the x-ray beam with the specimen normal was 51.5°. Unmonochromatized Mg$K\alpha$ (1253.6 eV) radiation was used exclusively. The x-ray power was kept relatively low

(260W, 13 kV at 20 mA) so as to minimize sample heating. Raw XPS spectra were curve-fitted by the Savitzky-Golay method (10-point, second-order fitting).

6.2.2.5 Loading of the phage on the ME resonators

The prepared ME resonators were individually immersed in 330 μL of the phage suspension in a polypropylene PCR tube. The tubes were, then, rotated with a Barnstead LabQuake tube rotator (from Fisher Scientific, Inc.) at 8 rpm for 1 h, protected from UV exposure. In this way, the phage was allowed to uniformly attach to resonator surfaces via either physical adsorption or covalent attachment. After loading the phage, these resonators were washed thoroughly to remove any HEPES buffer component as well as loosely attached phages from the resonator surfaces. The surface-functionalized ME resonators loaded with phage were washed with a wash buffer (Tween 20 in a 100-mM HEPES buffer (0.5% v/v, pH 7.3)) three times, whereas the bare ME resonators loaded with phage were washed with DI water three times, following the traditional way of sensor preparation described in Chapter 3. Finally, all the phage-loaded resonators were surface-blocked with BSA (0.1% w/v in a 100-mM HEPES buffer), followed by washing with filtered DI water three times. Samples for AFM imaging were not BSA blocked.

6.2.2.6 Resonant frequency measurement

Resonant frequency measurements of ME biosensors were performed with the setup described in Chapter 3. For dose-response experiments, a phage-immobilized ME biosensor placed in the center of the solenoid coil was exposed to a suspension of SA beads with various concentrations (3.6×10^5 to 3.6×10^{10} beads/ml in 100-mM HEPES) at a flow rate of 25 μl/min (Ismatec CP 78017-10, Cole-Parmer Instrument Company, Vernon Hills, IL, USA) as shown in Figure 6.6. The resonant frequency of the ME biosensors was recorded every 15 seconds with a resolution of 25 Hz. In

addition, BSA-blocked ME biosensors (without phage) were tested as controls. A 100-mM HEPES buffer was flowed before and after the bead exposure to eliminate any viscosity effects on the resonant frequency change and to remove unbound and loosely bound SA beads from the biosensor surfaces. UV exposure during measurements was minimized by covering the solenoid coil with an opaque plastic box. Selective capture of SA beads on the phage-immobilized ME biosensors was verified by scanning electron microscopy (SEM) (JSM-7000F, JOEL, Ltd., Tokyo, Japan).

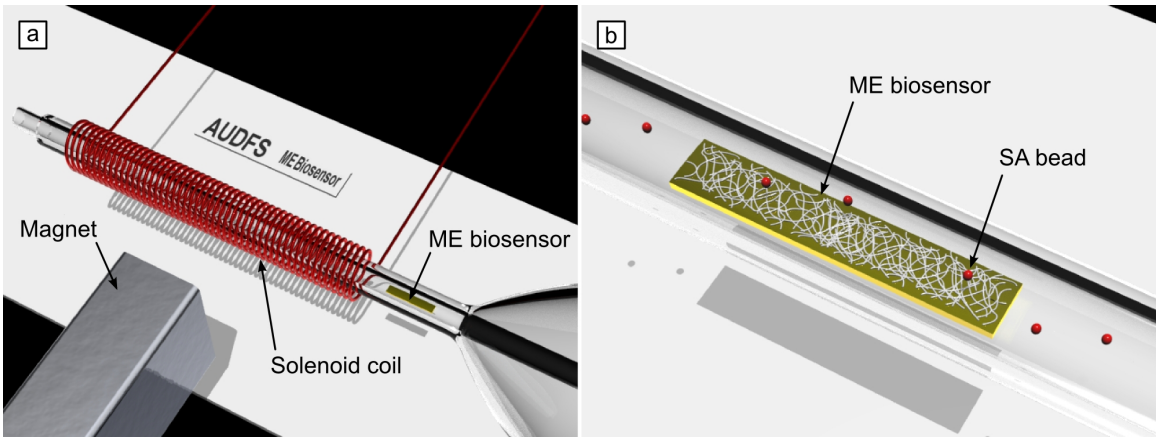

Figure 6.6: Schematic illustration of the frequency measurement setup for ME biosensors. (a) The setup consists of a copper solenoid coil, a bar magnet, and a network analyzer (not shown). (b) A phage-immobilized ME biosensor is placed in the glass capillary flow cell and positioned in the coil center. A suspension of SA beads was passed at 25 μl/min over the sensor, and the resonant frequency change of the biosensor was monitored in a wireless, magnetic manner.

6.2.3 Results and discussion

6.2.3.1 Verification of the surface functionalization of gold

The surface functionalization of gold was verified by contact angle goniometry (Model 200, Ramê-Har, Inc., Mountain Lakes, NJ, USA) and XPS (Kratos XSAM 800, Kratos Analytical, Inc., New York, NY, USA). Since the gold-coated ME resonators (1 mm $\times$ 0.2 mm) were too small for these analyses, gold surface specimens

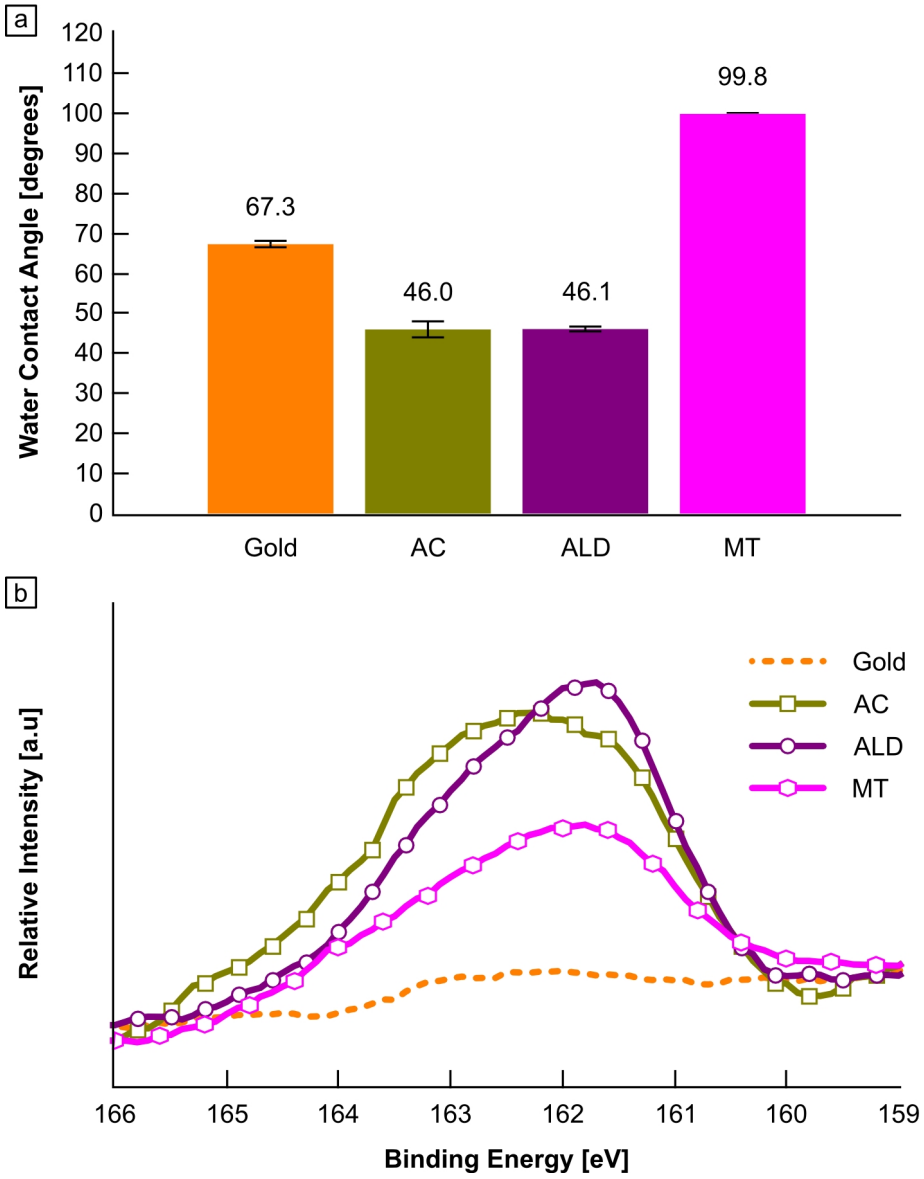

Figure 6.7: (a) Water contact angles for bare and surface-functionalized gold surfaces. (b) XPS S2p peaks at around 162 eV, indicating the formation of sulfur – gold bonded systems.

were, instead, prepared on polished silicon wafer pieces (1 cm × 1 cm), surface-functionalized in the same ways described earlier, and tested. As shown in Figure 6.7a, the water contact angle varied as a result of the surface functionalization (measured at 23°C and 31% relative humidity with water drops of pH 7.8). The polar activated carboxyl- and aldehyde-terminated surfaces (AC- and ALD-functionalized surfaces) showed lower contact angles than the reference gold surface, whereas the

non-polar methyl-terminated surface (MT-functionalized surface) showed a dramatic increase in contact angle. XPS analysis was also performed to confirm the contact angle results. As shown in Figure 6.7b, the S2p peaks for the surface-functionalized gold surfaces were close to the expected binding energy ($\approx$ 162 eV) in a sulfur – gold bonded system [18]. In other words, the gold surfaces were properly functionalized with the SAM chemicals, based on the sulfur – gold chemistry.

6.2.3.2 Surface phage coverage

After the loading of the phage on both bare and surface-functionalized ME resonators, the surface phage coverage was measured by AFM. The AFM imaging was performed at 23°C and 30% relative humidity using a scanning probe microscope (Dimension 3100, Veeco Instrument, Inc., Santa Barbara, CA, USA), operated in the tapping mode. Silicon probes with a tip radius of curvature of < 8 nm (FM probes, NanoWorld AG, Neuchâtel, Switzerland) were used to image 2 μm $\times$ 2 μm areas at a resolution of 256 $\times$ 256 pixels.

As shown in Figs. 6.8b to 6.8e, the phage was present on the ME resonator surfaces in the form of phage bundles (49.3 $\pm$ 4.8 nm in lateral thickness) and can be distinguished from the background gold deposit, based on the height profiles (Figure 6.8a is of the reference gold surface). The surface phage coverage was calculated from the surface areas occupied by the phage to be 46.8%, 49.4%, 4.2%, and 5.2% for (b) bare, (c) AC-, (d) ALD-, and (e) MT-functionalized ME resonators, respectively (Fig. 6.8f). As anticipated, relatively high surface phage coverage was obtained for the bare gold-coated ME resonator, which is attributed to the physical adsorption of the phage. In addition, comparable surface phage coverage was obtained for the AC-functionalized ME resonator. At a pH of above 7, the *N*-hydroxysuccinimide of the chemical AC leaves the group. The resultant activated carboxyl group, thus, forms a covalent amide bond with the *N*-terminus of a phage coat protein [13,19]. Even after

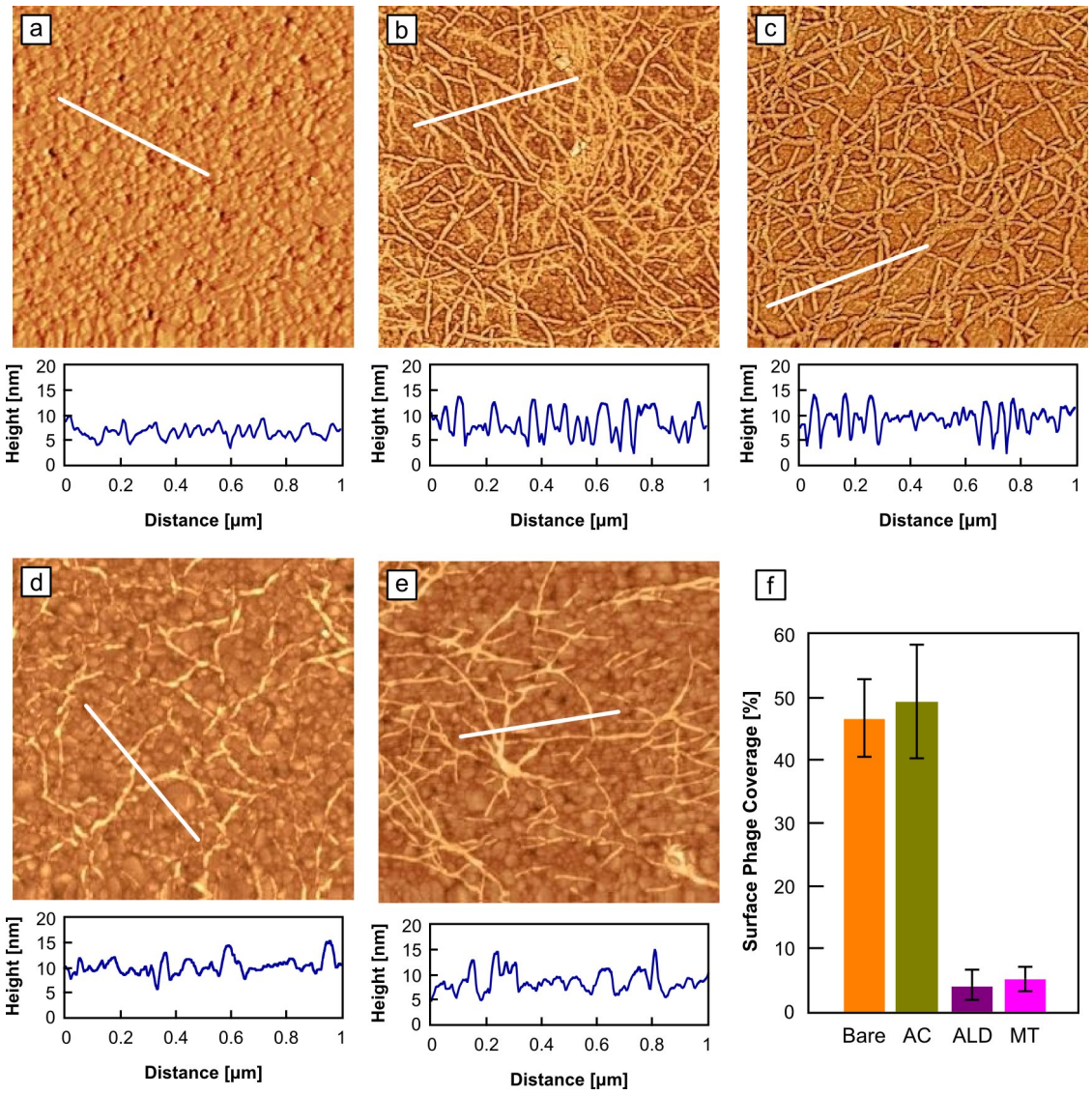

Figure 6.8: AFM images (2 μm $\times$ 2 μm) of the SAE10 phage on bare and surface-functionalized ME resonators: (a) reference, (b) bare gold (physical phage adsorption), (c) AC- (covalent phage attachment), (d) ALD-, and (e) MT-functionalized ME resonators. The white lines on the photographs were the paths from which the height profiles were measured. (f) The surface phage coverage values were 46.8%, 49.4%, 4.2%, and 5.2% for bare, AC-, ALD-, and MT-functionalized ME resonators, respectively.

washing with the wash buffer containing Tween 20, a commonly used detergent for blocking and cleaning of non-specifically adsorbed proteins [20], the covalently bound phages were found to be immobilized robustly on the resonator. In this work, a significant improvement in surface phage coverage was not observed for the AC-based

covalent phage immobilization, compared to the physical phage adsorption. Possible reasons are: (1) similar space-filling mechanisms of both physically and covalently adsorbed phages (i.e., the filamentous phage probe lay on the ME resonator surfaces upon adsorption) and (2) the effects of washing with/without the Tween 20 detergent on the quantity of the immobilized phages. In both cases, the major coat protein pVIII ($\sim$ 4,000 copies) seemed to provide the largest contribution in adsorption and immobilization stability. To investigate the effects of washing with the Tween 20 detergent, both physcially and covalently adsorbed phages on bare or AC-functionalized gold surfaces (1 cm $\times$ 1 cm) were washed with a 100-mM HEPES buffer containing various concentrations of Tween 20 (0 to 5% v/v) and finally with DI water. Contact angle changes due to the washing were, then, measured for these surfaces. The effect of washing was found to be large on the immobilization stability of the physically adsorbed phages. At a Tween 20 concentration of over 0.5% v/v, dramatic changes in water contact angle were observed for the gold surfaces with physically adsorbed phages, whereas much small contact angle changes occurred for those with covalently bound phages (Fig. 6.9). By contrast, a much smaller phage coverage was obtained for ALD- and MT-functionalized ME resonators (Figs. 6.8d and 6.8e). The surface phage coverage values were one order of magnitude smaller than those for the bare and AC-functionalized ME resonators (Figs. 6.8b and 6.8c). The coupling of the aldehyde-terminated SAM (ALD) and the *N*-terminus of a coat protein of the SAE10 phage seemed not to occur extensively under the buffer condition used in this work (100-mM HEPES, pH 7.3). Although Peelen and Smith has reported that an imine and a carbonyl can co-exist for an aldehyde – amine coupling reaction in aqueous buffer, the reactivity depends on the pH and buffer compositions [21]. In fact, the best condition for their model system was 10-mM HEPES mixed with 60-mM $NaBH_3CN$ at pH 10, which produced a stable secondary amine product. Washing of the ME

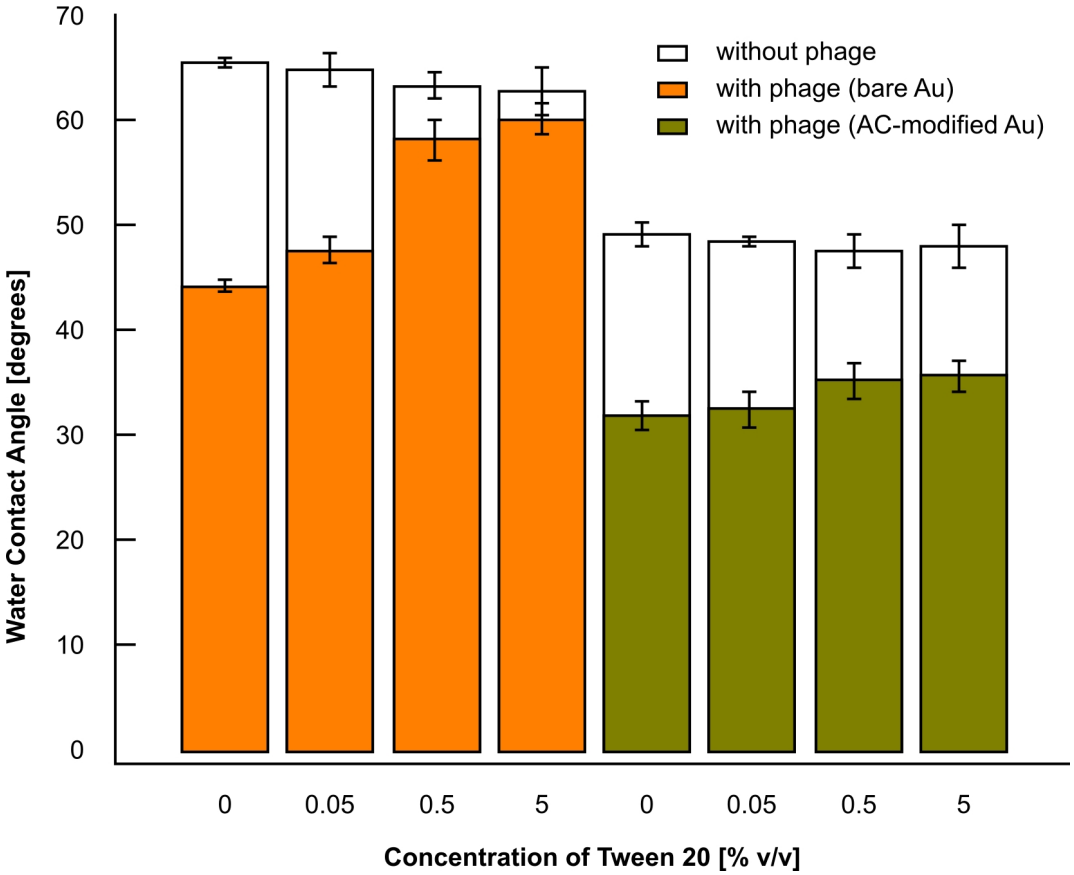

Figure 6.9: Water contact angles for bare and AC-functionalized gold surfaces loaded with/without phages. The surfaces were washed with a 100-mM HEPES buffer containing various concentrations of Tween 20 (0 to 5 % v/v) and finally with DI water. The effect of washing was found to be large on the immobilization stability of the physically adsorbed phages.

resonators with DI water after the phage loading was found to cause the imine product to be excessively hydrolyzed. Furthermore, the aldehyde- and methyl-terminated SAMs also have been found to block cystein-based covalent phage attachment [14] to gold-coated ME resonator surfaces. Hence, the ALD and MT-functionalized surfaces can be described as "anti-phage surfaces" under proper buffer and sample preparation conditions.

6.2.3.3 SEM observation and dose-response results

Figures 6.10a to 6.10d show SEM images for phage-immobilized ME biosensors ((a) bare, (b) AC-, (c) ALD-, and (d) MT-functionalized ME biosensors, all BSA-blocked) exposed to an SA bead suspension (3.6×10^{10} beads/ml), followed by washing with filtered DI water three times. The surface bead coverage for the bare and AC-functionalized ME biosensors was much higher than that for the ALD- and MT-functionalized ME biosensors, which can be explained by the large differences in surface phage coverage (See Figure 6.8.). Although the adsorption of the SAE10 phage onto the sensor surface is random in nature, approximately 4,000 copies of the binding sites along the length of the phage massively bound with SA beads (as high as 1.42 ± 0.26 beads/μm^2). This large number of binding sites is one of the advantages of filamentous landscape phages. In addition, non-specific adsorption of SA beads was greatly prevented by BSA as can be seen in Figs. 6.10e and 6.10f.

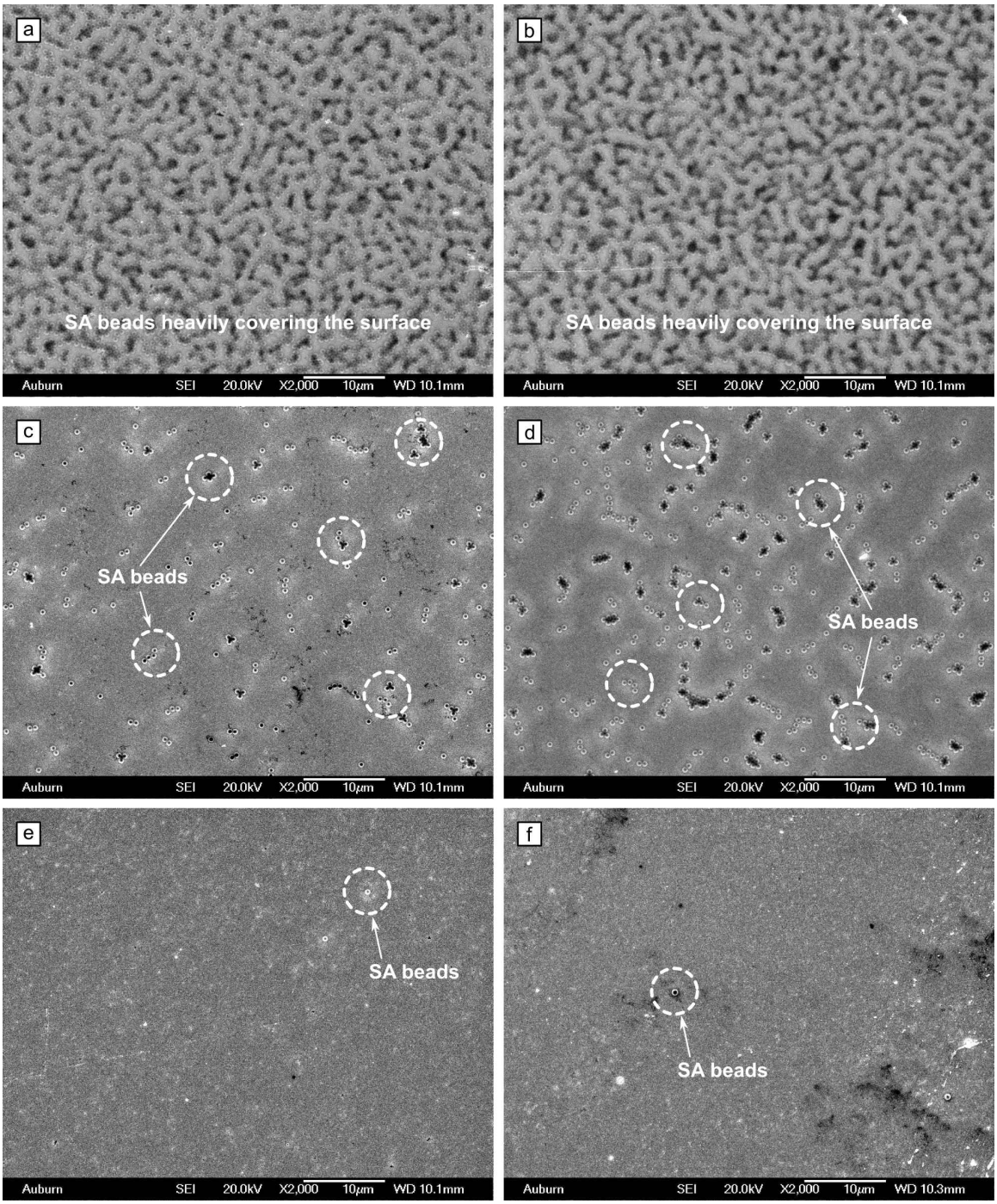

Figure 6.10: SEM images showing SA beads captured by the SAE10 phage on bare and surface-functionalized ME biosensors (all BSA blocked): (a) bare, (b) AC-, (c) ALD-, and (d) MT-functionalized ME biosensors. Non-specific adsorption of SA beads was greatly reduced by BSA blocking: (e) bare and (f) AC-functionalized ME biosensors without phage.

Based on the SEM observation results, dose-response plots were constructed for only the bare and AC-functionalized ME biosensors with high surface phage coverage ($\sim$ 50%) in order to compare their performance. The ME biosensors were exposed to various concentrations of SA bead suspensions (3.6×10^5 to 3.6×10^{10} beads/ml), and the resultant resonant frequency changes were plotted in Figs. 6.11a and 6.11b.

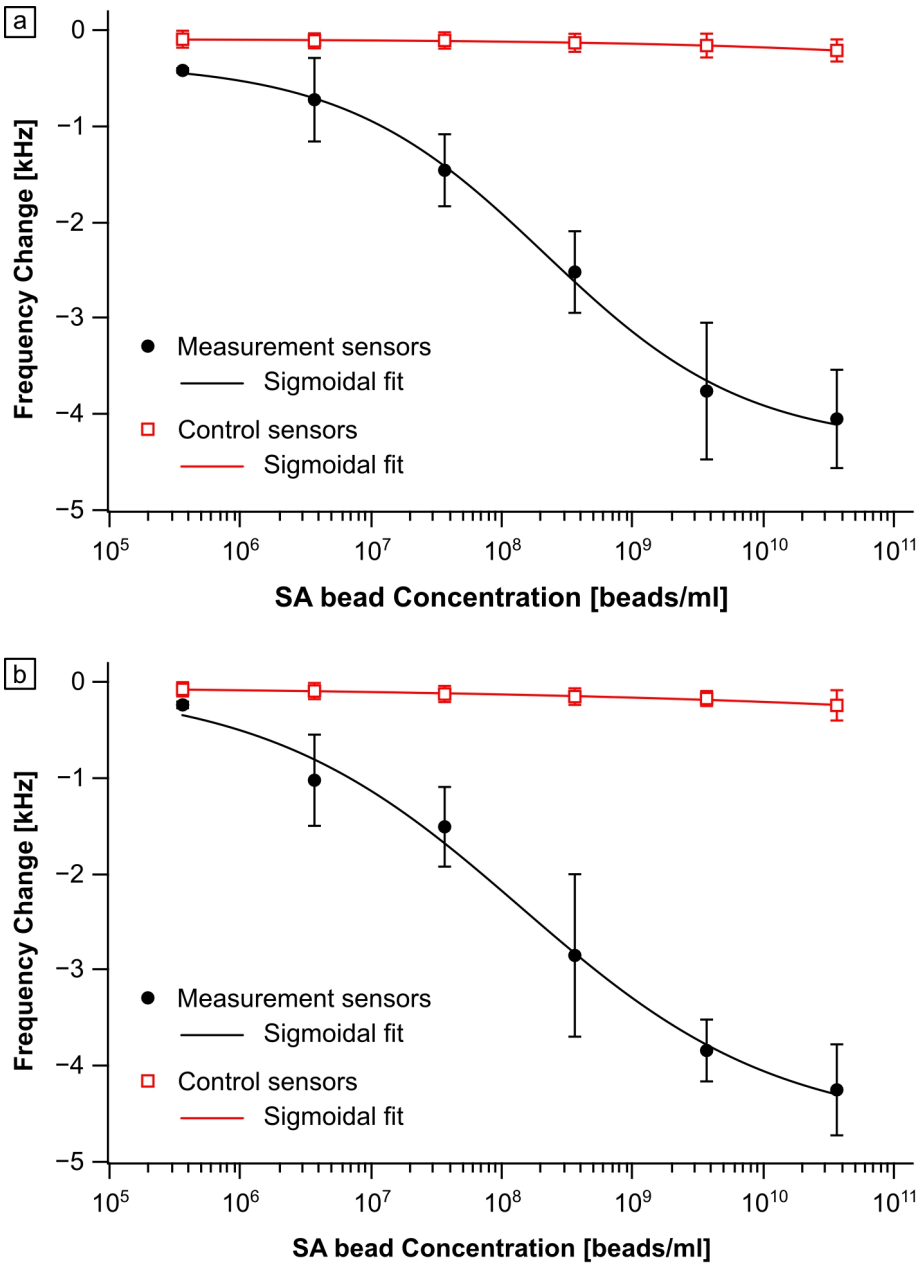

Figure 6.11: Dose-response plots showing the comparable performance of (a) bare and (b) AC-functionalized ME biosensors (1 mm $\times$ 0.2 mm $\times$ 15 μm).

The comparable performance of the bare and AC-functionalized ME biosensors (measurement sensors) indicates again that the surface phage coverage plays a crucial role in analyte capture. In addition, the measured negligible changes in control sensor resonant frequencies verified the prevention of non-specific adsorption of SA beads on the BSA-blocked ME biosensors.

6.2.3.4 Enhancing the detection capabilities of ME biosensors with a patterned phage layer

One of the ultimate goals to be reached for phage-immobilized ME biosensors is the detection of single pathogenic bacteria. However, the mass sensitivity of freestanding, strip-shaped ME biosensors operating longitudinal-vibration modes is largely dependent on the position of masses attached to the sensor surfaces [2]. In fact, for non-uniform mass attachment, which may be caused by the absence of sufficient quantity of target analytes, the mass sensitivity cannot be described by Eq. 3.6 (i.e., This equation is valid only for uniform mass attachment). It has been recently reported that for fundamental resonant frequency measurements of ME sensors, 1) the mass sensitivity is close to zero when the mass is attached in the middle of the sensor's longest dimension and 2) a high mass sensitivity is, by contrast, obtained for the mass attached at both ends of the sensor [2]. Considering this dependence is crucial to detection of low-concentration bacterial targets, including single pathogenic bacteria, because their local attachment may cause varying sensor responses. In a worst-case scenario, the resultant changes in resonant frequency may be too small and undetectable despite the use of micron-scale ME biosensors (i.e., The mass sensitivity increases as the size of sensor is decreased.). Although measurements of higher-mode resonant frequencies may solve the above-mentioned problem [2], the amplitude of the higher-mode frequency peaks is generally too small to be detected for micron-scale ME sensors, particularly in a liquid environment. Hence, when fundamental resonant

frequency measurements are considered, the phage layer that specifically binds with target bacteria may need to be patterned onto desired parts of sensor surface to enhance detection capabilities. One potential way to achieve this goal is to properly functionalize the sensor surface to maximize or minimize the surface phage coverage. Therefore, the results presented in this chapter may be useful. Since various methods of SAM patterning (e.g., photobleaching and scanning probe-based lithography) are readily available [17], micron-scale ME biosensors interfaced with a patterned phage layer may enable the detection of single pathogenic bacteria in the future.

6.2.4 Conclusions

Surface phage coverage on bare and surface-functionalized ME biosensors was quantified by AFM. The activated carboxyl-based covalent attachment (AC-based covalent attachment) produced a phage coverage of $\sim 50\%$, comparable to that obtained through physical phage adsorption. The results can be attributed to the space-filling nature of the filamentous SAE10 phage upon adsorption and effects of washing with/without the Tween 20 detergent. By contrast, aldehyde- and methyl-terminated surfaces (ALD- and MT-functionalized surfaces) did not yield high phage coverage. These surface functionalization may be used to construct "anti-phage surfaces" under proper buffer and sample preparation conditions. In addition, the large differences in the quantity of the captured SA beads on the differently functionalized sensor surfaces as well as the comparable dose-response results of the bare and AC-functionalized ME biosensors indicated that the surface phage coverage is a key factor in analyte capture. The results obtained here should be applicable to other fd-tet phage-based biosensing systems. Finally, a phage probe layer can be patterned onto desired parts of the sensor surface to enhance detection capabilities by properly functionalizing sensor surfaces.

Bibliography

[1] C. A. Grimes, C. S. Mungle, K. Zeng, M. K. Jain, W. R. Dreschel, M. Paulose, and K. G. Ong, "Wireless magnetoelastic resonance sensors: A critical review," *Sensors*, vol. 2, pp. 294 – 313, 2002.

[2] S. Li and Z.-Y. Cheng, "Nonuniform mass detection using magnetostrictive biosensors operating under multiple harmonic resonance modes," *Journal of Applied Physics*, vol. 107, p. 114514, 2010.

[3] S. Huang, J. Hu, J. Wan, M. Johnson, H. Shu, and B. Chin, "The effect of annealing and gold deposition on the performance of magnetoelastic biosensors," *Materials Science and Engineering: C*, vol. 28, no. 3, pp. 380 – 386, 2008.

[4] C. Liang, S. Morshed, and B. C. Prorok, "Correction for longitudinal mode vibration in thin slender beams," *Applied Physics Letters*, vol. 90, p. 221912, 2007.

[5] U. Rai and R. Singh, "Synthesis and mechanical characterization of polymer-matrix composites containing calcium carbonate/white cement filler," *Materials Letters*, vol. 58, pp. 235 – 240, 2003.

[6] A. Gupta, D. Akin, and R. Bashir, "Detection of bacterial cells and antibodies using surface micromachined thin silicon cantilever resonators," *Journal of Vacuum Science & Technology B*, vol. 22, pp. 2785 – 2791, 2004.

[7] X. Yao, M. Jericho, D. Pink, and T. Beveridge, "Thickness and elasticity of gram-negative murein sacculi measured by atomic force microscopy," *Journal of Bacteriology*, vol. 181, pp. 6865 – 6875, 1999.

[8] V. A. Petrenko, G. P. Smith, X. Gong, and T. Quinn, "A library of organic landscapes on filamentous phage," *Protein Engneering*, vol. 9, pp. 797 – 801, 1996.

[9] G. P. Smith and V. A. Petrenko, "Phage display," *Chemical Reviews*, vol. 97, pp. 391 – 410, 1997.

[10] C. Mao, A. Liu, and B. Cao, "Virus-based chemical and biological sensing," *Angewandte Chemie International Edition*, vol. 48, pp. 6790 – 6810, 2009.

[11] V. A. Petrenko, "Landscape phage as a molecular recognition interface for detection devices," *Microelectronics Journal*, vol. 39, no. 2, pp. 202 – 207, 2008.

[12] O. Lazcka, F. J. D. Campo, and F. X. M. noz, "Pathogen detection: A perspective of traditional methods and biosensors," *Biosensors and Bioelectronics*, vol. 22, no. 7, pp. 1205 – 1217, 2007.

[13] L.-M. C. Yang, J. E. Diaz, T. M. McIntire, G. A. Weiss, and R. M. Penner, "Covalent virus layer for mass-based biosensing," *Analytical Chemistry*, vol. 80, pp. 933 – 943, 2008.

[14] E. V. Olsen, I. B. Sorokulova, V. A. Petrenko, I.-H. Chen, J. M. Barbaree, and V. J. Vodyanoy, "Affinity-selected filamentous bacteriophage as a probe for acoustic wave biodetectors of *Salmonella typhimurium*," *Biosensors and Bioelectronics*, vol. 21, pp. 1434 – 1442, 2006.

[15] A. Singh, N. Glass, M. Tolba, L. Brovko, M. Griffiths, and S. Evoy, "Immobilization of bacteriophages on gold surfaces for the specific capture of pathogens," *Biosensors and Bioelectronics*, vol. 24, pp. 3645 – 3651, 2009.

[16] G. Kuzmicheva, P. Jayanna, I. Sorokulova, and V. Petrenko, "Diversity and censoring of landscape phage libraries," *Protein Engineering, Design and Selection*, vol. 22, pp. 9 – 18, 2009.

[17] R. K. Smith, P. A. Lewis, and P. S. Weiss, "Patterning self-assembled monolayers," *Progress in Surface Science*, vol. 75, pp. 1 – 68, 2004.

[18] W. Fabianowski, L. C. Coyle, B. A. Weber, R. D. Granata, D. G. Castner, A. Sadownik, and S. L. Regen, "Spontaneous assembly of phosphatidylcholine monolayers via chemisorption onto gold," *Langmuir*, vol. 5, pp. 35 – 41, 1989.

[19] P. Wagner, M. Hegner, P. Kernen, F. Zaugg, and G. Semenza, "Covalent immobilization of native biomolecules onto Au(111) via N-hydroxysuccinimide ester functionalized self-assembled monolayers for scanning probe microscopy," *Biophysical Journal*, vol. 70, pp. 2052 – 2066, 1996.

[20] Z.-H. Wang, A. S. Viana, G. Jin, and L. M. Abrantes, "Immunosensor interface based on physical and chemical immunoglobulin G adsorption onto mixed self-assembled monolayers," *Bioelectrochemistry*, vol. 69, pp. 180 – 186, 2006.

[21] D. Peelen and L. M. Smith, "Immobilization of amine-modified oligonucleotides on aldehyde-terminated alkanethiol monolayers on gold," *Langmuir*, vol. 21, pp. 266 – 271, 2005.

Chapter 7

Conclusions

In order to improve the cost-effectiveness and sensitivity of phage-based ME biosensors, batch fabrication of micron- to millimeter-scale sensors was performed. Two different sensor fabrication methods used were:

1. the dicing-based method for millimeter-scale sensors
2. the co-sputtering-based method for micron-scale sensors.

Particularly, the co-sputtering method was found to be suitable for fabricating micron-scale sensors with dimensional consistency. In addition, by performing batch fabrication, the cost per sensor can be reduced to a fraction of a cent.

Rapidness of testing was also improved by using two different methods of bacterial detection as follows:

1. Direct detection of *S.* Typhimurium on fresh spinach leaves
2. Detection of *B. anthracis* spores with the aid of a designed microfluidic flow cell.

For the first method, by placing freestanding biosensors on spinach leaf surfaces, rapid, direct detection of *S.* Typhimurium was realized. This method does not require any pre-test sample preparation. Hence, total assay time was only 45 min. In addition, by characterizing the topography of leaf surfaces, the characteristic sizes of biosensors free from the surface topography effects were determined. Furthermore, a formula describing the probability of detection as a function of the size and number of biosensors and the surface density of *S.* Typhimurium was derived. By using the

formula, the required number of biosensors to obtain a desired LOD can be determined.

For the second method, PDMS microfluidic flow cells were designed, fabricated, and tested with 200 μm-long phage-based ME biosensors for the enhanced detection of *B. anthracis* spores. Due to the enhanced chances of physical contact between a biosensor and spores, the time required for the testing was only about 10 min. In addition, with the micron-scale ME biosensors, a small number of spores, down to 106 spores, were detected.

Additionally, to further enhance the detection capabilities of phage-based ME biosensors, the following effects were studied:

1. Effects of mass position on the sensitivity of ME biosensors

2. Effects of surface functionalization of ME biosensors on surface phage coverage.

The mass sensitivity of ME biosensors was found to be largely dependent on the longitudinal mass position and dimensions of the sensors. The formula derived in this work can be used to predict the mass sensitivity and resonant frequency change of differently sized ME biosensors for the detection of single pathogenic bacteria.

Surface phage coverage on differently surface-functionalized ME biosensors was quantified by atomic force microscopy. The activated carboxyl-based covalent attachment produced a phage coverage of $\sim 50\%$, comparable to that obtained through physical phage adsorption, a traditional way of phage immobilization. By contrast, aldehyde- and methyl-terminated surfaces did not yield high phage coverage. These surface functionalization may be used to construct "anti-phage surfaces" under proper buffer and sample preparation conditions. In addition, it was found that surface phage coverage is a key factor in analyte capture.

Finally, based on the above results, a concept of phage layer patterning was introduced. Phage may be patterned onto desired parts of biosensor surface to enhance detection capabilities.